TECHNISCHE UNIVERSITÄT MÜNCHEN

TUM School of Natural Sciences

Direct detection of the self-modulation instability of a long relativistic proton bunch in the AWAKE Experiment

Karl August Georg Valentin Rieger

Vollständiger Abdruck der von der TUM School of Natural Sciences der Technischen Universität München zur Erlangung eines Doktors der Naturwissenschaften (Dr. rer. nat.) genehmigten Dissertation.

Vorsitz:

Prof. Dr. Andreas Weiler

Prüfer*innen der Dissertation:

1. Hon.-Prof. Dr. Allen C. Caldwell
2. Prof. Dr. Laura Fabbietti

Die Dissertation wurde am 11.04.2023 bei der Technischen Universität München eingereicht und durch die TUM School of Natural Sciences am 19.10.2023 angenommen.

Technische Universität München
Fakultät für Physik

Werner Heisenberg Institut
Max Planck Institut für Physik

PhD Thesis

Direct detection of the self-modulation instability of a long relativistic proton bunch in the AWAKE Experiment

Direkte Beobachtung der selbstmodulations-Instabilität eines langen relativistischen Protonenpakets im AWAKE Experiment

Author:
Karl August Georg Valentin Rieger

Supervisor
Allen C. Caldwell
Advisor
Patric Muggli

21.03.2023

Abstract:

This thesis presents the time-resolved optical proton beam diagnostics of the AWAKE experiment at CERN and reports on the direct detection of the ionization-front-induced self-modulation instability of the Super Proton Synchrotron (SPS) proton bunch. A qualitative description of the self-modulation is given and the challenges with the diagnostics of the proton beam are presented. The principle of the diagnostics is shown and the detector (a streak camera) is validated in an experimental setup. Using the time-resolved images of the bunch this thesis reports the micro-bunch frequency of the self-modulated SPS proton bunch for plasma densities from $\sim 1 - 10 \cdot 10^{14}\mathrm{cm}^{-3}$. By using a discrete Fourier transform and setting a frequency detection threshold it is shown that the self-modulation frequency scales with the square root of the initial unperturbed plasma electron density and is close to the cold electron plasma frequency.

Kurzfassung:

Diese Arbeit präsentiert die zeitaufgelöste Protonenstrahl Diagnostik des AWAKE Experiments bei CERN und berichtet über die direkte Messung der durch eine relativistischen ionisierungs Front induzierten selbst-modulations-Instabilität. Eine qualitative Beschreibung der selbst-modulation wird präsentiert und Hürden für die Diagnose des Protonenstrahls werden aufgezeigt. Das Funktionsprinzip der Diagnostik wird erläutert und der ausgewählte Detektor (eine Streak-Kamera) wird mit einem experimentellen Aufbau getestet. Unter Verwendung von zeitaufgelösten Bildern des Protonenpakets misst diese Arbeit die Frequenz der Protonen Bündel des selbst-modulierten Super-Proton-Synchrotron (SPS) Protonenstrahls für Plasmadichten von $\sim 1 - 10 \cdot 10^{14}\mathrm{cm}^{-3}$. Mittels der diskreten Fouriertransformation und einem Detektionsgrenzwert wird gezeigt dass die selbst-modulations Frequenz mit der Wurzel der Plasmadichte skaliert und durch die Elektronen Plasmafrequenz eines kalten Plasmas gegeben ist.

Contents

1 Motivation for future accelerators and thesis goal

1.1 Accelerators and their use

History of the main accelerator types

The main function of a particle accelerator is to supply energy to a species of particles (e.g. electrons or protons). Today the large majority of particle accelerators can be divided into two types

- Circular accelerators
- Linear accelerators (LINACs)

In circular accelerators the particles receive an energy kick during each roundtrip. In LINACs they are continuously accelerated. Of these two types of accelerators a large majority uses Radio frequency (RF) cavities to increase the particle energy in each roundtrip or have the particle travel in phase with a RF wave to achieve energy gain. Only a small fraction of the modern accelerators use static electric fields (DC) to accelerate particles and they are usually only low energy ($< 50MeV$) accelerators.
Despite being in the minority today, the DC accelerators were the first type of accelerators that were developed in the form of cathode ray tubes (it was not even clear that they were particle accelerators until J.J. Thomson showed in 1897 that cathode rays were particles [1]). The energy in DC accelerators is limited by the possible sustainable DC voltage and even in the 1920s nuclear theory demanded higher voltages than those that seemed realizable. This changed when quantum tunneling was predicted and reachable voltages ($\sim 700kV$) were enough to split Lithium atoms. This was achieved in 1932 by Cockcroft and Walton, with the DC type accelerator named after them [2]. At the same time Van-de-Graf developed the accelerators named after him which were able to raise the achievable energies by DC machines up to $10MeV$. These are still used in modern times [3].
In 1925 Ising envisioned the use of a linear array of electrodes supplied with a RF field to accelerate particles by having the particles travel in phase with a electromagnetic wave. In 1928 Wideröe built the first realization of this acceleration technique where he used coaxial cylinders to accelerate particles. The technique of having particles in phase with a RF wave is up to today the main acceleration scheme used in LINACs and circular accelerators. Even the newest proposed high-energy accelerators plan to use the same technique. In 1931 Lawrence and Livingston designed and built the first cyclotron in which particles are accelerated with a constant frequency (for non relativistic particles)

and kept on a circular path by using one large magnet [4], while a small gap in the magnet is used to realize the phase synchronous acceleration of the particles. A little bit later, in the 1940s Louis Alvarez and McMillan (and of course other people working on accelerators) built the first synchrotrons in which dedicated dipoles keep the particle on a circular path and a small section is used to accelerate the particles at each pass using a synchronized voltage [5], a very successful method as the largest ever built accelerators are synchrotrons (e.g. the Large Hadron Collider, LHC, at CERN).

Modern demand for particle accelerators

Today, many associate particle accelerators with accelerating particles to high energies and colliding them in high-energy colliders (e.g. LHC at CERN). This is definitely a significant role for modern accelerators, but particle accelerators have many other uses. They can be used to produce all kinds of particles, not only electrons and protons, but also photons, neutrons and radioisotopes for medicine [6]. Today particle accelerators are used in many fields of science and technology and the number of accelerators used worldwide is > 10000 with research accelerators being only the minority, but a large number is used in medicine and industry to modify surfaces or examine materials. The following list gives a (non exhaustive) estimate of the number of large accelerators existing in the world and their use [7].

- Industrial accelerators ~ 1500
- Radiotherapy ~ 5000
- Ion implantation and surface modification ~ 7000
- Research ~ 1200

It must be stressed that most of these accelerators are far smaller than the well-known accelerators such as LHC, many of these accelerators fit in normal buildings or in the basement of a hospital! Even tough there is a huge demand for smaller accelerators the rest of this text will consider mainly the sub part of the research accelerators that are used for high-energy physics and search for new physics.

Energy limit of particle accelerators

In all accelerator types the maximum particle energy is limited. In cyclotrons the energy limit is mainly given by the magnetic field strength and the radius of the bending magnet.
In the synchrotron it is first limited by the magnitude of the bending magnetic field B_0 and the radius r of the circular trajectory (for relativistic particles $E_p = r\,|q|\,B_0 c$, where E_p is the particle energy), and second by the emitted synchrotron radiation $P = 8.85 \cdot 10^{-5} \frac{m}{GeV} \frac{c}{2\pi} \frac{E_p^4}{r^2} \propto E_p^2 B_0^2$ [8], which is proportional to the square of the energy of the particles times the bending magnetic field strength. The ultra-high-energy accelerators are synchrotrons because the radius of synchrotrons can be made much

bigger than the radius of a corresponding cyclotron and such the maximum achievable energy is much higher. The largest synchrotron in operation is the LHC that has a circumference of 27km and it is an example for the fact that the spatial dimension for high-energy synchrotrons is enormous. In the LHC the particle energy limit is given by the B-field of the bending dipole magnets.
In LINACs synchrotron radiation due to the radial acceleration, does not exist. But the acceleration gradient, together with the physical size of the accelerator sets the limits of achievable energies. Modern RF cavity structures reach accelerating fields of $\sim 100\frac{MV}{m}$, while operating with a RF source at $\geq 10GHz$ (X-band and frequencies above). These modern cavities are used in larger LINACs such as the 1.7km long XFEL accelerator (that delivers an ∼17 GeV electron beam) which would be even longer and more expensive without such cavities [9]. Going to higher accelerating fields leads to breakdowns of the RF cavities. The acceptable breakdown rate for future colliders is very tight, e.g. $< 10^{-7}$ breakdowns/pulse/meter [10] and it is not easy to build cavities with gradients above $100\frac{MV}{m}$ that reach such low limit. Repeated breakdowns do not only lower the uptime of the whole accelerator, but also destroy the cavities over time and lower the achievable maximum accelerating gradient. This can be mitigated by having extra spare cavities in the collider and operating all cavities at a lower gradient, which in turn makes the collider even longer.

Planned colliders

Driven by the advancing accelerator technology from the beginning of the 1930's that created cheaper and higher energy accelerators, many fundamental discoveries in particle physics have been made. The newest high energy particle physics collider, the LHC, has achieved its minimum goal of detecting the Higgs-Englert boson. Yet no significant sign of new physics (supersymetry or direct dark matter production) has been found during LHC runs until now [11]. Increasing the available precision on the Higgs-Englert coupling constants would place new constraints on the existence of new beyond standard model physics particles, but this is hardly achievable with the LHC $p^+ - \bar{p}^-$ collider [12]. A high energy $e^- - \bar{e}^+$ collider ($\geq 500GeV$ invariant mass energy) can perform high precision Higgs measurements and search for new physics in a very clean environment because e^- and $\bar{e}^+$ are fundamental particles [13]. There are four main candidates for a future $e^- - \bar{e}^+$ collider.
The ILC (International Linear Collider) to be possibly built in Japan, CLIC (Compact Linear Collider), the circular CepC in China and the FCC at CERN [14]. Other proposed future accelerators are electron-proton colliders at very high center of mass energy $\sqrt{s} \sim 9TeV$ that requires highly relativistic electrons at $3TeV$ but open a lot of possibilities in beyond standard model physics and quantum chromodynamics physics by probing the electrons and quark constituents of the proton [15].

All these proposed accelerators need very high energy electrons (0.5 - 3 TeV) for which a linear accelerator is highly desirable as the circumference of a circular accelerator would be immense (up to 100km for the FCC, which has ∼0.5 TeV electron energy). But even

the linear collider candidates such as CLIC or ILC are enormous structures, e.g. CLIC is estimated to have a length of $\sim 50km$ and the shorter ILC still reaches $\sim 31km$. Despite having high-gradient RF cavities, the high energy requirements for the particle beams make the future linear colliders (CLIC/ILC) very large (spatial and man power) and expensive technical challenges. Because conventional accelerator technology is readily commercially available and has been successful since ∼70 years, one can make a total cost estimate (C) on the future colliders via the $\alpha\beta\gamma$-formula [14]

$$C = \alpha \left(\frac{Length}{10km} \right)^{1/2} + \beta \left(\frac{Energy}{TeV} \right)^{1/2} + \gamma \left(\frac{Power}{100MW} \right)^{1/2}$$

with $\alpha = 2 \cdot 10^9\$/(10km)^{1/2}$, $\beta = 2 - 10 \cdot 10^9\$/(TeV)^{1/2}$ and $\gamma = 2 \cdot 10^9\$/(100MW)^{1/2}$. By estimating the costs for the CLIC $500GeV$ option ($\sim 10 \cdot 10^9\$$) one sees that the costs for such accelerators easily reaches the total costs of the LHC which was one of the major European scientific projects in the last 30 years. This means that the next collider will be a time consuming and expensive international project.
For the proposed LINACs the geological boundary conditions pose a serious problem due to their size. So the limits that set boundaries on the reachable particle energies are given by:

I) landscape

II) structure size

III) acceleration gradient

All of these limit the possible size of the accelerator and the reachable energy of the accelerated particles. The huge costs and size of the next colliders, when using conventional technologies, explains the interest in recent yeas in future acceleration schemes such as plasma-based acceleration or dielectric wakefield acceleration. And maybe they might lead someday to a new standard acceleration technique as RF cavities are today.

1.2 Plasmas and particle acceleration

Plasma-based acceleration can be divided into two main approaches: laser-driven wakefield acceleration such as the plasma-beat wave accelerator (PBWA) or laser wakefield accelerator (LWFA). The other main approach is particle-driven wakefield acceleration (PWFA). Both try to use plasma waves to accelerate particles but they differ in the plasma wave excitation source. A Laser in PBWA/LWFA and particles in PWFA. The LWFA/PBWA are the older of the three schemes.

Laser and particle-driven acceleration

The first proposal to use lasers and a plasma to accelerate particles was given in 1979 by Tajima and Dawson [16]. The concept is to use either a short, intense laser pulse that excites a electrostatic wakefield in a plasma or to use two laser pulses that differ

in frequency by the plasma frequency so that the beating of these two pulses excites a plasma wave [17]. From the beginning it was clear that particles trapped in the wakefields of a LWFA or PBWA see electric fields in the range of $\sim$ multi GV/m which is $100-1000$ times higher than what can be achieved in RF cavities. Experiments with the PBWA concept were carried out in the 1980s-1990s, but shortly after, high power laser machines became more available in the 1990s, great success was achieved by using the LWFA concept. Already in 1996 electric fields of $\sim 10GV/m$ [18] were reached in an experiment. Because of the availability of short high power laser pulses LWFA became an active research topic that is still an active research area. LWFA has shown great results and with experimentally demonstrated fields of $> 50GV/m$ [19] it holds the records for largest energy gain/unit length but the demands of future particle accelerators are very strict in terms of beam quality and LWFA struggles to meet the energy spread requirements. Also the acceleration length is very short ($\sim$ mm) and thus the total achieved energy of $\sim 8GeV$ [20] is far below the required hundreds of GeV. A possible solution would be staging of the LWFAs and this is an ongoing research topic [21].

Only six years after lasers were proposed as drivers for plasma waves, in 1985 it was suggested that particles are also able to excite plasma waves. And in 1988 a experimental proof of this concept was published [22] although the reported accelerating field was only in the MV/m range. After almost 20 years it was shown at Stanford linear accelerator center (SLAC) that PWFA is able to also achieve GV/m accelerating fields. In the experiment the research group around Blumenfeld was able to double the energy of electrons in the 42GeV electron SLAC bunch in a plasma of $\leq 1m$ length. PWFA has a long history of successful experiments with electrons, for example at Argonne National laboratory, at SLAC (FACET facility), or at Brookhaven National Laboratory (BNL) in the US. With the electron beam requirements of modern free electron lasers (FEL) even more facilities started recently (from $\sim$ 2015 on) with R&D of PWFA. Not only intense electron beams can be used as drivers but also positrons and proton bunches as is done at the AWAKE facility at CERN, a experiment that wants to show the feasibility of proton driven plasma wakefield acceleration. This experiment and the reasons for proton driven acceleration will be explained in the next section.

1.3 Drivers in plasma and AWAKE

1.3.1 Driving plasma waves

For acceleration in a plasma to occur, there needs to be a driver to separate the electrons and ions to create electric fields. With a suitable driver the fields can reach the wave breaking field $E_{wb} = \frac{\omega_{pe} m_e c}{e}$ (ω_{pe} is the electron plasma angular frequency which sets a typical timescale for electron oscillations in a plasma, m_e is the electron mass and e is the electron charge and c is the speed of light) which is greater than $1GV/m$ for plasma densities above $10^{14} cm^{-3}$. The perturbation in plasma electron density that sustains the accelerating field can be created by the field of a (relativistic) charged particle bunch or the ponderomotive force of an intense laser pulse. While a laser pulse drives wakefields,

the accelerated electrons de-phase with respect to the laser. The relativistic electrons catch up with the laser pulse and overtake it because the group velocity of the laser pulse in plasma is slower than the speed of light. This can be seen by looking at the dispersion relation of a transverse electromagnetic wave with angular frequency $\omega_0 = ck_0$ in an un-magnetized plasma [23]

$$\omega_0^2 = c^2 k_0^2 + \omega_{pe}^2.$$

Therefore the group velocity for the pulse in the plasma $v_g = \mathrm{d}\omega/\mathrm{d}k = c \cdot \left(1 - \left(\frac{\omega_{pe}}{w_0}\right)^2\right)^{-1/2}$ is less than c. The laser wakefield relativistic factor (that means the gamma of a particle that has the same velocity as the laser group velocity) is given by $\gamma_\Phi = (1 - \frac{v_g^2}{c^2})^{-1/2}$. The de-phasing length ΔL a witness electron ($\gamma_e > \gamma_\Phi$) and the driving laser pulse (γ_Φ) experience over some distance L is approximately given by $\Delta L = L\frac{1}{2\gamma_\Phi^2}(1 - \frac{1}{2\gamma_\Phi^2})$. The de-phasing length L_ϕ can be determined by allowing a maximum ΔL of $\sim \frac{2\pi c}{\omega_{pe}} = \lambda_{pe}$ (λ_{pe} is the plasma wavelength) as the electrons in LWFA experiments are $\sim \lambda_{pe}$ behind the laser pulse. This results in $L_\phi = \frac{2\lambda_{pe}\gamma_\Phi^2}{1-\frac{1}{2\gamma_\Phi^2}}$. For typical laboratory parameters $\omega_0 \sim 2\pi \cdot 380THz$, the γ_Φ of a laser pulse is rather low and is shown together with the de-phasing length of the pulse in fig.1.1 (all images in this work are created by matplotlib [24] or Octave [25], all calculations are done with numpy [26] or scipy [27]) for plasma particle densities in the range $10^{14} - 10^{18}cm^{-3}$. It can be seen that at plasma particle densities $> 10^{17}cm^{-3}$ γ_Φ is $<<$ 100 and the de-phasing length is short ($\sim \mu m$ for plasma densities $> 10^{18}cm^{-3}$), which limits the achievable energies to $\sim 10GeV$ ($E_{wb} \cdot L_\phi$). For plasma particle densities below $10^{17}cm^{-3}$ γ_Φ and L_Φ are larger (and L_Φ can reach more than 100 km) but the wave breaking field is significantly lower and thus the whole system becomes much longer up to the point where there is no difference in length when compared to conventional accelerators.
In the acceleration process the plasma transfers the energy of the driver (be it a laser pulse or a particle bunch) to the witness bunch and the total energy that can be transferred is at maximum the energy of the driving pulse. The available energy in the highest powered, short (length $\tau < \frac{1}{\omega_{pe}} \sim 0.02ps$ for a plasma particle density $n_{pe} = 1 \cdot 10^{18}cm^{-3}$), laser pulses is still less than $0.1kJ$ and thus the total energy of the driver that can be transferred to the accelerated bunch is much less energy than that of the ILC bunches or the CLIC bunches ($\sim 8kJ$ for ILC and $\sim 0.75kJ$ for CLIC). One needs a complicated staging of very costly large high power lasers pulses because each single laser pulse can only partly accelerate the witness bunch.For very high powered laser with $> kJ$ pulse energy the repetition rate is low, i.e. $\ll 1Hz$, and those are not considered to be used as accelerator drivers.

In the PWFA case there are particle drivers available that are extremely relativistic as e.g. the SLAC electron bunch that has a γ of ~ 45000 so the bunch velocity is very close to c. The particle drivers still loose energy but can retain a very large γ. For example if the SLAC bunch lost 99% of its energy the gamma would still be $880 \gg 1$ and de-

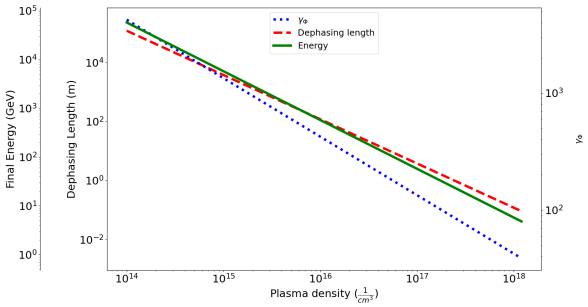

Figure 1.1: The gamma factor of a laser γ_Φ that drives a wakefield (blue dotted line, right axis), De-phasing length for electrons subject to the wave breaking field (red, inner left axis). Green: The final energy electrons can reach in a electrostatic plasma wave driven if they are accelerated with the wave breaking field over the whole de-phasing length. The total reachable energy goes down with higher plasma densities as the de-phasing length becomes very short and the wave breaking field only grows with $n_{pe}^{1/2}$.

phasing lengths are on the order of km. The maximum available energy per electron at SLAC is $\sim 45GeV$, with a bunch population of $2 \times 10^{10} e^-$ this corresponds to $\sim 160J$ per bunch that can only accelerate (based purely on energy conservation arguments) $0.08 \times 10^{10} e^- = 0.13nC$ to about 1.5 TeV (CLIC electron energy) at maximum but the CLIC has a bunch population of $\sim 0.3 \times 10^{10} e^- = 0.5nC$. Similar is true for the ILC as the needed energy is only $0.5GeV$ but the bunch population is $> 1 \cdot 10^{11} e = 16nC$. This means that for PWFA one needs high charge bunches to transfer enough energy to the witness bunches or very high energy bunches. Heavier particles bunches available today, as protons bunches, are not as relativistic as electron beams, but can carry much more energy due to their higher mass which makes proton bunches candidates for plasma drivers to accelerate e^- to very high energy (TeV) in a single plasma.

The use of the CERN proton bunch has been suggested [28] to build a $p^+ - e^-$ collider that uses plasma-based acceleration to obtain electrons with an energy of $3TeV$. Together with the $7TeV$ proton bunches from the LHC a $\sim 9TeV$ center of mass (COM) collider can be expected to give new insights into the deep inelastic scattering of electrons and protons. At this high COM energy the cross section for proton electron scattering is high and thus the proposed accelerator does not necessarily need a large integrated luminosity to obtain many events for scatterings electrons on proton quarks with a low fraction ($x < 10^{-5}$) of the proton total momentum [28]. With the proposed accelerator, proton matter can be studied up to a factor of 1000 lower parton momentum fractions than with old experiments such as HERA and experimental data for QCD regions not yet explored can be acquired. This (future) accelerator at the LHC needs a $3TeV$ electron bunch that needs to be created within $4km$ as this is a space constraint of this suggested VHEep. This means that one needs the possibility to have a $750MeV/m$ accelerating

structures. This can be obtained by plasma-based acceleration schemes. The LHC proton bunch ($\sim 19nC$ bunch population, total bunch energy $\sim 131kJ$) can be used to drive plasma wakefields with the needed field strength and can transfer enough energy to the electron bunch ($\sim 10nC, 3TeV \leftrightarrow 30kJ$). The de-phasing length for a de-phasing of $100\mu m$ between the LHC bunch and $3TeV$ electrons is $\sim 5.5km$. This motivates the use of proton bunch drivers for electrons acceleration and the AWAKE experiment is used to study the possibility to use proton bunches as drivers for plasma-based acceleration.

1.3.2 AWAKE

The foregoing section has shown that for a future plasma-based accelerator a lot of energy needs to be transferred from the driver to the accelerated particles. As shown high energy particle beams are a candidate because of their high total bunch energy. The SPS beam is a $400GeV$ proton beam that is injected into the LHC. The AWAKE experiment is a proof of principle experiment to show the feasibility of using long ($2\sigma \sim 800ps$), high-energy particle bunches for plasma acceleration. The main goals of this experiment are to show that:

- the self-modulation instability of a long proton bunch occurs and can be seeded
- electrons can be accelerated in the wakefield driven by the proton bunch
- the acceleration length can be several meters

This thesis will mainly deal with the first item of this list and the setting up of a beam diagnostic that can be used to detected the self-modulation and infer several of its critical parameters.
The general setup of AWAKE is to use the SPS $400GeV$ proton beam ($\gamma = 427, \beta = \sqrt{1 - \frac{1}{\gamma^2}} = 0.999997 \sim 1$) to drive wakefields in a $10m$ long Rubidium plasma with a density between 10^{14} and $10^{15} cm^{-3}$ (density units are $\#/cm^3$). The key to the AWAKE experiment is a high-powered short ($\sigma_t < 120fs$) laser pulse that co-propagates with the proton bunch. The laser pulse creates a relativistic ionization front (RIF) that creates a plasma in which the proton bunch excites wakefields. Only parts of the proton bunch that enter the Rubidium at later times than the RIF experience a plasma which is equivalent to a sharp cut bunch in a pre-existing plasma and the cut part in the plasma excites wakefields. The wakefields interact with the proton bunch and an instability develops (the self-modulation instability) that transforms the bunch into a train of micro-bunches with temporal period $\frac{1}{f_{pe}}$ (f_{pe} is the cold plasma electron frequency, see next chapter) [29]. The instability can occur when the RIF is far ahead of the proton bunch, but it can be seeded by placing the RIF within the proton bunch. It is then the seeded self-modulation instability (SSM). The transformed bunch can excite large amplitude wakefields and the first observation of the SSM development, the micro-bunches of the proton drive bunch and the measurement of the modulation frequency is the main result of this thesis. A drawing of the AWAKE area and of the experiment is shown in fig.1.2. At position (a) the proton bunch is co-propagating with the laser pulse in vacuum. At

position (b) electrons created by an electron gun [30] are merged with the main proton beam line in phase two (see below). At position (c) the laser pulse and the proton bunch enter, spatially overlapped, a Rubidium (Rb) vapor source which is heated to create a vapor with the desired density [31]. The Rb temperature is controlled precisely to ensure a constant density within 0.2% along the whole $10m$. For a future acceleration experiment, the electrons that will be accelerated occupy only a fraction of the plasma wavelength λ_{pe} in the plasma wave. When the density changes, λ_{pe} changes and this shifts the electrons with respect to the plasma wave. When this shift is longer than 25% of λ_{pe} the accelerated electrons will no longer be accelerated. This leads to a 0.2% density stability requirement that is measured by two interferometers at the beginning and end of the vapor source [32]. The laser pulse ionizes the first electron of the Rubidium atoms and creates a plasma with $n_{pe} = n_{Rb}$. At position (d) the self-modulated proton bunch exits the plasma and the laser pulse is blocked by an Aluminum foil. Shortly behind the laser dump there is a beam monitoring station (BTV) that is the first part of the indirect self-modulation measurement [33]. Afterwards, at position (e) there is first a coherent transition radiation station. $30cm$ behind it there is an optical transition radiation station that creates light with the same time and space structure as that of the proton bunch. The light is transported via a transport line (f) and then reaches two streak cameras at (g). These create time resolved images of the bunch and they are behind a radiation shielding made of concrete. Simulations and the experiment show that the radiation created by the beam is very dangerous for technical equipment (and of course for most living beings). Thus the cameras have to placed this far apart from the beamline.

Numerical simulations suggest that wakefields excited by the SSM reach amplitudes up to $1GV/m$ [34], which is ten times larger than any modern RF cavity can sustain. The experiment is split in two phases with different goals. In the first phase in 2017, the aim was to study the SSM. The experimental proof of the SSM was shown with the use of optical transition radiation and time resolved images of the bunch. In the second phase the aim was to demonstrate the acceleration of electrons injected into the wakefields driven by the self-modulating bunch over 10 meters. This was also achieved in 2018 which concludes Run 1 of the AWAKE experiment ($\sim 2016 - 2018$). In Run 2 of AWAKE the goal is to stage plasma sources and achieve stable electron acceleration not only over $10 + m$ of plasma but over multiple plasma stages and preserve the quality of the accelerated electron bunch.

1.4 Conclusion and thesis goal

All modern high-energy particle accelerators use RF cavities to accelerate particles, a technique developed in the 1920s. With this acceleration technique the proposed future accelerators such as CLIC or FCC, are even larger than the largest accelerator of today, the LHC with 27km circumference. The cost for these huge machines is also becoming very prohibitive. This stimulates looking into alternatives techniques to accelerate parti-

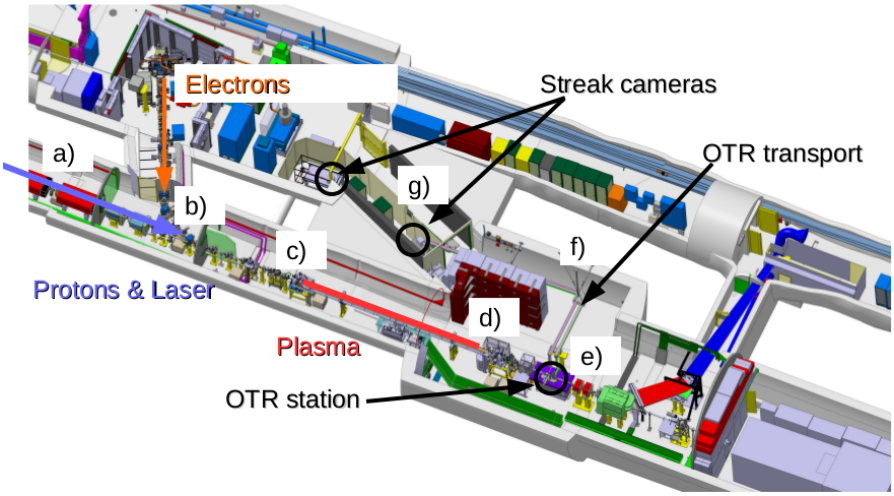

Figure 1.2: Awake facility with the main experimental parts. The plasma cell is marked as a red line. The incoming proton bunch and laser pulse are in light blue. The electron injection path is in depicted by the orange arrow. The OTR station and the streak cameras are located in the black circles.

cles, which is where plasma-based acceleration might become an option as a acceleration scheme that is cheaper and smaller by operating at much larger gradient. Proton-driven plasma acceleration is a promising candidate for high-energy physics and the AWAKE experiment at CERN is a proof of principle experiment to show the feasibility of such a PWFA.

This thesis presents the arguments for choosing optical transition radiation and a streak camera as a diagnostics tool for the self-modulation the AWAKE proton bunch. It shows the theoretical setup and reasoning for the diagnostics and implements the setup in the AWAKE experiment area. Further this thesis shows with a direct observation that the self-modulation of a long proton bunch can be triggered. Further the existence of micro-bunches is shown and the frequency of the micro-bunches created by the self-modulation over a plasma density range of $1-11\cdot10^{14}cm^{-3}$ is measured. It will be shown that the micro-bunch modulation frequency scales as predicted, with $\sqrt{n_{pe}}$, where n_{pe} is the plasma electron density.

2 Physics behind the self-modulation in AWAKE

The central part of AWAKE is to use a plasma to generate an electric field to accelerate electrons. This chapter introduces concepts of plasma physics for the self-modulation of proton bunches and its possible diagnostics.The chapter shows that the self-modulated proton bunch has only a radial density modulation but no current modulation.

2.1 Plasma description

Using the definition of Chen [35] a plasma can be defined as "a quasi neutral gas of charged and neutral particles which exhibits collective behavior". Following are the parameters that define the plasma in the context of particle driven plasma acceleration.

- plasma electron density n_e $[\#/cm^3]$
- plasma ion density n_i $[\#/cm^3]$
- plasma electron frequency $f_{pe} = \frac{1}{2\pi}\sqrt{\frac{e^2 n_e}{m_e \epsilon_0}} = \frac{1}{2\pi}\omega_{pe}$ $[Hz]$

For a plasma to exist the collisions with neutral atoms must be rare, i.e. the time between neutral collisions must be greater than typical timescales in the plasma. In the AWAKE case one assumption is that the laser pulse 100% ionizes the Rubidium vapor so that we have $n_e = n_i = n_0$ where n_0 is the Rubidium vapor density. The single ionized Rubidium atom is ~ 160000 times heavier than an electron and all timescales for them are much longer than any electrons timescale ($\tau < \frac{1}{\omega_{pi}}$), so a fixed ion background $n_i = n_0$ is assumed in the discussion of the self-modulation. For longer bunches than the AWAKE bunch the assumption of a static background might become problematic, for the purpose of this chapter it suffices.

To describe the plasma and the beam a Magnetohydrodynamics (MHD) approximation is employed because all plasma waves are expected to be on a larger scale than the Debye length ($\lambda_D = \sqrt{\frac{\epsilon_0 k_b T}{n_e e^2}}$). It will be found that the shortest timescale is the inverse plasma frequency $\tau = \frac{2\pi}{\omega_{pe}}$ which makes the MHD approximation a good candidate for a qualitative view to understand the self-modulation. The electron temperature is neglected and the plasma is modeled as a cold plasma. This is surely incorrect in the real experiment, but to get a qualitative view of the physics it is enough. To include the effect of a beam in a plasma the charge density $q_b n_b$ of the external beam needs to

be included in Poisson's equation and Ampere's Law. Here q_b is the charge of the beam particles ($+e$ for protons) and $n_b(x, y, z, t)$ is the charge density of the beam.

$$\vec{\nabla} \cdot \vec{E} = \frac{(n_i q_i + n_e q_e + n_b q_b)}{\epsilon_0} \tag{2.1}$$

$$\vec{\nabla} \times \vec{E} = -\partial_t \vec{B} \tag{2.2}$$

$$\vec{\nabla} \cdot \vec{B} = 0 \tag{2.3}$$

$$\vec{\nabla} \times \vec{B} = \mu_0 \left(n_i q_i \vec{v_i} + n_e q_e \vec{v_e} + n_b q_b \vec{v_b}\right) + \frac{1}{c^2} \partial_t \vec{E} \tag{2.4}$$

$$m_j n_j \partial_t \left[\vec{v_j} + \left(\vec{v_j} \cdot \vec{\nabla}\right) \vec{v_j}\right] = q_j n_j \left(\vec{E} + \frac{1}{c} \vec{v_j} \times \vec{B}\right), j = i, e \tag{2.5}$$

$$\partial_t n_j + \vec{\nabla} \cdot (n_j \vec{v_j}) = 0, j = i, e \tag{2.6}$$

Here $\vec{E}$ and $\vec{B}$ are the electric and magnetic fields in the plasma. n, $\vec{v}$, m and q describe the density, velocity, mass and charge of electrons (e) and ions (i). The beam itself is for now considered as an external (fixed) source term in the plasma.
A limiting factor for the MHD approximation is when the electric fields comes close to the wave breaking field which is given for a one dimensional plasma as $E_{1D} = \frac{m_e c \omega_{pe}}{e} = E_{wb}$. When wave breaking occurs it can be seen as if all electrons are compressed to an infinitely thin sheet and the fluid description breaks down [36]. This means that in the discussion of the excited wakefields the amplitude is limited to the wave breaking field. This is not strictly necessary as the developed theory is valid for electrostatic waves with amplitude larger than the wave breaking field but in these cases the linear theory, presented in the next section, is no longer valid.

2.2 Linear plasma response theory

Solving equations 2.1 to 2.6 with a given beam density shows that there will be plasma waves trailing the beam. Because the Euler equation 2.5 is nonlinear, it is useful to linearize it by assuming that the initial electrons and ions densities are homogeneous in space, have a velocity density near zero and there are (on a macroscopic scale) no electric and magnetic fields in the unperturbed plasma. Only perturbations to first order will be retained.

Linearizing the plasma densities and velocities around their equilibrium values leads to

$$\vec{v_i} = 0, \vec{v_e} = \vec{v_0} + \vec{v_{pe}} = \vec{v_{pe}} \tag{2.7}$$

$$n_i = n_0, n_e = n_0 + n_{pe} \tag{2.8}$$

$$\vec{E} = \vec{E_0} + \vec{E_1} = \vec{E_1} \tag{2.9}$$

$$\vec{E} = \vec{B_0} + \vec{B_1} = \vec{B_1} \tag{2.10}$$

This linearization is only valid if the velocity of the plasma electron density is small compared to the velocity of the driving bunch and the perturbation in the plasma density

is also small $n_{pl} << n_0$. Neglecting quadratic terms in the perturbations the fluid equations eq.2.5 and eq.2.6 read now [37]

$$\partial_t \vec{v_{pl}} = \frac{-e}{m_e}\vec{E} \tag{2.11}$$

$$\partial_t n_{pl} + n_0 \nabla \vec{v_{pl}} = 0 \tag{2.12}$$

Assuming an infinite plasma and a relativistic proton beam going in the z-direction ($\rho_{beam} \sim e n_b(z - \beta ct, r, \theta) = e n_b(\zeta, r, \theta)$) and using

$$\rho = -e n_{pe} + e n_b \tag{2.13}$$

$$\vec{j} = -e n_0 \vec{v_{pe}} + e\vec{\beta} n_b \tag{2.14}$$

together with Poisson's equation eq.2.1

$$\vec{\nabla} \cdot \vec{E} = 4\pi(n_b q_b - e n_e) \tag{2.15}$$

one can find an equation for the perturbation in the density (after performing a change of variable to $\zeta = z - \beta ct \sim z - ct$) [37] due to the beam

$$\partial_\zeta^2 n_{pe} + k_p^2 n_{pe} = k_p^2 n_b \tag{2.16}$$

where $k_p = \frac{\omega_{pe}}{c}$ is the plasma wave number. This equation describes the plasma density perturbation due to an external charged beam and it can be seen that the plasma density perturbation is a driven linear harmonic oscillator with fixed k_p that has following solution [38]

$$n_{pe} = \int_{-\infty}^{\zeta} \mathrm{d}\zeta' n(\zeta', r, \theta) \sin(k_p(\zeta - \zeta')) \tag{2.17}$$

Note that the lower boundary can often be cut to some finite value e.g. when the beam is not infinitely long and that the density perturbation in the radial direction is given exactly by the radial beam distribution. The driver does not only perturb the plasma density but both plasma and the driver create electric fields. The electric and magnetic fields created by the driver in the plasma are determined by the equations [38]

$$\left(\Delta_\perp - k_p^2 + \frac{1}{\gamma^2}\partial_\zeta^2\right)\vec{E} = -\hat{z}\partial_\zeta\left(\frac{q_b n_b}{\gamma^2} + q_{pe} n_{pe}\right) + \hat{r}\partial_\zeta\left(q_b n_b + q_{pe} n_{pe}\right) \tag{2.18}$$

$$\left(\Delta_\perp - k_p^2 + \frac{1}{\gamma^2}\partial_\zeta^2\right)\vec{B} = -\hat{\theta}\beta\partial_r q_b n_b \tag{2.19}$$

where $\hat{\cdot}$ denotes a unit vector, $\Delta_\perp = \nabla^2 - \partial_\zeta^2$ is the cylindrical transverse nabla operator. The radial wakefield $W_\perp$, which is defined as the radial force per unit charge, excited by the beam is then given by

$$W_\perp = \hat{r}\left(E_r - \beta_b B_\theta\right) \tag{2.20}$$

The longitudinal wakefield $W_\parallel$ is given by

$$W_\parallel = \hat{z} E_z \tag{2.21}$$

In [38] a throughout derivation of the solution for the electric fields is given for a radially symmetric beam. For ultra relativistic particles ($\gamma \to \infty$) the wakefields to first order are given by the expressions

$$W_{\parallel} = \frac{\pm e k_p^2}{\epsilon_0} \int_{-\infty}^{\zeta} \mathrm{d}\zeta' \cos(k_p(\zeta - \zeta')) R\left(r, n_b\right) \tag{2.22}$$

$$W_{\perp} = \frac{\pm e k_p^3}{\epsilon_0} \int_{-\infty}^{\zeta} \mathrm{d}\zeta' \sin(k_p(\zeta - \zeta')) R'\left(r, n_b\right)) \tag{2.23}$$

where $R(r, n_b)$ is given by

$$R(r, n_b) = K_0\left(\frac{\omega_{pe} r}{c}\right) \int_0^r \mathrm{d}r' r' n_b(\zeta', r') I_0\left(\frac{\omega_{pe} r'}{c}\right) + I_0\left(\frac{\omega_{pe} r}{c}\right) \int_r^{\infty} \mathrm{d}r' r' n_b(\zeta', r') K_0\left(\frac{\omega_{pe} r'}{c}\right) \tag{2.24}$$

and $R'(r, n_b)$

$$R'(r, n_b) = \partial_r R(r) = K_1\left(\frac{\omega_{pe} r}{c}\right) \int_0^r I_0\left(\frac{\omega_{pe} r'}{c}\right) r' n_b(\zeta', r') - I_1\left(\frac{\omega_{pe} r}{c}\right) \int_r^{\infty} K_0\left(\frac{\omega_{pe} r'}{c}\right) r' n_b(\zeta', r') \tag{2.25}$$

here K_n and I_n are the modified Bessel functions of the second and first kind of order n respectively. Equations 2.23 and 2.22 describe the resulting wakefields in the plasma due to an external beam in a linearized fluid theory. Note that the k_p factor from derivatives was included in the prefactors of the wakefields. The charge of the driving bunch determines whether the + sign (protons) or the − sign (electrons) is used. Here after I will always use the plus sign. In many cases (as in AWAKE) the beam density can be considered to be of the form $n_b = e^+ \cdot Q f_r(r) h(\zeta)$ where Q is the number of protons in the beam, f and h are the beam radial and longitudinal distribution functions that are normalized to one and e^+ is the proton charge (positive). With this proton beam shape the perpendicular and parallel wakefields have a purely longitudinal component given by

$$W_{\parallel Long} = \frac{k_p^2 Q e^2}{\epsilon_0} \int_{-\infty}^{\zeta} \mathrm{d}\zeta' cos(k_p(\zeta - \zeta')) h(\zeta') \tag{2.26}$$

$$W_{\perp Long} = \frac{k_p^2 Q e^2}{\epsilon_0} \int_{-\infty}^{\zeta} \mathrm{d}\zeta' sin(k_p(\zeta - \zeta')) h(\zeta') \tag{2.27}$$

and a purely radially part given by $R(r, f), R'(r, f)$.These two equations show that the fields created due to the plasma density perturbation do have a longitudinal wakefield component which can be used for acceleration. But it also shows that the wakefields strongly depend on the beam shape and the total charge in the bunch. Thus the created fields do have a longitudinal wakefield component that can be used to accelerate particles, yet there is always a perpendicular component and the exact wakefield depends on the bunch shape via eq.2.27.

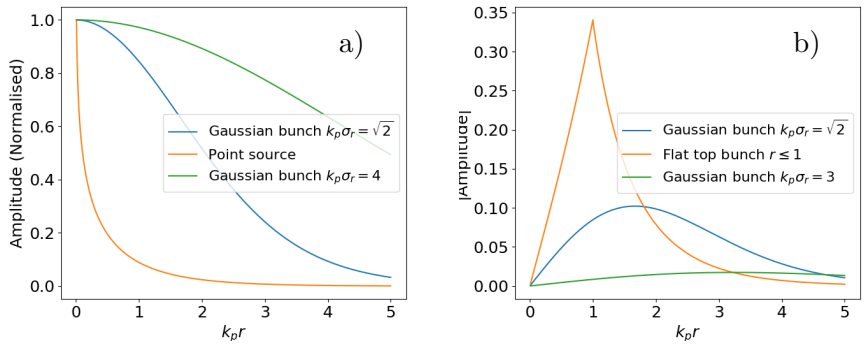

Figure 2.1: Image a) shows the radial dependency of the longitudinal wakefields normalized to one. The maximum amplitude is reached on axis. Note that the broader the bunch is the lower the amplitude is, so a very broad pulse will not excite large wakefields. Image b) shows the transverse wakefield dependency on the radius is shown. The wakefields are only focusing or de focusing (depending on the wakefield phase) and can act for on axis particles as a linear restoring force.

2.2.1 Radial dependency of the wakefields

The radial wakefield dependency of the longitudinal part is shown in fig.2.1 a) for a Gaussian beam (in radius) in blue ($k_p\sigma_r = 1$) and a point source $\delta(r)/r$ in yellow. The longitudinal wakefield is at maximum at the bunch center so one wants to inject electrons directly a the center. The transverse wakefield dependency on the radius is shown in fig.2.1 b) for a Gaussian bunch (blue, green) and a flat top bunch with $n_\perp = const$ for $r < 1$ and zero elsewhere. The flat top bunch has a linear increasing part ($\sim I_1(k_pr)$) up to its edges and from there on it decays. The Gaussian beams lead to radial wakefields that are also almost linearly growing up to $k_p\sigma_r \leq 1$ and then decay exponentially. The amplitude of the wakefields, for a given beam charge, becomes larger when the beam is more focussed which will play an important role in the self-modulation. The radial part is zero and grows almost linearly with radius. Thus an accelerated particle sees a linear restoring force towards the maximum accelerating position on axis. The longitudinal part monotonically decays with r. This means that particle injected on axis see the highest accelerating fields (longitudinal dependency) and a focusing or de-focusing field (depending on the phase).

2.2.2 Wakefields by Gaussian driving beams

Bunches as the SPS proton beam have a longitudinal shape that can be estimated with a Gaussian distribution $h \sim \exp(-\frac{\zeta^2}{2\sigma_\zeta^2})$. For this longitudinal distribution the solution of the perpendicular and parallel wakefields far behind the bunch ($\zeta \gg \sigma_\zeta, \zeta \to \infty$) is

given by

$$W_\perp = R' \frac{k_p^2 Qe}{\epsilon_0} \exp\left(-\frac{k_p^2 \sigma_\zeta^2}{2}\right) \cos(k_p \zeta) \tag{2.28}$$

$$W_\parallel = R \frac{k_p^2 Qe}{\epsilon_0} \exp\left(-\frac{k_p^2 \sigma_\zeta^2}{2}\right) \sin(k_p \zeta) \tag{2.29}$$

which are, aside from scaling factors, sine and cosine waves that oscillate with the plasma frequency. The longitudinal wakefield is oscillating between being accelerating and decelerating. In order to accelerate particles they are injected in the correct phase of the wakefield. In this case they will see only the accelerating phase if they are fast enough to be captured by the wave. This is also the principle of electron acceleration in AWAKE. A proton bunch crates wakefields and a 18MeV electron bunch is injected into the proton bunch, so electrons in the correct phase are captured and accelerated [39].
The transverse wakefield is out of phase by π with respect to the longitudinal ones. This means that a particle that is maximally accelerated does not feel any transverse force and is unguided. To have a guided acceleration one wants to have the particles in the accelerating and focusing phase. Ignoring the scaling by R and R', the amplitude of the oscillations and thus the excited wakefields strongly depends on the length of the bunch, respectively the plasma density through $k_p \sigma_\zeta$. For a given radial dependency the wakefield amplitude is maximum when the condition $\sigma_\zeta k_p = \sqrt{2}$ is fulfilled [40]. When this condition is not fulfilled one can see from eq.2.28 and 2.29 that the wakefields decay exponentially in amplitude with $k_p \sigma_\zeta$ increasing. This result has important implications for particle driven plasma wakefield acceleration - as for a given bunch length - it sets a limit for the plasma density and thus a limit on the obtainable accelerating fields when using a single driving bunch.

2.2.3 Wakefields by a cut Gaussian driving beam

For the SPS proton bunch used in AWAKE the condition $\sigma_\zeta k_p = \sqrt{2}$ sets a limit for the plasma density and thus for the largest wavebreaking field in the plasma. With the SPS parameters the wavebreaking fields are $10-75 MV/m$ ($\sigma_\zeta = 200-400 ps \cdot c$) corresponding to plasma densities of $0.1 - 6 \cdot 10^{11} cm^{-3}$. This is far lower than the mentioned $\sim GV/m$ accelerating fields. Increasing the charge in the bunch by two orders of magnitude is not possible, but the wakefields can be increased by cutting the Gaussian driving bunch. In the limit of a very long Gaussian bunch that is zero for $\zeta < 0$ (a "cut" bunch with $|\zeta| << \sigma_\zeta$) one can expand the Gaussian shape of the bunch up to first order and obtain

$$W_\perp \sim R' \left(\frac{1}{k_p^3 \sigma_z^2} \left(1 - \cos(k_p \zeta)\right) - \left(\frac{\zeta}{\sigma_\zeta}\right)^2 \frac{1}{k_p^3} \right) \tag{2.30}$$

$$W_\parallel \sim R \sin(k_p \zeta) \tag{2.31}$$

The initial wakefields in a long bunch are accelerating and decelerating for the parallel component and the perpendicular wakefields are positive with the minima being only

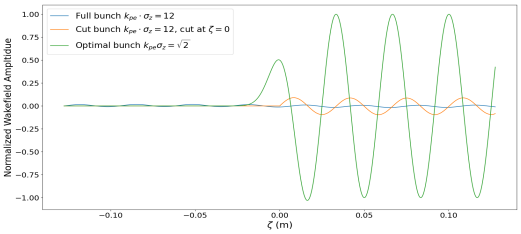

Figure 2.2: Longitudinal wakefields on axis excited by three types of bunches with a plasma density of $1 \cdot 10^{12} cm^{-3} \leftrightarrow k_p = 188 m^{-1}$. An optimum bunch with $k_p\sigma_z = \sqrt{2}$ (green line), a very long bunch (blue line) and a long but cut bunch (orange line). The amplitude is normalized to the maximum amplitude of the optimal bunch. The wakefield amplitude is suppressed for the long bunch but a cut one can enhance the excited wakefields from $\sim 2\%$ of the optimum wakefields to $\sim 9\%$ of the wakefields of the optimum driver (for the chosen parameters).

slightly defocusing. Fig.2.2 shows that sharp cut can induce large wakefields even when the bunch does not fulfill $k_p\sigma_\zeta = \sqrt{2}$. The figure shows three cases. The wakefields for a Gaussian bunch with $\sigma_\zeta = \sqrt{2}/k_p$ (an optimal driving bunch), a Gaussian bunch with $k_p\sigma_\zeta = 12$ (a long bunch) and a bunch that has $k_p\sigma_\zeta = 12$ but is cut in the middle. All bunches except for the cut bunch have the same total charge but the cut one has only half the charge. Clearly visible for the longitudinal wakefields is that the wakefields from the long driver are small ($\sim 1\%$) compared to the optimal driver. The long but cut beam with half the total charge excites wakefields that reach an amplitude of up to $\sim 9\%$ of the optimal one. This allows to start the wakefields at a certain position and phase within the bunch. The magnitude of the wakefields is enhanced w.r.t. the long bunch. In AWAKE the cut is experimentally done by the high-power laser pulse that is used to create the plasma within the bunch. This enhances the wakefields but still does not reach the GeV wakefields scale. To reach the GeV wakefield scale the interaction of the plasma with the bunch has to be considered.

2.3 The beam envelope equation

So far the beam has been considered as an external source that only disturbs the plasma and excite a wave that oscillates with the plasma frequency. In [41] the equation for the beam root mean square radius (RMS, $R = \sqrt{< r^2 >}$) is given for a bunch that is moving through a medium with energy transfer rate ϵ' is developed.

$$\ddot{R} + \frac{1}{\gamma}\dot{\gamma}\dot{R} + \frac{U}{R} + \frac{\omega_c^2 R}{4} - \frac{C^2}{\gamma^2 R^3} = \frac{1}{\gamma^2 R^3}\int_0^t dt' \left(\frac{2\gamma R^2 \epsilon'}{m_p}\right). \tag{2.32}$$

This equation assumes a self similar beam of the form $f_r \sim F(r/R)$. The constant $C^2 = \epsilon^2 + P_\theta^2$ is the emittance of the beam when the angular momentum of the beam is zero. Note that the emittance here has units $\frac{mm^2}{s}$ which coincides with the standard units $mm - mrad$ when changing from a time description to a propagation distance description. The constant ω_c is enforced by an external magnetic field $\omega_c = \frac{q_p B}{\gamma m_p}$ and U is related to the self focusing of the beam. For a Gaussian bunch $R = \sqrt{2}\sigma_r$ and $R = \frac{a}{\sqrt{2}}$ for a flat beam with radius a. Since the beam envelope at position ζ depends on the beam envelopes of earlier ζ' the complete equation is a retarded functional differential equation. When the beam is propagating without interaction, with $\gamma = const$ and no macroscopic forces act on the beam, $U = \omega_c = 0$, the beam evolves as

$$\frac{d^3}{dt^3} R^2 = \frac{4\epsilon'}{\gamma m_p} \tag{2.33}$$

which has the solution $R^2 = R_0^2 + V_0^2 (t-t_0)^2 + \left(\frac{\epsilon'}{3\gamma m_p}\right)(t-t_0)^3$ [41]. Here $V_0^2 = C^2/(\gamma^2 R_0^2)$ is the initial beam velocity and R_0^2 the initial beam radius. When taking into account the wakefields, the longitudinal wakefields are ignored as the beam is highly relativistic and it is assumed that it does not loose much energy over the course of the beam plasma interaction. To see why this simplification is acceptable one can assume that protons within the bunch are always in a decelerating phase with the wave breaking amplitude during the interaction with the wakefields. The wave breaking field for the highest possible AWAKE Rubidium plasma density of $\sim 11 \cdot 10^{14} cm^{-3}$, is $3.1 GV/m$. The protons lose at most $\Delta E = 31 GV$, corresponding to $\Delta\gamma = 31$, over the $10m$ of plasma. The shift $\Delta L = L \cdot \frac{1}{\gamma^2}\frac{\Delta\gamma}{\gamma}$ due to the deceleration of the protons is less than $10\mu m \ll \lambda_{pe}$ which means that the longitudinal movement is of second order. The transverse momentum of the proton bunch particles on the other hand is initially small. Calculating the velocity of the protons from the AWAKE bunch parameters assuming a emittance of $2 \cdot 10^{-6} mm - mrad$, one finds that the protons in the AWAKE bunch have a corresponding radial velocity of $V_0 \sim 11 km/s$. This corresponds to a transverse momentum of $\sim 1 eV/c$. Numerically evaluating eq.2.29 for a half cut AWAKE bunch and a plasma density of $1 \cdot 10^{14} \frac{\#}{cm^3}$ already gives wakefields in the MeV/m range (the perpendicular wakefields are just scaled by the value of $R'(r)$), which shows that the wakefields excited in low density plasmas are much larger than the initial transverse momentum from the emittance (the C^2/γ^2 term in 2.32). The effect of the transverse wakefields $W_\perp = (E_r - B_\theta)$ on the bunch can be taken into account by setting $U = \frac{e^+}{m_p \gamma} < W_\perp \cdot r >$ [41]. Keeping this term in 2.32 the resulting beam envelope equation for every slice at position ζ within the beam, caused by the transverse wakefields $W_\perp$, is then given by

$$\ddot{R} - \frac{C^2}{\gamma^2 R^3} + \frac{e}{R\gamma m_p} \int_0^\infty dr\, r^2\, f_r(r,\zeta)\, W_\perp(r,\zeta) = \frac{1}{\gamma^2 R^3} \int_0^t dt' \left(\frac{2\gamma R^2 \epsilon'}{m_p}\right). \tag{2.34}$$

The implicit ζ dependence of R has been omitted. When the equation is written out it reads as

$$\ddot{R} - \frac{C^2}{\gamma^2 R^3} + \frac{Qe^2}{R\gamma m_p}\frac{k_p^3}{\epsilon_0}\int_0^\infty dr r^2 f_r(r,\zeta)\int_{-\infty}^{\zeta}\cdot\sin\left(\frac{\omega_{pe}}{c}(\zeta'-\zeta)\right)d\zeta'\times \left(K_1\left(\frac{\omega_{pe}r}{c}\right)\int_0^r r' f_r\left(\zeta', r'\right) h\left(\zeta'\right)\mathrm{I}_0\left(\frac{\omega_{pe}r'}{c}\right)dr'\times -I_1\left(\frac{\omega_{pe}r}{c}\right)\int_r^\infty r' f_r\left(\zeta', r'\right) h\left(\zeta'\right)\mathrm{K}_0\left(\frac{\omega_{pe}r'}{c}\right)dr'\right) = 0. \tag{2.35}$$

Again no external magnetic field is considered and f_r is the radial bunch distribution. The effect of scattering can also be neglected as the forces from the wakefields will be much stronger than any additional scattering thus the r.h.s. of eq.2.35 is zero. Equation 2.35 describes the beam envelope under the influence of a self-excited wakefield in a plasma. The right hand side of eq.2.35 is only a function of $R(\zeta)$ because all dependencies of r and $R(\zeta')$ are integrated out. This equation only describes the mean square radius $R(\zeta)$ of the beam envelope, but this influences the beam charge distribution so it becomes a charge distribution $f(r/R(\zeta))h(\zeta)$. This distribution then influences the excited wakefields as the beam charge density appears within the integrals. Note that the beam charge density is determined by the equation for the radius and it was assumed that the functional shape of the charge distribution does not change so only a parameter of the distribution does change. To obtain the wakefields it is necessary to solve eq.2.35 and then calculate the transverse and longitudinal wakefields for the resulting beam distribution with eq.2.22 and eq.2.23.

2.3.1 Numerical solution of the beam envelope equation for a flat top beam

Equation 2.35 is difficult to solve analytically. For a flat top bunch $f_r = \frac{1}{2\pi R^2}, r < a,\ 0$ else (again R is the RMS radius and a is the "cut radius") a fast numerical solution was developed. The solution to the radial wakefield given by eq.2.25 can be written down explicitly (in terms of the RMS radius R) as

$$\begin{aligned} r \geq a : R' &= K_1(k_{pe}\cdot r)\cdot I_1(k_{pe}\cdot\frac{R}{\sqrt{2}})\cdot\frac{R}{2\sqrt{2}\pi k_{pe}R^2} \\ r \leq a : R' &= K_1(k_{pe}\cdot\frac{R}{\sqrt{2}})\cdot I_1(k_{pe}\cdot r)\cdot\frac{R}{2\sqrt{2}\pi k_{pe}R^2}. \end{aligned} \tag{2.36}$$

This is much easier to handle but because of the $R(\zeta')$ dependence, the double integral over the transverse wakefields is hard to solve analytically. The resulting equation now

reads

$$\ddot{R} - \frac{C^2}{\gamma^2 R^3} + \frac{Qe^2}{R\gamma m_p}\frac{k_p^2}{\epsilon_0}\int_0^a dr \frac{r^2}{R(\zeta)^2}\cdot dr\int_{-\infty}^{\zeta} h(\zeta')\cdot\sin\left(\frac{\omega_{pe}}{c}(\zeta'-\zeta)\right)d\zeta'\times K(r,R,\zeta',a) = 0. \tag{2.37}$$

where $K(r, R, \zeta, a)$ is given by eq.2.36. After bringing the term that corresponds to $\frac{U}{R}$ term on the right hand side of eq.2.32, the left hand side is a second order differential equation. The right hand side is the retarded functional term. In order to numerically solve the equation, the longitudinal distribution h of the bunch is approximated with small constant parts (approximate the longitudinal distribution as if one would do Riemann integration). For each of these constant approximations the ζ' integral can be solved analytically as now R is considered a constant over this small region ζ. The ζ wakefield integral Ψ of a constant (starting at position ζ_0 and ending at $\zeta_1 = \zeta_0 + \mathrm{d}\zeta$) is then given by

$$\Psi = \frac{1}{k_p}\cdot(\cos(k_p\cdot(\zeta-\zeta_1)) - \cos(k_p\cdot(\zeta-\zeta_0))). \tag{2.38}$$

Each of the slices is considered short enough that it does not interact with itself. The first slice of the bunch then does a free propagation according to Eq. 2.33 which was solved with a Runge-Kutta 4-5 solver. This slice then generates wakefields according to eq.2.36 and eq. 2.38. For the next slice the wakefields are now known for all times and thus a numerical integration of the wakefield part can be done. This results in the r.h.s. of eq.2.32 is now numerically given as $\frac{K_{mean}(t)}{R}$. The resulting equation for the propagating slice i is then

$$\ddot{R}_i - \frac{C^2}{\gamma^2 R_i^3} + \frac{e^2}{R_i\gamma m_p}\frac{k_p}{\epsilon_0}\sum_{j<i}\int_0^a dr\frac{r^2}{R_j^2}I_1(k_{pe}\cdot r)Q_j\cdot\Psi_j(i)\times K_1(k_{pe}\cdot\frac{R_j}{\sqrt{2}})\cdot\frac{1}{2\sqrt{2}\pi R_j} = 0 \tag{2.39}$$

and can again be solved with a Runge-Kutta 4-5 method. In this equation the sum term corresponds to the known wakefields from the previous slices which sums and integrates to the known $K_{mean}(t)$. Further Q_j is the charge of the slice j and $\Psi_j(i)$ is the value of the longitudinal wakefield of slice j at position i. R_j is the value of R of slice j at time t. Note that only the radial wakefield part for $r < a$ is needed as the average will not extend further than a (the density is 0 for $r > a$). After the slice is propagated, the new wakefields created by the slice according to eq.2.23 are stored and used in the propagation of later slices. The loop continues to go over all slices until the last slice has propagated through the plasma. A visual representation of the solution process is given in fig.2.3 where the loop is shown for the first slice. Note that in the figure the bunch is

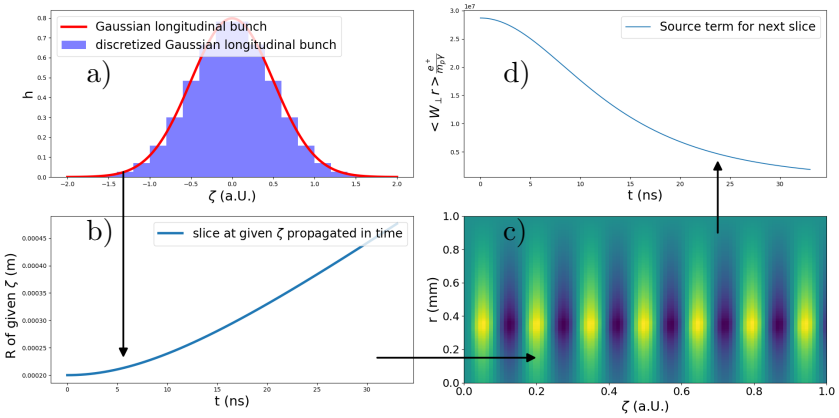

Figure 2.3: Flowchart for the solution of the radius evolution equation 2.35. Starting at a) the longitudinal beam distribution is discretized into constant step functions. The first slice is then selected and propagated according to Eq.2.33. The radius R of the beam changes over the propagation time as seen in b). The slice creates wakefields for each t and they are calculated by using Eqs. 2.36 and 2.38. The resulting wakefields c) are stored and the term $\frac{U}{R}$ is calculated from the excited wakefields for each time-step d). Now for the next slice the driving term in Eq.2.39 is known and can be used to propagate the second slice through the plasma. The excited wakefields of the second slice are added to the wakefields of the first slice. The loop continues until all slices are propagated.

not cut, however the algorithm allows also cut bunches to be propagated. It is also not necessary to use flat top bunches. The same principle can be used to propagate arbitrary radial distributions, yet the analytical solution of the two innermost integrals in eq.2.35 speeds the process up by orders of magnitudes. Using Gaussian radial distributions brings little additional benefit (for this work) over the flat top bunch.

2.3.2 Discussion of the model

It must be stated clearly that this model is only a qualitative view of the self-modulation process. The model ignores any variations in the plasma density. Albeit linear density ramps could be included, the complexity of the model increases by a large amount. Also the beam is considered as self-similar which is not true, it is not only the beam RMS that gets modulated but also the mean proton radius becomes modulated in the self-modulation which is ignored in this model. Last but not least the emittance of the beam slices is conserved which is a shortcoming of the model as the emittance of a bunch increases in nonlinear radial fields and so the expansion of the beam after the plasma will clearly be underestimated.
The model is well behaved for small R because $\frac{Qe^2}{m_p\gamma} < W_\perp r >$ behaves as $\sim \frac{1}{R}$. This means that the emittance driven expansion will always dominate a possible beam pinch. Also the wakefields do not propagate due to thermal effects($T = 0$). Despite all these shortcomings the model is still able to capture the qualitative behavior of the beam (see next section) and gives a significant basic understanding of the processes that happens.

2.3.3 The self-modulation of a long proton beam

In the preceding sections it was presented that in linear theory a beam with length $k_p\sigma_z = \sqrt{2}$ is needed to excite the largest wakefield amplitude. Further a bunch is influenced by the wakefield it creates, so the bunch is not a static driver but evolves in time. A model is presented that accommodates for these effects and a way to solve the equations of the model is given. It was suggested to use a very long proton bunch to drive wakefields with high plasma densities and rely on the self-modulation instability that allows the use bunches such as the SPS one for high energy acceleration [42]. In this instability a very long bunch breaks into smaller micro-bunches with distance $\sim \lambda_{pe}$. The qualitative model from section 2.3 shows the same behavior. To show this a half cut proton bunch with the AWAKE parameters ($\sigma_z = 400ps \cdot c$, $R_0 \sim 0.2mm, C = 3.5 \cdot 10^{-6} \cdot c, Q = 3 \cdot 10^{11}$) is sent into a plasma with a density of $7 \cdot 10^{14} cm^{-3}$. This corresponds to a plasma wavelength of $1.26mm$. The method presented to solve eq.2.35 is applied to the beam that is cut into 200 slices where each slice has a length of $100\mu m$. This corresponds to $\sim$ 12 slices per plasma wavelength. The beam is propagated for $33ns$ which corresponds to the $10m$ plasma that is used in AWAKE. The time step resolution for the runge-kutta solver is starting at $10^{-11}s$ and is variable during the integration procedure. The radial resolution is $15\mu m$ and the number of radial grid points is 200. The beam is not completely covered by the grid in ζ direction, but to see the self-modulation it is enough to look at the beginning of the bunch.

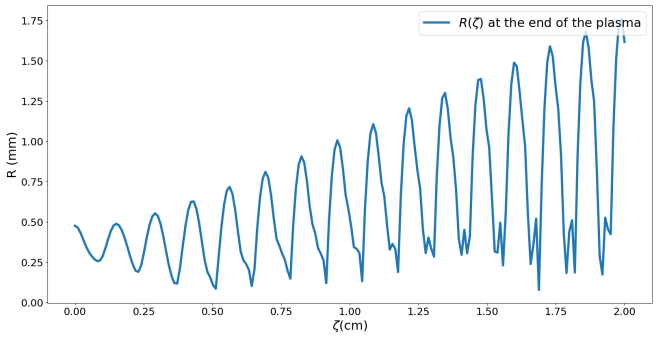

Figure 2.4: The radial distribution $R(\zeta)$ of a cut AWAKE bunch propagated through 10m of plasma. Clearly visible is that the bunch has no longer a constant radius but rather a modulated one. After the plasma the bunch consists of short regions where the beam is focused and de-focused between those regions. The distance between the focused beamlets (the valleys of the radial modulation) is close to the plasma wavelength λ_{pe}.

The resulting $R(\zeta)$ after the plasma is shown in fig.2.4. Clipping the fields to the wavebreaking field does not change the solution as the mean fields do not reach E_{wb} for the part of the bunch considered. Thus clipping was not applied. Clearly visible is that the first slice (the one that propagated without any wakefields present) has a radius that is predicted by the emittance of the bunch ($\sim 0.5mm$). The initially focusing wakefields focus a short part of the bunch, then R starts to oscillate and the bunch breaks into beamlets with distance λ_{pe}. This is the fundamental idea of the AWAKE experiment. To use a long proton bunch and let it break into small beamlets with length $\leq \lambda_{pe}$ that can then drive large amplitude plasma waves. Shortening the cut bunch to $200ps$ but keeping the total charge constant leads to an stronger growth of the radial modulation, such that the bunch exceeds the simulation grid in radius.
A note of interest is that the model also shows that the wakefields do not propagate with the same velocity as the bunch. This is a feature that is also observed in more complex models (see e.g. [43] fig.4). This can be seen in fig.2.5 where the term $K_{mean}(t)$ in eq.2.39 for all t and ζ is shown. The term corresponds to $W_{\perp Long} \cdot W_{\parallel Long}$ averaged over the beam distribution. If the wakefields propagate with the same velocity as the bunch, the stripes in fig.2.5 would be parallel to the y axis. But it is clearly visible that at the beginning of the self-modulation process the stripes are curved backwards and only approach the parallel to the y axis for later times. This means that a focused part of the bunch can fall into a defocusing part with increasing propagation time and this model predicts that the beam breaks up into small beamlets that then slide into a defocusing region and become shorter and shorter. This means that the charge that drives the plasma waves become smaller and smaller over time. This model predicts that this will not "eat up" the micro-bunches in AWAKE for the planned densities. This

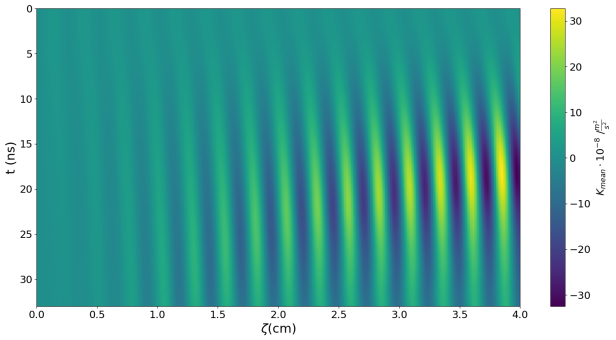

Figure 2.5: The term K_{mean} with AWAKE basseline parameters for each slice and all times is shown. It can be seen that the focussing and defocussing terms grow along ζ and t. Interesting to note is that for a fixed slice (and therefore fixed ζ) the phase of the K_{mean} term is not constant but moves (the slope of the oscillating lines).

means the micro-bunches are still intact after the beam-plasma interaction.

2.3.4 Comparison with quantitative LCODE Simulation

In the qualitative model above the bunch develops into micro-bunches with a distance of λ_{pe} (corresponding to a time difference of $1/f_{pe}$) and the current is conserved. To develop a diagnostic the qualitative nature of the radius in the model is problematic. For quantitative results simulations by LCODE [44] were used. LCODE[1] is a freely distributed quasi static code for simulating beam-plasma interactions. It is developed by K. Lotov and his team at the Budker Institute of Nuclear Physics in Novosibirsk and is one of the standard simulation tools in AWAKE[45]. The output of a AWAKE baseline simulation[2] with a plasma density of $7 \cdot 10^{14} cm^{-3}$ and AWAKE baseline parameters [39] has been propagated for 3m in free space after the plasma and analyzed. The 3m free space propagation was used because the LCODE bunch will serve as source model for the detector which is located $\sim$ 3m behind the plasma exit. In fig.2.6 the current of a proton beam after 10m in plasma is shown together with a beam that was not interacting with a plasma as produced by LCODE. The curve shows that the total current of the bunch that interacted with the plasma is not modulated. The beam that propagates in free space also has no current modulation. In fig.2.6 the beam current is shown when one takes the modulated beam and selects only the particles within $0.5mm$ radius. The beam current becomes strongly modulated and the periodicity of $\lambda_{pe} = 1.26mm$ appears in the current.
Cutting the bunch along the x-axis shows only a thin slice but this slice conveys the in-

[1] https://lcode.info/main.html
[2] Thanks to K.Lotov and A.Petrenkov for the simulation

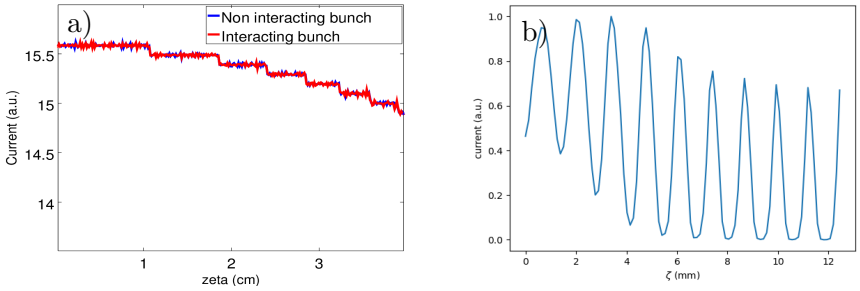

Figure 2.6: a) Total bunch current for a modulated (red line) and un-modulated (blue line) proton bunch. The negligible difference shows that the total current is not modulated. Only the first $4cm$ of the bunch are shown. The bunch current step granularity is from the simulation input current.
b) The beam current when only particles within $0.5mm$ radius are considered. The current is now heavily modulated with a period of $\lambda_{pe} = 1.2mm$

formation about the dependency $R(\zeta)$ of the bunch in LCODE. In Fig.2.7 the normalized cut out is shown. The LCODE simulation shows that bunch becomes heavyly modulated directly behind the cut. The comparison between the LCODE R and the R from the model shows that the model is able to give a qualitative view of the self-modulation process. The LCODE bunch has a maximum R that is comparable to the solution of beam envelope equation but the semi-analytical solution seems to overestimate the actual radius of the bunch. It is interesting to note that the modulation frequency of R of both simulations do not match and the semi analytical model has a slightly larger modulation spacing than the LCODE simulation.
The LCODE shows two very important features of the self-modulation:

- The self-modulation is current conserving (only a transverse modulation!)
- The self-modulation transforms the central part of the beam into micro-bunches with distance λ_{pe}

The second point is very important as these micro-bunches drive the wakefields resonantly and thus very efficiently. The cut bunch that excites initially smaller wakefields than the optimal length bunch breaks up into micro-bunches. These micro-bunches have close optimum bunch length and they drive the plasma resonantly. This leads to an exponential growth of the wakefields along the bunch and the wakefields can reach up to the wavebreaking field later in the bunch. The mentioned phase slippage of the wakefields with respect to the bunch limits the effect of the resonant driving but the qualitative model and quantitative simulations show that the phase slippage does become nearly zero at some time in the plasma and the resonant driving of the wakefields can occur. The detection of the self-modulation and these micro-bunches are therefore an important step in AWAKE!

a) b)

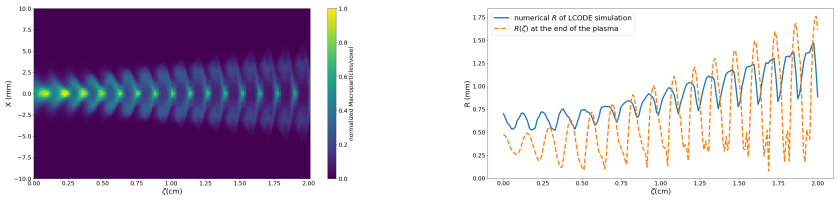

Figure 2.7: a) Cut out of the LCODE bunch output. Each macroparticle is assigned a random phase between $(0, 2\pi)$. Then the position of the macroparticles are calculated in x,y and z direction. A grid with a resolution of $\lambda_{pe}/10$ in z direction and $0.1mm$ in x and y direction is applied and the density of the beam is calculated. The resulting beam distribution is normalized to the maximum. Only the first $2cm$ of the bunch are shown.
b) From the bunch slice in a) the numerical value of $R = \sqrt{< r^2 >}$ is calculated along the z grid direction (blue line). For comparison the R value from the developed model in fig.2.4 is shown in the same plot (orange line).

2.4 Conclusion

The qualitative analysis of the self-modulation and its seeding have shown that the proton bunch will retain most of its energy in its self-induced longitudinal wakefields. We expect the proton beam to have only a radial modulation but no longitudinal density modulation. This prediction coincides with PIC simulations. The radial modulation can become very large ($> mm$) but all longitudinal features of the modulated bunch are expected to be near the inverse plasma frequency. The large radial modulation is only expected to be seen in the late parts of the bunch ($> 2cm$ behind a cut). The radial modulation and the longitudinal characteristic are important characteristics that have to be considered in the diagnostics.

3 Bunch diagnostics for self-modulated bunches

In the preceeding chapter it was shown that the self-modulated beam is not longitudinally modulated but only radially. The most important feature are the central micro-bunches with a spacing given by the plasma wavelength. In this chapter possible beam diagnostics are discussed and Optical Transition Radiation (OTR) is chosen.

3.1 Requirements of the bunch diagnostics

A central aspect of this work is to develop a bunch diagnostics tool that can detect the formation of the self-modulation and the micro-bunches. The micro-bunches are only a few ps (from $\sim 10ps$ to $\sim 3ps$ for $n_{pe} = 1 \cdot 10^{14} - 10 \cdot 10^{14} cm^{-3}$) apart and thus a diagnostic with high temporal resolution is needed.
The bunch diagnostic should be able to detect the micro-bunches in a single event. The SPS sends only every $\sim 30s$ a bunch to the AWAKE experiment where the beam passes through the experiment and is then dumped towards Gran Sasso, Italy (so it will not come back).
Because the bunch is dumped after the diagnostics and no stations are planned behind the self-modulation diagnostic for the first few runs the measurement can be destructive. The diagnostics must be removable from the beamline for later electron acceleration and electron measurements. Note that the self-modulated bunch is already considered as destroyed/not usable for normal accelerators. A destroyed bunch means that the substructure of the bunch is no longer intact after interaction with the detector and the beam structure is significantly altered.
Finally the diagnostic should be proven. The implemented diagnostic is the main self-modulation detection tool. The first SPS beam came to AWAKE at the end of Dec. 2016 while this thesis started in mid 2014, so within three years the full instrumentation must be installed and working. There are also space constraints as the area behind the designated diagnostics space will be occupied by (is by now, 2022/2023) an electron spectrometer magnet. So only $\sim 2m$ of space are available along the SPS beamline. Perpendicular to the beamline or even further away more space is available but the signal needs to be transported there.

3.2 Overview of available diagnostic tool

In [46] an overview of standard beam measurement techniques is given and the most promising candidates are shown in table 3.1. Due to the self-modulation I want to measure a time-resolved, longitudinal and transverse image of the beam. A short discussion of the techniques and why they are fit or unfit follows.

Property measured / Technique	Pos.(transv.)	Size/shape(transv.)	Size/shape(longitud.)
Wall current monitor	y	n	y
Beam transformer	n	n	y
Secondary-Emission Monitors and similar	y	y	n
Scinitillator Screen	y	y	n
Pick up	y	y	y
Optical Transition Radiation	y	y/n	n/y
Synchrotron Radiation	y	y	y

Table 3.1: Overview of standard accelerator diagnostic technqiues and their primary use, table from [46]. The abbreviation y stands for yes and n for no. The y/n and n/y combination for transition radiation means that when a full size/transverse shape measurement is done with a camera no longitudinal measurement can be done (except when the bunch is very long).

Synchrotron radiation

Synchrotron radiation seems to be a natural choice because it can be used for longitudinal and transverse measurements [47]. In AWAKE there is no synchrotron radiation expected (even in the SPS there is no large amount of synchrotron radiation). This is because the protons are only bent by a small angle in the self-modulation process and emit negligible amounts of synchrotron radiation. Thus this method is not available.

Beam transformers, secondary emission monitors, wall current monitors and pick up

Beam transformers are a proven diagnostic but the self-modulation is only transverse so the total longitudinal charge distribution of the un-modulated bunch can only be distinguished if the beam transformer only picks up the core. This necessarily means that the rest of the beam hits the beam transformer which most likely destroys the transformer after a few shots. A further point against a beam transformer is that, if they only pick up the core, the setup is very inflexible. To pick up the core the setup must be very elaborate and the frequencies we want to pick up are in the $100's GHz$ range which is very hard to detect with radiation hard devices (if not impossible).

Secondary-Emission Monitors (SEM) rely on collecting the secondary electrons that are created when the beam hits a material. A SEM chamber can detect the transverse profile of a beam with resolution of down to 0.5mm [48] but the time resolution is too slow to measure the self-modulation frequency in AWAKE.
Wall current monitors also have the problem of the non modulated current, measuring up to $250GHz$ is possible but the total current is not changed by the modulation.
A pickup can detect bunch trains with a single bunch length of $\sim 1ps$ [49] but again these measurements rely on current modulation, which is not expected in AWAKE.

Scintillator screen and optical transition radiation

Scintillator screens (SS) and optical transition radiation (OTR) are proven measurement tools for measuring transverse beam profiles. While scintillators can be used to measure beams with length $\gg ns$, they do not offer a sub ns time resolution as the scintillation process has a characteristic timescale of μs. OTR on the other hand is prompt and thus has the same time structure as the bunch that creates the OTR. This means that OTR can be used to create a longitudinal profile. This has been done with streak cameras that sacrifice the transverse resolution by capturing all of the light from the bunch to get a very good $\leq ps$ time resolution (but only for short single pulses)[50]. A streak camera provides a time resolved measurement and all the expected frequencies are covered if the highest one can be detected.
Streak camera measurements need an OTR screen in the beamline. This screen can be thin and retractable so the measurement only slightly disturbs the proton beam and can be completely removed if needed.
Since the OTR diagnostic with a streak camera seems like a good candidate for the planned diagnostics, it was decided to investigate the feasibility of this method for detection of self-modulation and if a streak camera is able to detect the self-modulation.

3.3 Optical transition radiation in AWAKE

When a charge crosses the boundary between dielectric media (e.g. vacuum to a metal), the electric fields have to fulfill boundary conditions (i.e., for the parallel and perpendicular component of the electric field to the surface between the boundaries). When a charge moves towards and through a boundary, it emits transition radiation (TR) to fulfill these boundary conditions. For highly relativistic charges coming from vacuum into a foil and not too high radiated frequencies $\frac{\omega}{2\pi}$ (this means $\omega < \omega_{pe}$, where ω_{pe} is the plasma frequency of the metal) it is possible to model the TR using image charge theory [51], [52]. Assuming a charge coming from $z < 0$, having a velocity v perpendicular to the surface of a (infinitely thick) foil with normal vector $-e_z$, it is possible to model the electric fields with an image charge moving with -v at the imaged position -z. After the charge has entered the foil ($z > 0, \epsilon_r >> 1, \mu_r = 1$), its fields are completely screened and therefore there is no image charge any more. For an observer at $z < 0$ this looks like the charge and the image charge disappear. This can be modeled by decelerating the image charge from $|v|$ to 0 [53]. The power radiated per solid angle by instantaneously

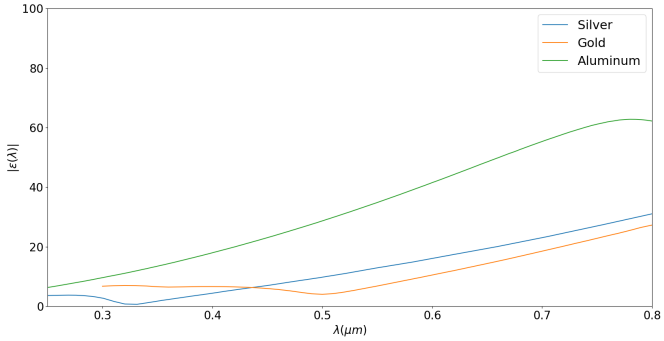

Figure 3.1: Absolute value $\|\epsilon(\lambda)\|$ for the three common reflective materials (Gold - orange line, Silver - blue line, Aluminum - green line). For the whole visible range $400nm$ to $800nm$ Aluminum has the highest reflectivity and is therefore chosen as reflective coating.

decelerated or accelerated charges is given by [54]

$$\frac{\mathrm{d}W}{\mathrm{d}\omega\mathrm{d}\Omega} = \frac{1}{4\pi c} \mid \sum_i q_i \left[\frac{\beta_{i2} \times \vec{n}}{1 - \left(\vec{\beta_{i2}} \cdot \vec{n}\right)} - \frac{\beta_{i1} \times \vec{n}}{1 - \left(\vec{\beta_{i1}} \cdot \vec{n}\right)} \right] \mid^2 \tag{3.1}$$

where the charge q_i is instantaneous accelerated from β_{i1} to β_{i2} and $\vec{n} = \frac{\vec{k}}{k}$ is the vector of observation.
When the charge hits an ideal mirror ($\|\epsilon(\omega)\| >> 1$ for frequencies in the range of interest - such that the mirror charge is $\sim -q_i$) all the power that is emitted from the charge in forward direction ($-e_z$) can be observed.
Since a streak camera detects visible light a highly reflective and flat material is needed. In fig.3.1 the dielectric constant is shown for three common reflective coatings. For this experiment the wavelength range is 400 to 500nm (as most streak cameras are most sensitive in this wavelength region) and only Aluminum has a relative permittivity of > 20 (corresponding to a reflectivity of $> 90\%$ for $45°$ incidence light) in this range of wavelengths, which makes it a good choice out of those three metals.
The penetration depth of visible light in Aluminum is less than $1nm$ and thus a very thin layer is enough. A $1\mu m$ thick layer of Aluminum on a silicon wafer substrate ($10cm$ diameter, $150\mu m$ thickness, evaporated by MicroFabSolutions, Italy) is used as the mirror foil. The roughness is $< \lambda/20$ for $800nm$ light which is still $< \lambda/10$ for the range $\geq 400nm$. The energy deposition of a full un-modulated AWAKE bunch leads to a temperature increase of less than $10K$ which gives enough time for the foil to cool down between the arriving bunches ($\sim 30s$)).

3.4 Energy of transition radiation

In this section the total amount of energy emitted by the proton bunch will be estimated. Using eq.3.1, the result for the power radiated into the half space $z < 0$ for a single charge and its image charge $\pm e$ is calculated as

$$\frac{\mathrm{d}W}{\mathrm{d}\omega \mathrm{d}\Omega} = \frac{e^2\beta^2 \sin^2(\theta)}{\pi^2 c \left\{1 - \beta^2 \cos^2(\theta)\right\}^2} \tag{3.2}$$

where θ is the angle between the observer and $-\vec{e_z}$. Therefore the total power that is radiated by an proton is, in this approximation, independent of ω, the frequency of the emitted light. This approximation is only valid for frequencies where the mirror can be treated as ideal [52]. The maximum of this distribution lies at $\theta = \frac{1}{\gamma}$ (seen from $1 - \beta^2 \cos^2\theta = 0 \rightarrow \cos\theta = \frac{1}{\beta} = \frac{1}{\sqrt{1-\frac{1}{\gamma^2}}} \rightarrow \theta = \arcsin(\frac{1}{\gamma}) \sim \frac{1}{\gamma}$), which becomes a small angle for large γ. In the AWAKE case $\beta \sim 0.999997$ for the $427GeV$ p^+ and e q.3.2 has a peak at an angle $\theta \sim \frac{1}{\gamma} = \frac{1}{427} \sim 0.14°$ which is very small. The total power radiated in the half space $z < 0$ is given by

$$\frac{\mathrm{d}W}{\mathrm{d}\omega} = \frac{e^2}{\pi c}\left\{\frac{1+\beta^2}{2\beta}\ln\left(\frac{1+\beta}{1-\beta}\right) - 1\right\} \tag{3.3}$$

corresponding to eq.3.2 integrated over $\int_0^{2\pi}\mathrm{d}\phi\int_0^{\frac{\pi}{2}}\mathrm{d}\theta$. Note that it seems that light collected from small angles (as the distribution eq.3.2 is sharply peaked around the angle $1/\gamma$) is enough to catch $\sim 90\%$. This is not true, one has to collect up to angles of $\sim 60°$ to collect $\sim$90% of the light. This is because of the $\sin(\theta)$ factor in $\mathrm{d}\Omega = \sin(\theta)d\theta d\varphi$ that increases the area at larger angles.
The amount of light emitted by transition radiation can be measured by the number of photons emitted per frequency. To calculate this one divides Eq.3.2 by $\hbar\omega$ [55], and after integrating over ω one obtains the number of photons radiated between ω_1 and ω_2 per angle as

$$N_{ph}(\theta) = \frac{e^2\beta^2 \sin^2(\theta)}{\hbar\pi^2 c \left\{1 - \beta^2 \cos^2(\theta)\right\}^2}\ln\left(\frac{\omega_2}{\omega_1}\right) \tag{3.4}$$

And thus the number of photons emitted into the half sphere between ω_1 and ω_2 is given by

$$N_{phot} = \frac{e^2}{\hbar\pi c}\left\{\frac{1+\beta^2}{2\beta}\ln\left(\frac{1+\beta}{1-\beta}\right) - 1\right\}\ln\left(\frac{\omega_2}{\omega_1}\right). \tag{3.5}$$

The streak camera uses a S20-ER photocathode with the maximum quantum efficiency at $450nm$. To limit chromatic dispersion in the optical system there will be a $25nm$ filter centered at $450nm$. Thus the frequency range under consideration is $\frac{\omega_2}{\omega_1} = \frac{462.5nm}{437.5nm}$. The velocity factor is $\beta = 0.999997$ ($\gamma = 427$) and $\frac{e^2}{\hbar c} \sim \frac{1}{137}$. This results in $N_{phot} = 0.0016$ photons emitted per particle.
The total number of photons emitted is then $4.8 \cdot 10^8$ (equal $\sim 0.2nJ$) for a beam with $3{\cdot}10^{11}p^+$. Although the total energy emitted is small, the peak power is still $0.2W$ due to

the short bunch that is only $\sim ns$ long. Despite the small total energy the OTR from this bunch can be detected with standard CCD/CMOS cameras[1]. The LCODE simulation and the developed model from 2 show that the micro-bunches have a radius comparable to the un-modulated bunch so if the streak camera can detect the un-modulated bunch, it is also able to detect the micro-bunches. The SPS bunch has been detected by streak cameras at CERN[2] so a Streak camera setup is possible. Streak cameras are sensitive to radiation. The self-modulated bunch is expected to create a lot of radiation. This means that the diagnostic must be placed behind a shielding as far away as needed and as close as possible to the beamline. With this constraint the main challenge will be to transport the OTR to the streak camera.

3.4.1 Justification of approximations

The expression for the transition radiation energy given in eq.3.2 is only valid when the screen has an infinite extent. When the screen is not infinitely large, but is a disk with radius d (as in AWAKE it is $10cm$), the radiated power has a correction term [56].

$$[1 - T(\theta, \omega)]^2 \tag{3.6}$$

where

$$T(\theta,\omega) = \frac{\omega d}{c\gamma} J_0(\frac{\omega d \sin(\theta)}{c}) K_1(\frac{\omega d}{c\gamma}) + \frac{\omega d}{c\gamma^2 \sin(\theta)} J_1(\frac{\omega d \sin(\theta)}{c}) K_0(\frac{\omega d}{c\gamma})$$

For $\omega d \sim \frac{2\pi c d}{\lambda} \gg 1$, T exponentially approaches zero [56]. In this experiment the foil has a diameter of $100mm$. For the considered wavelengths the finite size of the foil can be neglected since $d/\lambda \sim 10^5$ and an infinite foil is assumed.
The resulting angular power distribution in eq.3.2 is only valid when the charge is incident on the foil with a normal incident angle. For highly relativistic particles the effect of rotating the foil can be modeled by choosing a correct velocity vector for the image charge in eq.3.1. Such that the boundary conditions are still always fulfilled (i.e. the charge moves towards $-e_z$, the foil has a normal vector $\frac{1}{\sqrt{2}}(-e_z - e_x)$ for a foil with 45°, and the image charge has a velocity direction of $-e_x$). The result is that the transition radiation with this model is emitted as if the foil acted as a mirror with the reflection direction for the TR being 2φ (the direction θ is measured against), where φ is the tilt angle of the foil with respect to the incident electron trajectory. The angles for TR are usually small for highly relativistic particle. This provides a convenient way to decouple the TR from the proton bunch.

3.4.2 Optical transition radiation from a long bunch

So far only the energy of the TR of a single particle was considered. The TR pulse created by a particle has a spectrum corresponding to the Fresnel reflection coefficients

[1] personal communication with CERN and own experience
[2] Stefano Mazzoni CERN, personal communication

of the foil. Thus the length of a TR pulse can be very short because the spectrum is very broad and has a flat phase. For Aluminum the spectrum of the emitted TR pulse extends by the Fresnel reflection coefficients from the infrared region down to 400nm. This large bandwidth makes the TR pulse from a single particle extremely short and even suitable to detect even $\sim 50fs$ short electron bunches [57]. For a bunch as in AWAKE, the 1D current is given by $q_{p^+} \sum_i^N \delta(z - \beta ct)$, where we assume that each particle has the same velocity βc along the z direction. This is justified as $\beta \sim \beta_0(1 - \frac{\Delta\gamma}{\gamma^2})$, which is ~ 1 for $\gamma = 427, \Delta\gamma = 0.01$ as in the AWAKE case. Each particle emits the same electric field, but with some phase $\Phi_i = \omega z_i/\beta/c$. The power of the TR emission of this collection of N particles is the sum of the single bunch particle emission squared, which results in the total power radiated given by

$$\frac{\mathrm{d}^2 W_N}{\mathrm{d}\Omega \mathrm{d}\omega} = \frac{\mathrm{d}^2 W}{\mathrm{d}\Omega \mathrm{d}\omega} \sum_{i,j} \exp(-i\omega(\Phi_i - \Phi_j)) = \frac{\mathrm{d}^2 W}{\mathrm{d}\Omega \mathrm{d}\omega}(N + \sum_{i \neq j} \exp(-i\omega(\Phi_i - \Phi_j))) \quad (3.7)$$

The emission can be separated in a part that is proportional to the number of particles N (the incoherent TR, OTR) and a part that depends quadratically on the coherent sum of the phase difference between the particles in relation to the frequency of the emitted light (coherent TR,CTR). The quadratic dependency is because the coherent part has $N(N-1)$ summands. The power emitted by the CTR is described by a form factor, that is the absolute value of the Fourier transform of the bunch charge distribution squared. This form factor can be found by noting that for a large number of particles the single sum of the coherent and incoherent part can be replaced by the expectation value of the exponent $\omega(\Phi_i - \Phi_j)$. The contribution from the CTR is then $\sim N(N-1)\left|\int \mathrm{d}z f(z) \exp(-iz\omega/\beta/c)\right|^2$ which is the square Fourier transform of the longitudinal charge distribution in this case. In AWAKE the bunch length is long $(200 - 400ps)$ and thus the form factor is very low at optical wavelengths. Only the incoherent part, the OTR, contributes to the signal from the bunch while the coherent part does not contribute due to the exponentially damped form factor (at visible wavelengths!). The result is that the total power emitted is proportional to the number of particles and is from the single particles. This allows the use of OTR as a measurement in the AWAKE experiment to measure the bunch modulation frequency directly.

3.5 Streak camera as diagnostics tool in AWAKE

A streak camera has a time resolution down to 200fs in single events in the visible light frequency range. They are very sensitive devices that can detect low power signals. In the following paragraphs the operating principle and the streak camera is described. A light pulse is sent towards the input slit $(\sim 0 - 200\mu m)$ of the streak camera and then coupled to a photocathode by input optics. The light is converted to electrons and those electrons are accelerated in a vacuum tubes by an accelerating mesh. The bunch of electrons has the time structure of the light pulse in the longitudinal direction. In the transverse direction the electron stream has the same spatial structure as the light pulse along the slit. The slit is needed to ensure the time resolution of the camera.

After acceleration a time dependent electric field is applied perpendicularly to the slit. The field deflects the electrons. The longitudinal structure is converted into a vertical structure, while the structure along the slit is not changed (a too large slit creates a large vertical structure). Then they hit a electron multiplier (Multi Channel Plate, MCP) and behind the MCP the electrons are converted back to light. This light is imaged onto a CCD camera.
A streak camera has a MCP, a photocathode and a sensitive camera attached so it is not radiation hard. The self-modulated proton bunch creates a lot of secondary radiation and the environment near the beamline is not suitable for a streak camera to be placed. This means that the OTR created from the foil in the beamline must be transported to the streak camera that is located in a shielded place.
The streak camera converts the time structure of the light pulse into a spatial structure along the axis of deflection and measures intensity vs time.
The streak camera can only achieve its best time resolution when it takes a very short image ($\leq 100ps$). The streak camera can take longer snippets (up to ns), however the time resolution is proportional to the time window length (a good estimate for the time resolution is $\sim 1\%$ of the time window[3]). The streak camera has a photocathode which has its highest sensitivity between 400 and $500nm$ with its maximum at $450nm$.

In the case of AWAKE the slit acts in two ways. Firstly it ensures the time resolution of the camera to be good enough to detect the micro-bunches ($3 - 10ps$). Secondly the slit acts as a mask if an image of the OTR is formed at the entrance slit plane. This mask allows only a selected plane of the OTR light through the slit and then a time resolved image of this plane is taken. A quantitative analysis is done by propagating two proton bunches with LCODE. The first one does not interact with the plasma and propagates in free space. The second one interacts with the plasma of density $7 \times 10^{14} cm^{-3}$ over ten meters. The bunch is half cut in both cases. The bunches are propagated for three meters in free space after the plasma. This is the approximate distance between the plasma exit and the planned diagnostics place in the experiment. The same procedure as in section 2.3.4 is applied to create a discretized 3D bunch density. Fig. 3.2 shows the expected streak camera image assuming a 1:1 imaging system, detection of all photons (this is an idealization) and a time resolution of $\leq 1ps$. Only the beginning $2.5cm$, corresponding to $83ps$, of the bunch are shown and the slice thickness is $180\mu m$. The results in fig.3.2 b) show that modulation of the bunch is strong enough that most protons are defocussed shortly behind the seed point. Clearly visible are the micro-bunches from the self-modulation. The slice of a non central cut is shown in fig.3.2 c) where the slice is taken $750\mu m$ away from the bunch axis. The signal strength is less than the signal from the central slice and there are no focused micro-bunches from the self-modulation visible. The rings from the defocused protons are now visible. The frequency of the rings is the same as the frequency of the micro-bunches, but shifted by the phase $\sim \pi$ in phase with respect to the micro-bunches. When slicing the cylindrical bunch the 2d structure of the bunch that carries information about the micro-bunch structure can be

[3]Hamamatsu, Personal communication

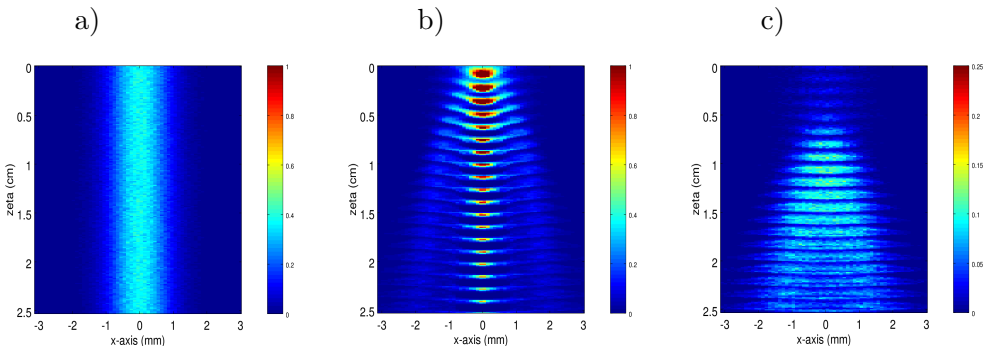

Figure 3.2: a) Bunch from a LCODE simulation propagating without plasma interaction for 13m. No charge modulation is visible as expected. b) Slice on axis of the proton charge density, and thus OTR photon density, of a beam propagating in 10m of plasma and then three meters without plasma. The beam is a half cut beam with the cut in the middle. Clearly visible are the micro-bunches that are forming behind the cut that is at the top at $0ps$. The defocused protons are also visible. c) Slice with $750\mu m$ offset from the axis. There are no longer focused micro-bunches visible but there is still the same periodicity in the OTR as in the on axis case. Notice the different color-table in c). The plasma electron wavelength in the modulated case is $1.2mm$.

seen. A time resolved measurement of the slice makes the information visible.

3.6 Conclusion

Streak cameras and OTR are proven and reliable bunch diagnostic tools. For AWAKE they fulfill all demands that are considered. An analysis of the OTR power radiated by the bunch shows that the OTR light emitted has an energy of $> 100pJ$ (depending on the wavelength range that is considered). From personal communication with CERN this amount of light should be detectable on a streak camera. This will be examined in the next chapter. The properties of the streak camera together with the property of the OTR allow a time resolved measurement of the micro-bunches and of the bunch time structure in general. This leads to the measurements realized in this thesis:

- Block the high power laser pulse that creates the rubidium plasma with a beam-dump. This beamdump was implemented by M. Hüther.
- Insertion of an Aluminum coated wafer in the bunch path to generate OTR with the same space and time structure as the proton bunch
- Image the OTR on the input slit of the streak camera that selects a thin slice of the OTR along the bunch propagation axis and blocks all light from outside

- Usage of a streak camera to create a time resolved image of the thin slice and measure the period of the micro-bunches and many other properties of the self-modulation process.

The resulting streak image shows the focused micro-bunches as in fig.3.2. The frequency measurement of the modulated bunch is independent of the exact slice that is cut out. All components of the diagnostics are well known but the challenges for the diagnostics lie in two facts. Firstly there must be enough light transmitted to the camera (the losses in the imaging system must not be too high - what is too high will be determined). The structure of the proton bunch must be maintained between plasma and OTR screen. This is needed since the area around the beamline will be showered by secondary particles (and to some extent even by the self-modulated bunch) and this is not a fit environment for a sensitive device[4]. The streak camera cannot be situated near to the proton beam and a minimum distance of $\geq 10m$ to the proton bunch must be overcome. The optical system to transport the OTR light will be discussed in Chapter 5. Secondly, streak cameras are typically used for short, single pulses. The signals that are expected in AWAKE have a substructure that has a short period ($\sim ps$) but the signal itself is very long ($\sim ns$, see fig.3.2). This is an unusual use for a streak camera and it was not clear whether streak cameras still obtain high resolutions for long signals with a short structure[5]. It will be investigated in the next chapter whether a streak camera is able to resolve ps structures in a long signal.

[4]Standard CCD cameras that were placed near the SPS beamline did not survive very long (died between a few events and one week)

[5]The vendors would not guarantee ps resolution with such a long signal.

4 Streak camera suitability

In chapter 3 a diagnostics for the detection of the self-modulation was presented. A central piece in this diagnostics is a streak camera to take the time resolved images of the proton bunch OTR light. Streak cameras have a best time resolution between $200fs$ and $2ps$ but they usually achieve this time resolution only when a single short pulse is sent into the device. If pulse trains are used, the camera is operated in synchroscan mode or the pulse distance is larger than the time resolution of the camera [58]. As stated in sec.2.4 one streak camera vendor pointed out that they are not sure if a streak camera is able to detect a long modulated signal. This chapter will show that streak cameras are a suitable device to detect the modulation in the AWAKE experiment. The results of this chapter have been published as "GHz modulation detection using a streak camera: Suitability of streak cameras in the AWAKE experiment", Review of Scientific Instruments 88, 025110 (2017) https://doi.org/10.1063/1.4975380".

4.1 Experimental test setup to measure streak camera time resolution

A 420 GeV proton bunch would be needed to give a definite answer to the question whether streak cameras are able to detect a $4ps \sim 250GHz$ modulated OTR light signal. Because there is currently (and even in near future) no 420 GeV proton beam at the Werner-Heisenberg-Institute to produce the desired OTR, it was decided to use an experimental setup that can simulate the (modulated) OTR light expected from the proton bunch.
The principle idea to simulate the OTR light from the proton bunch is to modulate a laser pulse with the frequency that is expected from the OTR light of the bunch. This is done by using two lasers with slightly different frequencies and send them both onto the photocathode of a streak camera. The photocathode of a streak camera is in general sensitive to the intensity of the incoming light. This can be used to create a signal which is modulated at 250 GHz by using the fact that for two plane waves $E = E_0 \cos(\omega_1 t + \delta) + E_1 \cos(\omega_2 t)$ the power (and therefore also the intensity) is modulated at the difference frequency $\omega_1 - \omega_2$. When the difference frequency of the two lasers corresponds to the $50 - 250GHz$ of the expected modulation in the AWAKE experiment, the signal that the streak camera detects can be simulated. This light has the same modulation structure as the OTR light from the proton bunch. The streak camera photocathode is only sensitive in the range $400nm - 850nm$ and no two lasers that produce light in this range were available, so an alternative setup to create the beating intensity was needed.

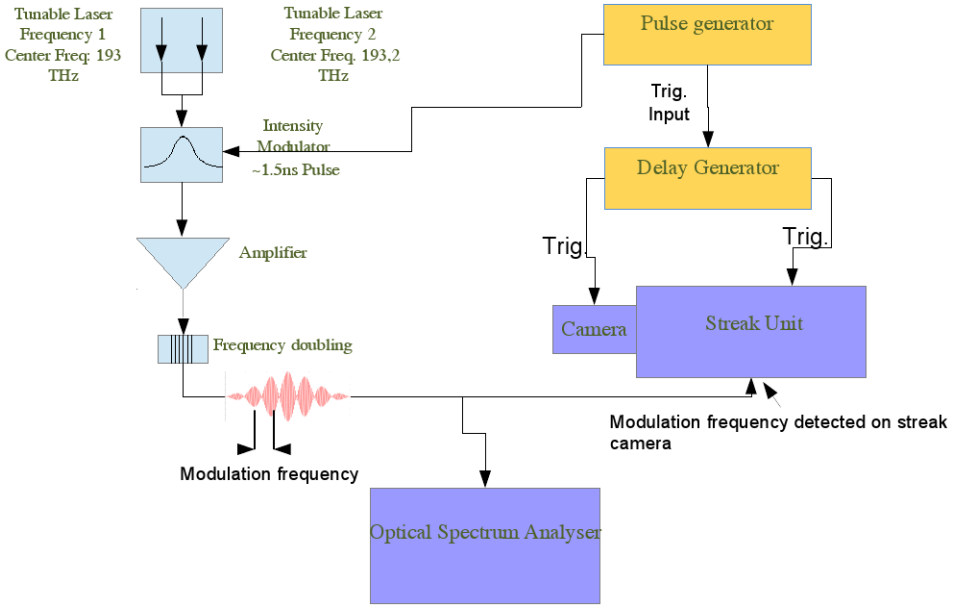

Figure 4.1: Experimental layout of the streak camera test in the laboratory.

4.1.1 Intensity beating with frequency doubling

Two tunable cw lasers (Thorlabs, TLX series) with center frequency $193THz \leftrightarrow 1554.4nm$ and $193.2THz \leftrightarrow 1552.8nm$ were available and their frequency doubled wavelength lies in the detection range of streak camera photocathodes. A test setup was built to create a laser pulse with intensity beating as the OTR in AWAKE. The general setup is shown in fig.4.1. The idea of the experiment is to combine the two lasers and to create a short pulse with a intensity modulator. Then the pulse is amplified and frequency doubled to be detectable on the streak camera. The frequency doubled pulse is then split and sent to an optical spectrum analyzer (OSA) for control and to the streak camera where the pulse with the beating modulation is detected. A detailed discussion of the setup follows.

Tunable lasers and intensity modulation

The two tunable cw lasers each have an adjustable center frequency. The maximum difference center frequency is $450GHz$ and the minimum difference frequency is $50GHz$. The center frequency can be adjusted in $25GHz$ steps for each laser and the linewidth of each laser is $< 1GHz$. The output power of each laser is $1mW \leftrightarrow 0dBm$. Both lasers are combined into a single polarization maintaining fiber (Thorlabs). The combiner is from Thorlabs with an input loss of $\sim 3dB$. A Mach-Zehnder modulator (3dB transmission level $> 10GHz$) and a DG645 Pulse generator are used to create $\sim 1.5ns$ long light pulses. The length of the light pulses is chosen to be the same as the 4σ length of

the AWAKE proton bunch. The intensity modulation does not introduce a linewidth broadening as the bandwidth limited linewidth is still less than 1GHz. The repetition rate of the pulse generator and thus of the modulated light pulse is $f_{rep} = 100kHz$.

Amplification, frequency doubling and OSA

The pulse is then sent by polarization maintaining fibers into an amplifier (EDFA-CW-PMC0-PR-20-40-FCA from Acal-BFI with up to 40dB gain and 20dBm maximum output power) where the average output power can be adjusted between $10mW$ and $100mW$. The polarization of the modulated pulse can be controlled by a bat-ear fiber polarization controller (3 coils, Thorlabs) and is then sent into a periodically poled Lithium Niobate (PPLN) crystal (1mm long, MSHG1550-0.5-1 Covesion Ltd.) whose temperature is controlled in a small oven (also Covesion Ltd.). The laser pulse is sent into the PPLN crystal by using a fiber collimator (Thorlabs) and a $f = 100mm$ lens ($25.4mm$ diameter). The fiber collimator is mounted on a X-Y positioner stage on an optical rail (Thorlabs). The lens is mounted on the optical rail. The crystal with the oven is also placed on the optical rail with a special mount that allows it to move in one direction perpendicular to the optical rail. This is needed because the PPLN crystal has different periods for different wavelength bands and the band of interest ($1553nm \pm 1nm$) would be outside of the X-Y positioner range of the fiber collimator. Behind the crystal there is another $f = 100mm$ lens ($25.4mm$ diameter) and a X-Y positioning stage with another collimator to capture the light into a multimode fiber. The multimode fiber has a core diameter of $200\mu m$ (Thorlabs). The chromatic dispersion in the multimode fiber can be ignored as the total fiber length is $\sim 1m$ but the modal dispersion needs to be considered. The maximum dispersion can be estimated by calculating the path length of a ray that enters the fiber at the maximum acceptance angle, which is given by the numerical aperture $NA = n_{air} \cdot sin(\theta_{acc})$ and compared to a ray that enters the fiber with $\theta = 0°$. The path length distance d is given by $d = \frac{l_{fiber}}{\sqrt{1-NA^2/n_{core}^2}}$ where l_{fiber} is the length of the fiber and n_{core} is the refractive index of the core. For a typical value of $n_{core} \sim 1.445$ at the wavelength of interest, a $200\mu m, NA = 0.22$ fiber with a length of $1000mm$ gives a maximum path length difference of $11.8mm$. This is far more than the wavelength of the intensity modulation (free space wavelength of $\sim 1.26mm$) and care must be taken that the modal dispersion does not destroy the modulation. The second $f = 100mm$ lens and the fiber collimator are used to launch the laser light into the fiber with the same conditions as it was launched from the single mode fiber into the PPLN. This proved to be successful as the streak camera was able to see almost 100% modulated light pulses. The laser electric field E entering the PPLN is of the form

$$E \sim A_0 \cos(\omega_1 t + \delta_1) + B_0 \cos(\omega_2 t + \delta_2) \tag{4.1}$$

where $A_0, \omega_1/(2\pi), \delta_1$ are the amplitude, frequency and phase of laser 1 and $B_0, \omega_2/(2\pi), \delta_2$ are amplitude, frequency and phase of laser 2. The long envelope is neglected here. The PPLN crystal frequency doubles the incoming laser light with an efficiency that is pro-

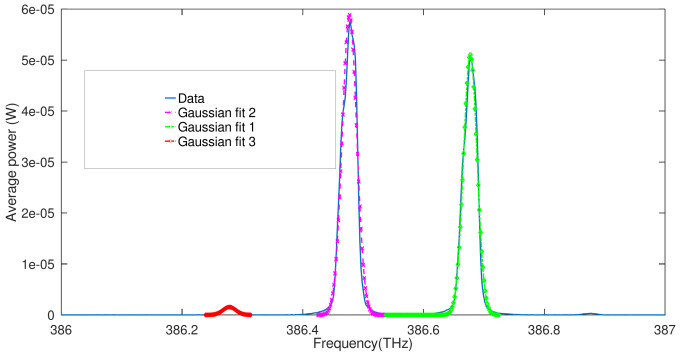

Figure 4.2: OSA spectrum for a $f_1 - f_2 = 200GHz$. For all three peaks a Gaussian of the form $K_i e^{-(f-f_i)^2/(2\sigma_i)^2}$ has been fitted. In This case the fit parameters that are needed for modulation depth calculations are $K_1 = 5.886 \cdot 10^{-5}, K_2 = 5.108 \cdot 10^{-5}, K_3 = 1.545 \cdot 10^{-6}$ and $f_1 = 386.48THz, f_2 = 386.68THz, f_3 = 386.28THz$. The width σ of the Gaussians is (in nm): $0.024174, 0.022566$ and 0.021646

portional to $|E|^2$[59]. The outgoing electric field E_{out} is then given by

$$E_{out} = A\cos(2\omega_1 t + 2\delta_1) + B\cos(2\omega_2 t + 2\delta_2) + C\cos((\omega_1 + \omega_2)t + \delta_1 + \delta_2) \quad (4.2)$$

where A, B, C are factors that depend on the conversion efficiency and the phase matching of the fundamental wave with the frequency doubled wave. The phase matching is adjusted by changing the temperature of the crystal. A $50:50$ splitter sends half of the light to an optical spectrum analyzer (OSA) that has a fiber input. The other half is sent to the streak camera. On the OSA the three conversion factors A, B, C can be measured (both fibers have the exact same length) and the modulation depth can be determined. A typical OSA spectrum is shown in fig.4.2. Each OSA spectrum peak is fitted to a Gaussian of the form $K_i e^{-(f-f_i)^2/(2\sigma_i)^2}$. From this fit the factors A, B, C from eq.4.2 can be calculated by $A = K_1^2/2$, $B = K_2^2/2$ and $C = K_3^2/2$. For all fitted spectra the width of the Gaussian fits was always comparable and within 10% variation, typical values are given in the description of fig.4.2.

Signal on the streak camera

The $50:50$ splitter sends half of the frequency doubled light towards the streak camera. The imaging system towards the streak camera will be discussed later. The photocathode

is only sensitive to $|E_{out}|^2$[60] and thus the signal on the streak camera is given by

$$|E_{out}|^2 = \frac{A^2}{2} + \frac{A^2}{2}\cos\left(4\omega_1 t + 4\delta_1\right) + \frac{B^2}{2} + \frac{B^2}{2}\cos\left(4\omega_2 t + 4\delta_2\right) \times$$
$$+\frac{C^2}{2} + \frac{C^2}{2}\cos\left(2(\omega_1+\omega_2)t + 2\delta_1 + 2\delta_2\right) + AB\cos(4(\omega_1+\omega_2)t + 4\delta_1 + 4\delta_2) \times$$
$$+AB\cos(2(\omega_1-\omega_2)t + 2(\delta_1-\delta_2)) + AC\cos((\omega_1-\omega_2)t + (\delta_1-\delta_2)) \times$$
$$+BC\cos((\omega_1-\omega_2)t + (\delta_1-\delta_2)) \quad (4.3)$$

where the terms with $4\omega_{1/2}$ and $2\omega_{1/2}$ can be neglected as they oscillate too fast to be detectable. The remaining terms are then given as

$$|E_{out}|^2 = AB\cos(2(\omega_1-\omega_2)t) + 2(\delta_1-\delta_2)) + AC\cos((\omega_1-\omega_2)t) + (\delta_1-\delta_2)) \times$$
$$+BC\cos((\omega_1-\omega_2)t) + (\delta_1-\delta_2)) \quad (4.4)$$

where it is now clear that there will be a signal that has a modulation with the difference frequency $\frac{\omega_1-\omega_2}{2\pi}$ but also with the doubled term $\frac{2(\omega_1-\omega_2)}{2\pi}$. To get rid of the doubled difference frequency term, the phase matching condition of the PPLN crystal has to be changed (by controlling the temperature of the crystal) to allow only the frequency doubling of two terms in eq.4.2. This must always be the term with $\omega_1+\omega_2$ (with amplitude C) and exclusively either $2\omega_1$ (amplitude A) or $2\omega_2$ (amplitude B). So either A or B can be considered as 0. This can be checked in real time with the OSA as seen in fig.4.2. With this condition fulfilled the detected signal $S(t)$ on the streak camera is of the form

$$S(t) = (S_0\cos((\omega_1-\omega_2)t + \varphi) + C_0)\cdot e^{-t^2/(2\sigma_t)} \quad (4.5)$$

which is a signal that has a modulation frequency of $\frac{\omega_1-\omega_2}{2\pi}$. The Term S_0 can be calculated from eq.4.4 and the measured OSA spectrum fig.4.2 as $S_0 = \sqrt{K_1\cdot K_2}$ and $C_0 = \sqrt{K_1^2+K_2^2}$. The modulation depth is then calculated as S_0/C_0. Because the fitted Gaussian width is $\sim$ *const.*, it does not play into the modulation depth. The signal measured by the camera for the $200GHz$ modulation frequency shown in fig.4.2 is shown in fig.4.3. The calculated modulation depth from the OSA is $> 90\%$. In fig.4.4 the typical modulation depth calculated from the OSA fit is shown for various beating frequencies that were imposed onto the laser pulse. The modulation depth of the incoming laser pulse was always above 95.5% and thus no additional signal degradation is introduced.

Imaging of fiber and energy into streak camera

After the 50 : 50 beamsplitter the final imaging optics to the streak camera from the fiber was done by mounting the fiber on a X-Y translator that is put in a optical cage system. The optical cage has two $f = 50mm$ ($25.4mm$ diameter) lenses that act as 1 : 1 imaging system to image the fiber core onto the streak camera slit. The distance between the first lens and the fiber end is $f = 50mm$ and again the distance from the second lens to the streak camera slit is $f = 50mm$. The cage allows to adjust the system and the X-Y

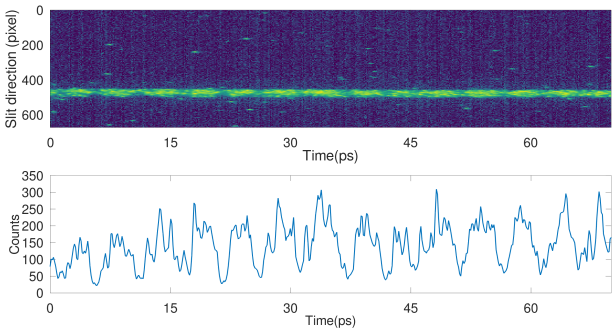

Figure 4.3: Top: Time-resolved image of the frequency beating on the streak camera. The modulated laser pulse is the bright stripe across the image.
Bottom: A profile of the image created by summing along the slit pixels from 400 to 500. The modulation is still visible by eye but the experiment shows that the visible modulation degrades very fast for modulation frequencies $> 200GHz$. In this case the imposed frequency was $200GHz$.

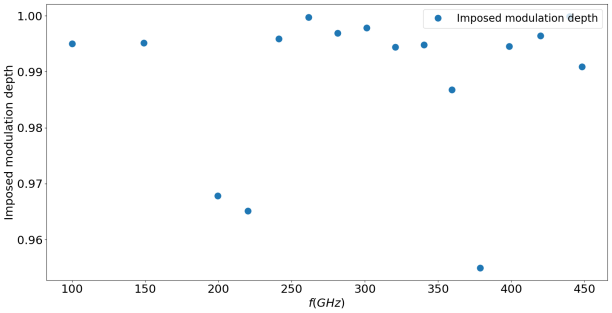

Figure 4.4: Typical modulation depth calculated from OSA fits for different imposed frequencies. The modulation depth is very close to 100% for all imposed frequencies.

stage allows to move the spot on the streak camera. Both cylindrical and spherical lenses have been used as the final focussing lens. The cylindrical lens disperses the light along the slit and thus lowers space charge effects. The energy onto the streak camera can be estimated by integrating the spectrum on the OSA (see fig.4.2) and an estimation from the imaging system. The fiber has a $NA = 0.22$ and the optical system has a $NA = 0.254$ which means that all of the light from the fiber is captured and imaged. The only loss occurs because of the slit that cuts the amount of light that reaches the photocathode. The energy per pulse can be estimated from the OSA ($E_{pulse} = P_{avg}/f_{rep}$) and from the slit with together with the fiber diameter. As an example the energy in the pulse shown in fig.4.2 and fig.4.3 is $32pJ$ which is a typical value for the settings used. The slit width is $50\mu m$ thus about $\sim 1/4$ of the light that is imaged can enter the slit. The available amount of light for the streak camera is $\sim 8pJ$. The energy in the pulses ranged between $10pJ$ and $100pJ$ before accounting the slit. This energy has to be compared with the energy of the OTR pulse that is created by the AWAKE proton bunch. The AWAKE proton bunch ($N_p \sim 1 - 3 \cdot 10^{11}, \gamma \sim 400$) emits in the band λ_1 to $\lambda_2 (< \lambda_1)$ the power

$$P \approx \frac{hN_p}{\alpha\pi^2} \left[\ln(\gamma) + \ln(2) - 0.5\right] \cdot \left(\frac{c}{\lambda_2} - \frac{c}{\lambda_1}\right) \tag{4.6}$$

where c is the speed of light, h is Planck's constant and $\alpha \sim 1/137$ is the fine structure constant. This results in $\sim 22 - 60$pJ of light created for a bandwidth of 50nm from $425nm$ to $475nm$. Because the streak camera photocathode is far more efficient at $450nm$ ($\sim 40\%$) than at $776nm$ ($\sim 15\%$) and because the slit will act in both experiments as a limiting element the experiment is comparable to the AWAKE settings from the point of energy per pulse. Experience with different settings and cameras showed that the amount of light per pulse was always enough to see a valid signal, even for low powers ($\leq 20pJ$). This increases the confidence that the OTR in AWAKE will provide enough photons for the signal to be detectable.

4.1.2 Experimental Series

The two important parameters that determine the streak camera time resolution are the amount of electrons in the streak tube (thus the ingoing light intensity) and the slit width of the streak camera. A larger slit means that the time resolution will drop though a large slit width may be necessary due to the fainting of the OTR signal. Typically the time resolution does not increase for slit width's smaller than $\sim 30\mu m$ due to the point spread function of the input optics. Experimental series were made with a streak camera and following setups:

- a cylindrical lens with a spot size of $\sim 2mm$ along the slit and a slit width of $30\mu m$ was used
- a cylindrical lens and slit width of $50\mu m$ (spot size $\sim 2mm$ along the slit)
- a spherical lens with a spot size of $50\mu m$ and a slit width of $50\mu m$.

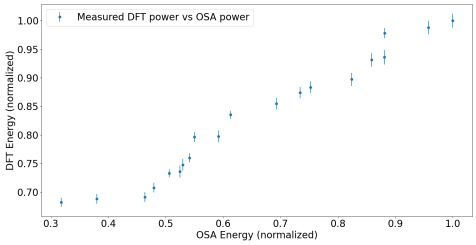

Figure 4.5: Mean energy measured in the high frequency DFT bins vs energy measured by the OSA for all imposed frequencies. The bars depict the square root of the estimated variance of the mean divided by the number of measurements. The Pearson correlation coefficient is 98.3%.

The imposed frequencies ranged from $100GHz$ to $450GHz$. For each series and modulation frequency 25 images per frequency were acquired. A line profile of each image was made, normalized to the power spectrum and then a DFT (see next section) of the normalized profile was applied with an empty background profile subtracted. The resulting profile had its mean subtracted. As the absolute value of the DFT, $|F_k|$, is also a measure of how much power is in the signal, the signals are also normalized to the noise power

$$PN = \sum_{n_0}^{N_0} |F_k| \tag{4.7}$$

The sum starts from n_0 corresponding to $1THz$ and ends at N_0 corresponding to $2THz$. This range is chosen because there is no signal in this range expected. In fig.4.5 the measured energy in the DFT bins versus the measured energy in the OSA for one measurement series ($30\mu m$ slit, cylindrical lens)is shown. The correlation between the measured energy in the DFT bins and the OSA is 98.3%. This shows that the DFT bins at high frequencies can be used to determine the relative energy in the streak image.

4.2 DFT and Measuring a DFT signal

The aim of this thesis is to detect the micro-bunches that are a result of the self-modulation. They appear in the streak image profiles as a modulation on the OTR intensity at the plasma frequency. The way this modulation is detected is by using the Discrete Fourier Transform (DFT). The DFT will now be introduced as a transformation acting on a discrete sampled periodic signal. Assume a time continuous real signal $S(t)$ (that is the profile made from the streak image) that is ideally sampled at points $n\Delta T$ for all times. The resulting sampled signal S_s is a discrete function extending from $-\infty$ to $+\infty$. It can be formally seen as the multiplication of an infinite train of δ-distributions

with the time continuous signal S.

$$S_s(t_n) = S(t) \cdot \sum_{n=-\infty}^{\infty} \delta(t - n\Delta T) \tag{4.8}$$

The spectrum $F(f)$ of such a sampled function is given by the convolution theorem. It is the convolution of the δ-train and the Fourier transform $FT(\omega)$ of the signal.

$$F(f) = \frac{1}{\Delta T} \sum_n FT(\omega - \frac{n}{N\Delta T}) = \sum_n S(n\Delta T) \exp(-i\omega n\Delta T) \tag{4.9}$$

This is now a periodic summation of the original spectrum, the discrete time Fourier transform (DTFT) of S which is a continuous spectrum. When the highest frequency in the sampled signal is lower than the Nyquist frequency of the sampling rate, then no errors are introduced by this periodic summation. In (finite time) experiments one cannot sample the signal for all times, so the sampled $S_n = S(t_n), n = [0, 1, ..., N - 1], t_n = n\Delta T$ is known between 0 and $(N-1)\Delta T$ for the total time $N\Delta T$. This can be modeled by multiplying the underlying signal S with a window function W that becomes zero for $t \leq 0$ and $t \geq N\Delta T$. To introduce the DFT one can now make a periodic summation of the windowed signal with period T_p, where $T_p = M\Delta T \geq N\Delta T$. The periodic summation can be modeled as the convolution of the sampled and windowed signal with $\sum_n \delta(t - nT_p)$. The Fourier transform $F(f)$ of the periodic summation is again calculated with the convolution theorem as

$$F(\omega) = \frac{1}{T_p} \left(\sum_n W(n\Delta T) S(n\Delta T) \exp(-\omega n\Delta T) \right) \cdot \sum_{k=-\infty}^{\infty} \delta(\omega - \frac{2\pi k}{T_p}) \tag{4.10}$$

since it is assumed that the window function is zero for $n \leq 0$ and $n \geq N$. The sum over n can be limited from 0 to $N - 1$. Replacing ω with its discrete value $\omega_l = \frac{2\pi l}{T_p}$ and setting $M = N$ results in the DFT $F_k = F_k\{W_n S_n\}$ that is periodic with $F_{k+M} = F_k$. A usual window function is the rectangular window, that is 1 when $0 \leq n \leq N - 1$ and zero elsewhere.

$$F\{S_n\}(\omega_k) = F\{S_n\} = F_k = \frac{1}{N} \sum S(t_n) \exp(-2\pi i f \Delta T k). \tag{4.11}$$

The DFT is a complex function of $\omega_k = \frac{2\pi k}{N\Delta T}$. Note that the length of the window $N\Delta T$ determines the frequency bin difference $1/\Delta T$. A change in the time window changes all frequencies up or down. The DFT in eq.4.11 can be inverted to regain the sampled signal S_n by the formula eq.4.12.

$$S(t_n) = \sum_{k=0}^{N-1} F_k \exp(i \frac{2\pi k}{N\Delta T} t_n) = \sum_{k=0}^{N-1} F_k \exp(i\omega_k t_n) \tag{4.12}$$

So in summary the interpretation of the DFT that is used in this thesis is the following:

- An infinite continuous signal $S(t)$ is sampled at discrete time points t_n
- The (continuous) spectrum of this sampled function is now a periodic summation of the original spectrum
- A measurement does not sample for all times but only for a certain time window $N\Delta T$
- The discrete spectrum of this finite sampled signal is the DFT which samples the continuous spectrum of the periodically summed spectrum.

4.2.1 Zero Padding

The interpretation of the DFT as sampling an underlying continuous periodic summed spectrum allows the possibility to interpolate spectral peaks. In the derivation of eq.4.11 a periodic summation with some period T_p is introduced. Since the window function is zero for $n < 0$, one can assume $M = LN$, which corresponds to adding zeros to the known signal. The resulting DFT is

$$\frac{1}{LN}\sum_{n=0}^{N-1} W(t_n)S(t_n)\exp(-i\frac{2\pi k}{M\Delta T}n\Delta T) \tag{4.13}$$

with $\omega_k = \frac{2\pi k}{M}$ and k ranging from zero to M. When $M \to \infty$ we get a continuous ω_k and the resulting DFT is the DTFT of the windowed signal (scaled by L). The DTFT in turn is a very good approximation of the Fourier transform. Zero padding does not increase the resolution of the DFT but is a consistent way of interpolating a signal that is leaking into other frequency bins. Infinite zero padding does recover the "true" frequency of a sinusoidal signal when the frequency of the sinus lies between two frequency bins. In fig.4.2.1 an example DFT power spectrum from the series with the $50\mu m$ spot size is shown where zero padding used as an interpolation method to determine the measured frequency. The DFT bins for the images of the streak camera are $f_{bin} = 508/70ps \sim 14.3GHz$ apart and the imposed frequency of $281.2GHz = 19.66 \cdot f_{bin}$ is a non integer multiple of the bin spacing frequency. In this case the DFT samples the underlying DTFT at very inconvenient points and the peak frequency is not sampled [61]. Zeropadding interpolates the underlying DTFT with a higher precision and measures a frequency very close (highest peak is now at a bin corresponding to $280.5GHz$) to the imposed one.

4.2.2 The distribution of a Signal

The DFT is useful to detect this frequency and especially the absolute value $|F_k|$ shows the amplitude of a sinusoidal frequency in the signal. In many cases peaks can very easily be distinguished from noise in the DFT, but for very low signal amplitudes with noise it is no longer clear what is a signal peak in the DFT and what is a noise peak. It will be shown that $|F_k|$ is distributed according to a Rayleigh distribution when

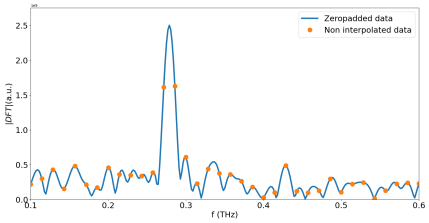

Figure 4.6: Example DFT power spectrum that shows the effect of zeropadding (from the series with a $50\mu m$ spotsize). The Imposed frequency is $281.2GHz$ which lies between the DFT bins $271.7GHz$ and $286GHz$ (the spacing between bins is $14.3GHz$). The underlying DFT leaks into the neighboring bins. Zeropadding allows for an interpolation of the frequency which is here interpolated as $280.5GHz$, very close to the imposed frequency.

there is no deterministic signal but only noise in the sampled series. This opens a possibility to discriminate a periodic signal from noise. The measured signal is modeled as $S(t_n) = S_d + N(0, \sigma_n^2)$ where S_d is a real value deterministic signal and $N(0, \sigma_n^2)$ is some additive noise drawn from a normal distribution $\sim \frac{1}{\sqrt{2\pi\sigma_n^2}} e^{-\frac{(x-\mu)^2}{2\sigma_n^2}}$ with mean $\mu = 0$ and a time bin dependent variance σ_n^2. The DFT F_k of such a signal is now also a random variable and it is easy to see that it is a Gaussian random variable with mean $F_k\{S_d\}$. To distinguish a signal from noise one is interested in the absolute value $|F_k|$ as it is a marker for the signal strength. The distribution of $|F_k|$ is not Gaussian but can be approximated by a Rice distribution as will be shown in the following.
By definition one is looking for the distribution of

$$|F_k| = \sqrt{\mathfrak{Re}\left(\sum_{n=0}^{N-1} S(t_n)\exp(-i\frac{2\pi k}{N\Delta T}t_n)\right)^2 + \mathfrak{Im}\left(\sum_{n=0}^{N-1} S(t_n)\exp(-i\frac{2\pi k}{N\Delta T}t_n)\right)^2} \tag{4.14}$$

where $\mathfrak{Re}$ and $\mathfrak{Im}$ depict the real an imaginary parts of F_k. Expanding for example the real part one sees that it is a sum of Gaussian distributed variables with an offset

$$\mathfrak{Re}(F_k)^2 = \left(\frac{1}{N}\sum_{n=0}^{N-1}\cos\left(\frac{2\pi kn}{N}\right)S_d + \frac{1}{N}\sum_{n=0}^{N-1}\cos\left(\frac{2\pi kn}{N}\right)G(0,\sigma_n^2)\right)^2 \tag{4.15}$$

making use of the fact that the sum of Gaussian distributed variables is again Gaussian distributed $\frac{1}{N}\sum_{n=0}^{N-1}\cos\left(\frac{2\pi kn}{N}\right)G(0,\sigma_n^2) \sim G(0, \frac{1}{N^2}\sum_{n=0}^{N-1}\cos^2\left(\frac{2\pi kn}{N}\right)\sigma_n^2)$ which will be shortened as G_c and has mean of zero. The part contributed by the deterministic signal in eq.4.15 is just the real part of $F_k\{S_d\}$. This leads to

$$\mathfrak{Re}(F_k)^2 = (\mathfrak{Re}\{F_k\{S_d\}\} + G_c)^2 \tag{4.16}$$

and an analogue expression is found for the imaginary part

$$\mathfrak{Im}(F_k)^2 = (\mathfrak{Im}\{F_k\{S_d\}\} + G_s)^2 \tag{4.17}$$

where $G_s \sim G(0, \sum_{n=0}^{N-1} \sin^2\left(\frac{2\pi kn}{N}\right) \sigma_n^2)$. After shifting the Gaussian distributions from zero mean to mean $\mathfrak{Re}(F_k\{S_d\}) = \mu_1$ and $\mathfrak{Im}(F_k\{S_d\}) = \mu_2$ and one gets the result

$$|F_k| = \sqrt{G(\mu_1, \sigma_c^2)^2 + G(\mu_2, \sigma_s^2)^2} \tag{4.18}$$

where $\sigma_{s/c}^2 = \sum_{n=0}^{N-1} \cos / \sin^2\left(\frac{2\pi kn}{N}\right) \sigma_n^2$. Following now the steps of [62] one can write down the probability distribution of $x \sim G_c$ and $y \sim G_s$. This leads to

$$p(x,y) = \frac{1}{2\pi\sigma_c\sigma_s} \mathrm{e}^{-\frac{(x-\mu_1)^2}{2\sigma_c^2}} \mathrm{e}^{-\frac{(y-mu_2)^2}{2\sigma_s^2}} dxdy \tag{4.19}$$

$$= \frac{1}{\pi\sqrt{1-b^2}} \mathrm{e}^{-\frac{(X-\mu_1)^2}{1+b}} \mathrm{e}^{-\frac{(Y-\mu_2)^2}{1-b}} dXdY \tag{4.20}$$

where $S^2 = \sigma_s^2 + \sigma_c^2$ was used, $bS^2 = \sigma_s^2 - \sigma_c^2$,$b = \frac{1-\frac{\sigma_s^2}{\sigma_c^2}}{1+\frac{\sigma_s^2}{\sigma_c^2}}$ and a variable transformation $X - \mu_S = (x - \mu_1)/S$, $Y - \mu_2 = (y - \mu_2)/S$ was made [62]. This corresponds to $\sigma_s = \frac{1}{2}(1+b)S^2$ and $\sigma_c = \frac{1}{2}(1-b)S^2$. The distribution of interest is $r = \sqrt{X^2+Y^2}$ and thus after a change to radial coordinates $X = r\cos(\phi)$, $Y = r\sin(\phi)$ one has now

$$p(r,\phi) = \frac{r}{\pi\sqrt{1-b^2}} \mathrm{e}^{-\frac{(r\cos(\phi)-\mu_1)^2}{1+b}} \mathrm{e}^{-\frac{(r\sin(\phi)-\mu_2)^2}{1-b}} drd\phi \tag{4.21}$$

To get the distribution of $r = \sqrt{X^2+Y^2}$ an integration over ϕ, which goes from zero to 2π, has to be applied. Introducing $\tilde{\mu}_1 = \mu_1\sqrt{(1-b)}$ and $\tilde{\mu}_2 = \mu_2\sqrt{(1+b)}$ one can write $p(r)$ as

$$p(r) = \frac{r}{\pi\sqrt{1-b^2}} \mathrm{e}^{\frac{-1}{1-b^2}\left(\tilde{\mu}_1^2+\tilde{\mu}_2^2\right)} \times$$
$$\times \int_0^{2\pi} \exp\left(\frac{-1}{1-b^2}\{r^2\left[1-b\cos(2\phi)\right] - 2r\sqrt{\tilde{\mu}_1^2+\tilde{\mu}_2^2}\cos(\phi+\varphi_b)\}\right) d\phi \tag{4.22}$$

where $\varphi_b = \tan^{-1}\left(\frac{\tilde{\mu}_2}{\tilde{\mu}_1}\right)$. To further simplify this integral, it is useful to have a look at b or equally σ_s and σ_c. Rewriting the definition for e.g. σ_c one gets $\sigma_c^2 = \frac{1}{2N^2}\left(\sum_{n=0}^{N-1}\sigma_n^2 + \sum_{n=0}^{N-1}\cos\left(\frac{2\pi 2kn}{N}\right)\sigma_n^2\right)$ and see that this is $\frac{1}{2N}DFT\{\sigma_n^2\}(0) + \frac{1}{2N}\mathfrak{Re}\{DFT\{\sigma_n^2\}(2k)\}$. Similarly for σ_s^2 one has $\sigma_s^2 = \frac{1}{2N}DFT\{\sigma_n^2\}(0) - \frac{1}{2N}\mathfrak{Im}\{DFT\{\sigma_n^2\}(2k)\}$. Thus for given noise ratios σ_s and σ_c, b is a function of ω_k. Also $\tilde{\mu}_1$ and $\tilde{\mu}_2$ are depending on ω_k through b and through the deterministic signal S_d. For the further analysis it will be assumed that σ_s does not differ to much from σ_c for each frequency bin ω_k (when not looking at the zero frequency bin). This means for $\omega_k \neq 0$ one can assume that $b \to 0$

and simplify eq.4.22 to

$$p(r = |F_k\{S_n\}|) = \frac{r}{2\pi} \mathrm{e}^{-\left(r^2+\mu_1^2+\mu_2^2\right)} \int_0^{2\pi} \exp\left(2r\sqrt{\mu_1^2+\mu_2^2}\cos(\theta)\right) d\theta \tag{4.23}$$

$$= \frac{|F_k\{S_n\}|}{\sigma_k^2} \mathrm{e}^{-\frac{|F_k\{S_n\}|^2+|F_k\{S_d\}|^2}{2\sigma_k^2}} I_0\left(\frac{|F_k\{S_n\}| \cdot |F_k\{S_d\}|}{\sigma_k \sigma_k}\right) \tag{4.24}$$

which is known as the Rice distribution [62]. Here I_0 is the zeroth order modified Bessel function of the first kind. Note that when $b \to 0$ this means $\sigma_s \to \sigma_c = \sigma$ which can still be a function of k. Thus σ_k can vary from bin to bin (as experience tells). The condition $b \to 0$ is usually well fulfilled for most noise sources. From this one sees that for a given deterministic signal S_d with added noise each frequency bin of the DFT of the total signal, $F_k\{S_n\}$, is a random variable, which is distributed according to eq.4.24. In the absence of any deterministic signal in a frequency bin $|F_k\{S_d\}| \to 0$ the Rice distribution becomes the Rayleigh distribution

$$p(r = |F_k\{S_n\}|) = \frac{|F_k\{S_n\}|}{\sigma_k^2} \mathrm{e}^{-\frac{|F_k\{S_n\}|^2}{2\sigma_k^2}} \tag{4.25}$$

that describes the distribution of a frequency bin for a signal in time where only noise is present.
Two remarks for the derivation of eq.4.22 follow. First the assumption of Gaussian noise distribution at each time bin can be relaxed. As one can see that e.g. in eq.4.15 the resulting Gaussian is the sum of many (for the streak cameras in AWAKE >> 100) independent variables, thus even if each single noise element is not Gaussian distributed and even if they are not identically distributed, the resulting G_s and G_c will approach a Gaussian. This is true for all but special noise distributions (which will not be considered in this work and are not present in the signals considered here[1]).
Second the result can be expanded when the signal S_n is multiplied with a window function W_n. Using the convolution theorem we see that, if we follow the same steps as above, we see that we have to replace e.g. $\mathfrak{Re}\{F_k\{S_d\}\}$ with $\mathfrak{Re}\{F_k\{S_d\} * F_k\{W\}\}$ and similarly with the imaginary part. Here $*$ means the convolution operation. The noise contribution changes to $\sigma_c^2 = \frac{1}{2N}(DFT\{W_n^2\} * DFT\{\sigma_n^2\}(0)$
$+\frac{1}{2N}\mathfrak{Re}\{DFT\{\sigma_n^2\} * DFT\{W_2^2\}(2k)\})$. Thus in the limit of large N, σ_c and σ_s will still be Gaussian distributed. If $b \to 0$ the resulting distribution for each frequency bin will still be a Rice distribution 4.24. The expected signal strength will be different
$|F_k\{S_d\}| \to |F_k\{S_d\} * F_k\{W_n\}|$. The total signal $|F_k\{S_n\}|$ also has to be replaced by $|F_k\{S_n\} * F_k\{W_n\}|$. I want to stress that $|F_k\{S_n\}|$ includes the possible signal, so one has to check every bin for whether there is a signal distributed in it. Even with windowing, the absence of a signal in the Rice distribution leads to the Rayleigh distribution eq.4.25.

[1]The ADC of the streak camera is has a finite range and thus the measured variance is always finite

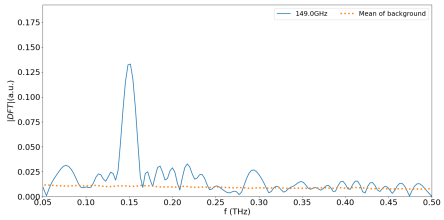

Figure 4.7: The measured mean noise background (orange dotted line) with a measured $150GHz$ signal on top (blue solid line). The image is taken from the series with a $50\mu m$ spotsize. All images have their mean subtracted thus the DFT is exactly zero at frequency 0 (not visible as the spectrum starts at $50GHz$). The signal and the background noise are zero padded. Visible is that the signal decays to the noise level when the frequency is $> 60GHz$ away from the signal or its double frequency.

4.2.3 Determining the noise in the experimental series

The spectral noise distribution for each series is measured by an interpolation. When a frequency of f_{in} is imposed, only a signal at f_{in} is expected. Possibly a signal at $2 \cdot f_{in}$ (one peak in fig.4.2 is suppressed but not exactly zero)) can also appear. The background noise spectrum for each DFT bin is constructed by using the DFT bins of all frequencies that are $> 60GHz$ away from the bin under consideration. Frequencies that are close to half the bin frequency under consideration are also excluded. This leads to the shot noise background. This resulting background is shown in fig.4.7 where an example measured signal is plotted together with the background that is created in the described way. The signal vanishes and becomes indistinguishable from noise for frequencies $> 60GHz$ away from the expected peak.

Because of the many background events it is possible to fit the theoretical Rayleigh distribution to the background distribution. In fig4.8 the histogram (normalized as a probability density) and the fitted Rayleigh distributions from eq.4.25 for the background frequencies $8 \cdot 14.3GHz = 114.4GHz$, $12 \cdot 14.3GHz = 171.6GHz$ and $20 \cdot 14.3GHz = 280.6GHz$ are shown. The background is very well described by the Rayleigh distribution. This is valid for all frequency bins and all measurement series.

4.3 Frequency detection on a streak camera image

For each of the three series (see sec.4.1.2) the background was determined and each bin was fitted to a Rayleigh distribution. To discriminate noise from a signal the probability to a threshold T is set for each bin with $P_{rayleigh}(|X| > T) < p$ to distinguish a signal from noise. The global probability to have at least one $|X|$ above this threshold between 0 and $1THz$ (70 bins) is then $1 - (1 - p)^{70}$. To have a extremely high confidence level it was decided to use a false detection rate (no signal present, but at least one bin above

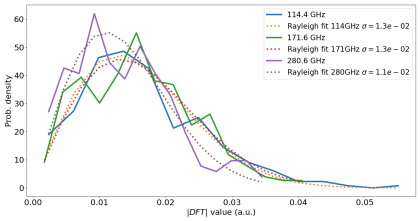

Figure 4.8: The distribution of the background noise for three frequency bins. Note that the σ of the Rayleigh distribution is dependent on the rescaling of the DFT. Note that The curve for $280.6GHz$ is used to discriminate the peak close to $300GHz$ in fig.4.7 from noise and by comparing the values one sees that the peak has a $|DFT|$ value of ~ 0.03 which is not in the $> 99\%$ percentile of the fitted noise distribution. Thus the peak would not be classified as a detected peak (see sec.4.3).

threshold) of $1\%(p = 1.44 \cdot 10^{-4})$ to reliably detect the modulation. The signal detected is the highest peak above the threshold.

Frequency detection with spherical lens and $50\mu m$ slit

In fig. 4.9 a) the mean DFT over all profiles taken for each imposed frequency together with the discrimination line is shown. It is noticeable that already the mean of the imposed frequencies above $375GHz$ is very close to the detection line. The mean is slightly above the detection threshold for frequencies that do not leak into the neighboring bins. This translates into a decreased detection probability that can be seen in b). The detection probability goes as low as $\sim 30\%$ for $450GHz$ but no false detection occurs. In AWAKE the highest expected frequency is $\sim 300GHz$. This result shows that even with a $50\mu m$ slit and a focused image one expects too see the modulation in a single event. In c) the mean zero padded DFT is shown. It shows that the loss of detection probability is due to the leakage in the neighboring bins as loss in the interpolated signal is not very strong.

Frequency detection with cylindrical lens and $30\mu m$ slit

In fig. 4.10 again the mean DFT together with the detection threshold is for imposed frequencies up to $400GHz$ shown. The mean signal is always above the detection threshold and the detection rate for the imposed frequencies is 100% except for for the highest imposed frequency (b). No false frequencies are detected. From comparing the interpolated mean DFT response c) with the non interpolated a) one can see that the $400GHz$ events have the same probability of detection as at $350GHz$. Note that the latter frequency does leak into the neighboring bins.

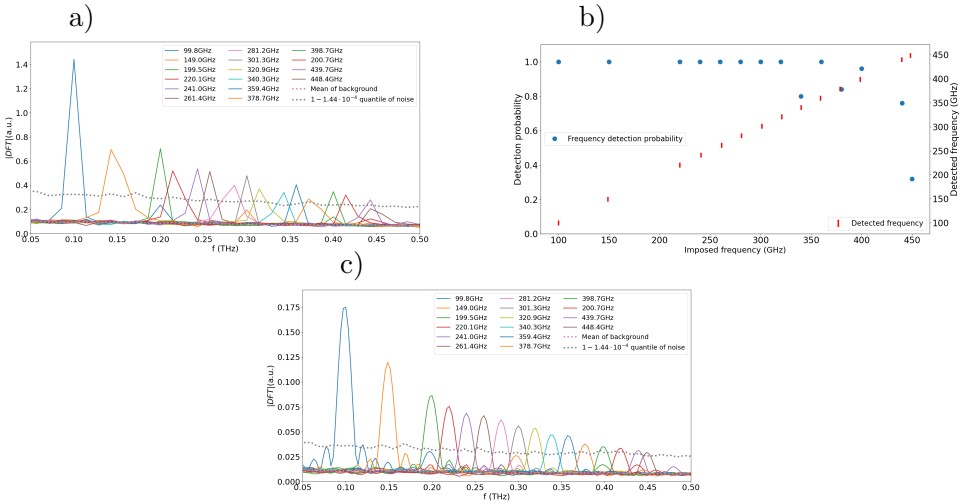

Figure 4.9: a) Non zero padded mean DFT for all measured signals. The noise-peak discrimination line is shown as the dashed line. It is clearly noticeable that the mean DFT values above $375GHz$ are only slightly above (or even below) the discrimination line. Especially for $450GHz$ this is because the imposed frequency lies between two DFT bins and the signal leaks into the neighboring bins. b) This leads to a decreased detection probability for frequencies above 325 GHz. All detected frequencies lie after zeropadding close ($< 5GHz$) to the imposed frequency. No false detection occurs. c) Interpolating the measured mean signal by zeropadding shows that the response of the streak camera does not decrease very strongly for frequencies above $350GHz$ but the leaking into neighboring bins leads to the loss of detection probability.

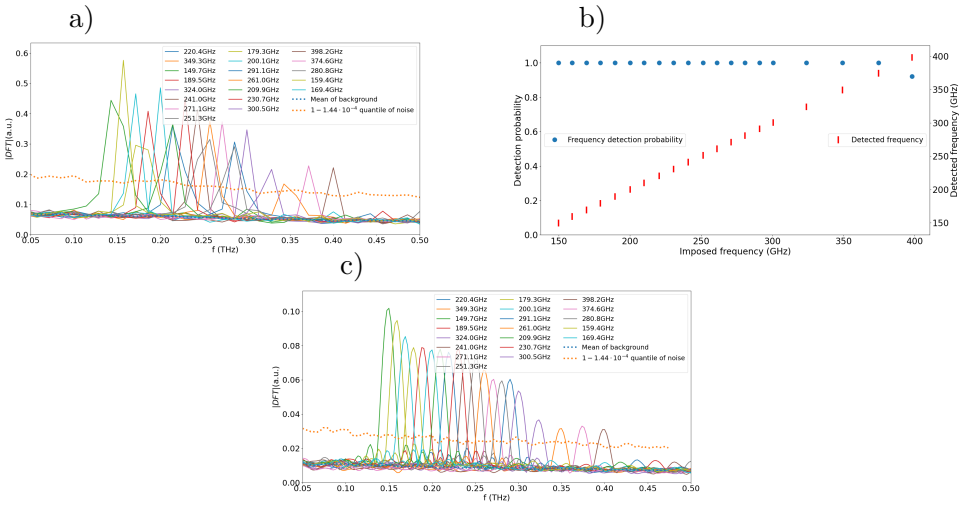

Figure 4.10: a) Non zero padded DFT mean values. b) Detection probability for each frequency. No false frequencies are detected. c) Interpolated harmonic response of the streak camera.

Frequency detection with cylindrical lens and $50\mu m$ slit

With a larger slit more light can enter the streak camera. More light would increase the signal to noise ratio of the detected signal but also increases the space charge effect in the streak tube. As shown in fig.4.11 a), with more light entering the streak camera the mean DFT is always well above the detection threshold. In b) the detection rate for all frequencies is shown to be 100% for frequencies up to $450GHz$ and no false detection occurs. In c) again the harmonic response of the streak camera is shown and again there is a noticeable drop for frequencies above $300GHz$ but then the response stays constant.

4.4 Conclusion for AWAKE

An experiment has been built that creates a light pulse with the same temporal structure as the OTR light in AWAKE. It has been shown that the signal distribution of the DFT is given by a Rice distribution and the noise can be modeled by a Rayleigh distribution. It has been shown that a streak camera can be used in the AWAKE experiment. The streak camera is able to detect frequencies $> 350GHz$ in a single event with pulse energies that are comparable or less than what is expected from OTR light pulse. The energy in each light pulse is comparable to the energy in the OTR pulse. This places the requirement on the optical system that it must not be too inefficient. When the amount of OTR light that can be coupled into the streak camera turns out to be not sufficient for single event measurements, the DFT approach can be used to average over spectra of many events. The information about the phase of the modulation might be lost but the first and foremost goal of this work is to detect the frequency. The next chapter will discuss

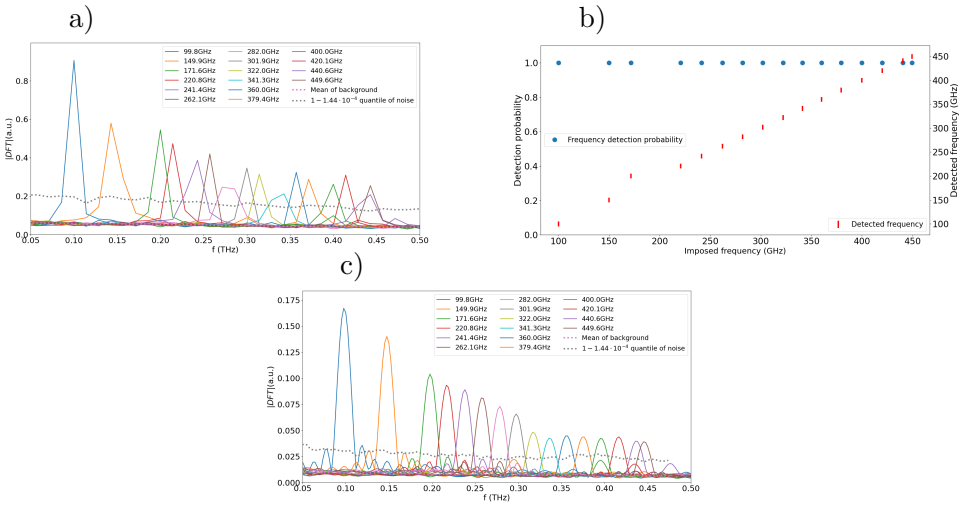

Figure 4.11: a) Non interpolated raw DFT mean values. b) Detection probability for each frequency. No false frequencies are detected. The wrong detected frequency at $180GHZ$ is correctly detected at $200GHz$ but the wrong data for the OSA was saved. The higher amount of light that is entering the streak camera ensures single event detection up to $450GHz$. c) Interpolated harmonic response of the streak camera.

the optical transport system from the beamline to the streak camera.

5 The streak camera system in AWAKE

In chapter 3 the diagnostics idea of using an OTR image of the beam was presented. In chapter 4 it was shown that streak cameras are suitable as detectors for the signal that is expected in AWAKE. Streak cameras are no radiation hard devices and therefore the camera must be placed away from the beamline. This means that an optical system needs to transport the light from the OTR foil to the streak camera. This chapter introduces the designed optical system and shows the characterization of the installed system.

5.1 The physical transport line

The physical location of the streak camera is behind a concrete radiation shield in a small hut next to the access to the AWAKE diagnostics area. According to simulations and directly behind the RIF (see chapter 3), the micro-bunches of the self-modulated beam have a transverse dimension that is comparable to the size of the un-modulated bunch ($\sigma = \sigma_0 \left(1 + \frac{z^2\epsilon^2}{\sigma_0^4}\right)^{1/2} \sim 0.56mm$, for $\epsilon = 2 \cdot 10^{-6}mm - mrad$,$z = 13.5m$ and $\sigma_0 = 0.2mm$). The OTR creates light with the same time structure as the proton bunch and this light needs to be transported to the streak camera. This means that a $\sim 14m$ transport line needed to be designed and integrated into the AWAKE area. Fig.5.1 shows the AWAKE area. The proton beam arrives from the SPS and undergoes self-modulation in the plasma. After the plasma the beam travels $\sim 3.5m$ until it hits the OTR foil that is marked as OTR/CTR diagnostics. Marked with "A" is the concrete shielding and the streak camera is located in the encircled area TSG41 (called "streak hut"). The point marked with "B" is where the AWAKE laser pulse is coupled into the SPS beamline. At this position a continuous wave Helium Neon (HeNe) laser can be coupled into the beamline. This laser is used for alignment of the OTR transport line.
The OTR light is created when the beam hits an aluminum coated silicon wafer (OTR diagnostics in fig.5.1). This wafer is held with a custom (MPP-workshop) holder that is connected to a vacuum actuator. The vacuum actuator is placed on a vacuum cube that is placed in the SPS beamline. The connection to the SPS beamline is done with two bellow vacuum tube pieces. A CAD drawing of the system that is on the optical table can be seen in fig.5.2 a). The OTR setup shares its space with a complementary coherent transition radiation system (CTR) which was used together with the setup described here to study the effect of density gradients [63]. The cube is located on an optical table that is again on a concrete socket. The optical table has passive vibration suppression. The very early installation of the table with concrete block can be seen in fig.5.2 b). The OTR light is leaving the OTR cube through a sapphire vacuum window. The backside of

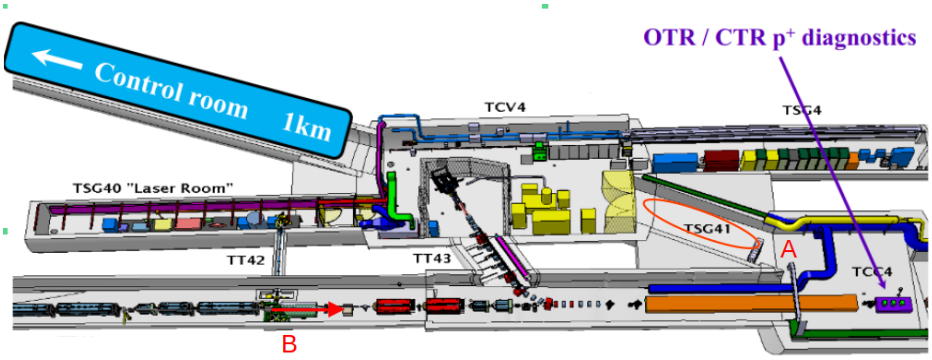

Figure 5.1: Awake area as CAD drawing. The proton bunch arrives from the left of "B" and travels (red arrow) towards the OTR diagnostics (pink arrow pointing). The Area TSG41 that houses the streak camera is circled in red (point A).

a) b)

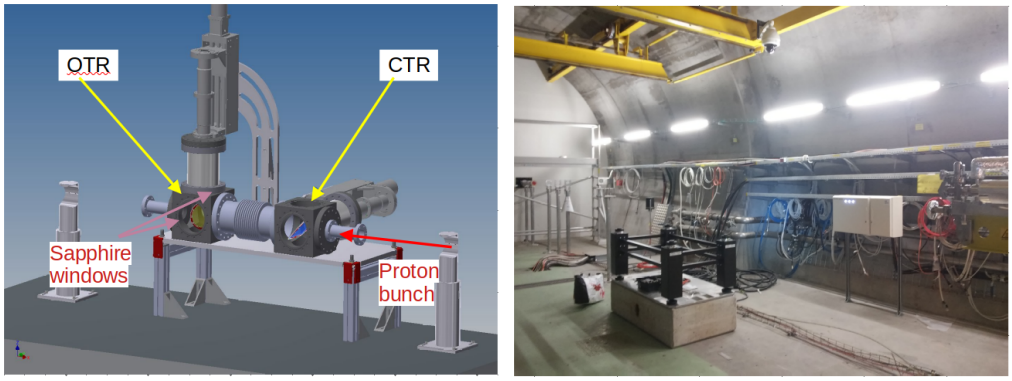

Figure 5.2: a) CAD drawing of the OTR/CTR station on the optical table. The bellow connectors to the SPS beamline are not shown. b) picture of the early integration. The concrete block for the optical table was freshly installed and the frame of the optical table had been already installed. The SPS beamline was not yet installed at the time when this picture was taken.

a) b)

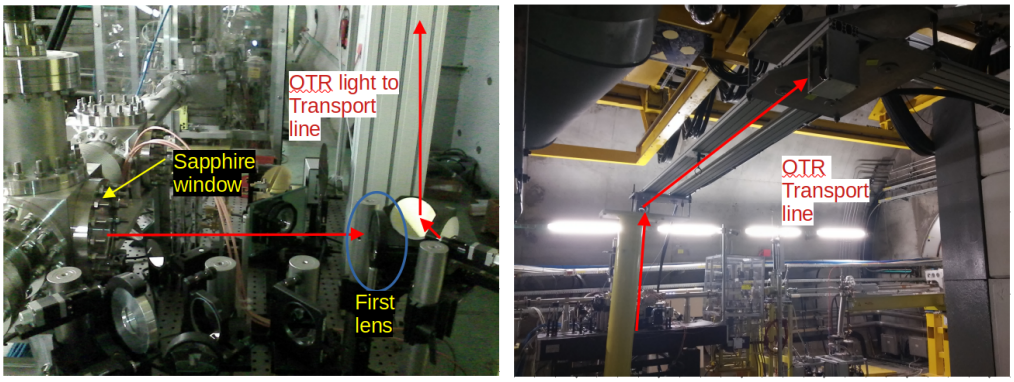

Figure 5.3: a) Optical elements on the beamline table. The OTR path is shown in red. In the foreground optical mirrors and attenuators can be seen that allow the OTR light to be sent to a CCD camera that is installed on the table. b) first part of the transport line that goes to the streak hut. The light is transported up and the line goes behind a radiation shielding (concrete blocks on the right). The deflection mirrors and one lens were already installed.

the cube has also a sapphire window which was used for alignment and calibration. Once the OTR light is coupled out, the light is going through the first lens (blue circle in fig. 5.3) and then two mirrors send the light towards the OTR transport line. The transport line is $\sim 2.5m$ above the floor level to not get in the way of the emergency exit. In fig.5.3 the first part (with lenses and mirrors installed) can be seen. The transport line makes a 90° bend after the concrete radiation shielding and then follows the exit of the area to the streak camera hut (fig.5.4). All physical installations of heavy equipment (e.g. optical table, the yellow pillar in fig.5.3, etc.) were performed by CERN integration team (lead by Ans Pardons). The support structure for the optical elements are aluminum rails that can accommodate custom made (MPP-workshop) holders for the lenses and mirrors that are needed. These holders allow to place lenses at every point along the support structures with variable height.

5.2 Theoretical considerations for the optical transfer line

The OTR emits power per solid angle $\frac{\mathrm{d}W}{\mathrm{d}\Omega} = \frac{e^2\beta^2\sin^2(\theta)}{\pi^2 c\{1-\beta^2\cos^2(\theta)\}^2}$ by the protons, which is shown in fig.5.5, and has a sharp peak at $\theta \sim 1/\gamma = 1/427$. This suggests that the numerical aperture $NA = n \cdot sin\,(\theta)$ should be $1/427$. Here n is the refractive index of the material surrounding the system (air, $n = 1.0$) and θ is the maximum angle of the rays that can enter the optical system. If one takes into account the $\sin(\theta)$ factor from $\mathrm{d}\Omega = \sin(\theta)\mathrm{d}\theta\mathrm{d}\varphi$, then the maximum of the integrand $\mathrm{d}W$ is at $\sim \frac{7}{4\gamma}$ and the integrated power does have substantial power left in larger angles. In fig.5.6 the F-number $F\sharp = \frac{f}{D}$, where f is the focal length of the input optics and D is the diameter of

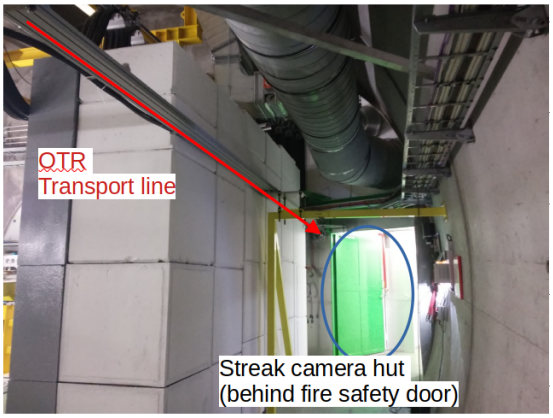

Figure 5.4: The final part of the transport line. The light is transported along the corridor towards the streak hut. At the time of this picture no lenses were installed. The streak hut has a $1mm$ thick fire proof glass window (accepted by CERN fire brigade) which is the entrance to the streak hut and ensures the fire safety. Inside the hut the optical line is deflected down to an optical table.

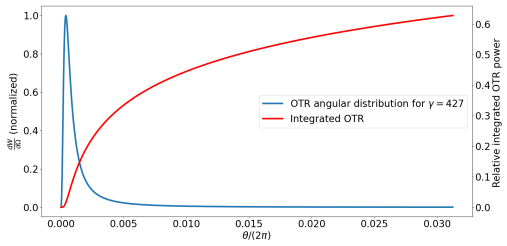

Figure 5.5: Relative angular distribution of the emitted OTR power. The emitted power peaks at an angle $1/427$. In red is the total emitted power is shown(integrated over $d\Omega$).

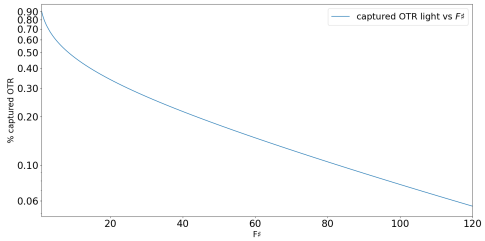

Figure 5.6: Captured percentage of OTR light versus $F\sharp$ of the optical system. The percentage is normalized to the captured light value at $F\sharp = 0$. The total amount of captured OTR light is as low as 6% at $F\sharp = 114$, which shows a $F\sharp$ as low as possible (but larger than 5) is desirable. The maximum amount of captured light ($\sim$ 33%) is given by the streak camera $F\sharp$ and the demagnification.

the input optics, is used as a measure for the collection power of a lens. This is plotted versus the total amount of OTR light captured. Because all angles in the system are $\ll 1$ and the transport line is surrounded by air the numerical aperture is approximated as $NA = \theta = \frac{1}{2F\sharp}$ and connected to the numerical aperture $F\sharp$. As the numerical aperture increases, $F\sharp$ decreases and more OTR light is captured by the optical systems due to increased collection angle, which is shown by the rise of the captured OTR light towards lower $F\sharp$ in fig.5.6. Even though the total emitted OTR power W is sharply peaked around $\sim \frac{7}{4\gamma}$ which corresponds to a $F\sharp = 144$, there is considerable amount of energy in the larger angles, which corresponds to smaller $F\sharp$. As seen in fig.5.6 only 6% are captured at $F\sharp$=114 and one needs large angles (corresponding to small $F\sharp$) to get a high capture rate. The streak camera input optics on the other end of the transport line has a $F\sharp$ of 5. This means the total $F\sharp$ of the system should be larger than 5 and smaller than 114 as one would lose light in the streak optics when $F\sharp < 5$. Another constraint is that a magnification smaller than 1 is desired. This constraint arises because the focused micro-bunches (after the self-modulation occurs) need to be imaged on the streak camera slit, which is between 30 and 50 μm in height. The quantitative LCODE simulations from chapter 3 suggest that the focused micro-bunches have a radius of $\sim 200\mu m$. This means that a $\sim 400\mu m$ object needs to be imaged onto a slit that is $50\mu m$ in height. This corresponds to a total magnification of $\sim 1/8$. The defocused protons have a much larger radius and are not captured with such a magnification. There is a trade off between magnification $|M|$ and $F\sharp$. For a well centered optical system the Smith-Helmholtz formula relates the lateral size Y of the object to the lateral size Y' of the image and to the angles light rays that a system can support [64]

$$\left|\frac{Y'}{Y}\right| = |M| = \frac{\theta_{in}}{\theta_{out}} = \frac{F\sharp_{out}}{F\sharp_{in}}. \tag{5.1}$$

Here *in* and *out* refers to the limiting and final $F\sharp$ of the system and $|M|$ is the magnification of the system. Putting these constraint together it is desirable to have $|M| \cdot F\sharp_{out} = 20 < F\sharp_{in} < 114$. A third factor is that the OTR foil is at a 45° degree to the proton beamline. This means that also points that are displaced along the optical axis need to be imaged. The longitudinal magnification $\frac{dZ'}{dZ}$ for a system that is completely in air is given by [64]

$$\frac{dZ'}{dZ} = |M|^2 \ll 1 \text{ if } |M| < 1.$$

The tilt of the foil is 45° so a light source that is $1mm$ radially displaced from the optical axis is at maximum $1mm$ displaced in Z. It will be shown that $|M| < 0.3$ and the longitudinal displacement due to the tilted foil is at maximum a few $100's$ μm. This means that the depth of view is large enough to image all particles and it will be neglected. The final $F\sharp_{in}$ is constrained by the available lens diameters. A magnification of 1/4 is easily achievable with space constraints (minimum distance of the slit to the lens is $\sim 2cm$) and commercially available lenses. This leads to a captured light efficiency of $\sim 33\%$ (corresponding to a $F\sharp_{in} = 4 \cdot 5 = 20$) which is within the range of the detection limit of a streak camera.

5.2.1 The OTR beamline

The final optical system for the streak camera with distances between the lenses and lens diameters can be seen in fig.5.7. The black lines sketch the path of the imaged light. Lenses $2-4$ are mounted on the support structure while lenses $1, 5, 6$ are on an optical table. After lens 1 there are two mirrors (tip/tilt) that couple the light into the transport line. Again after lens 4 there are two mirrors (tip/tilt) that couple the light out of the transport line. The distances between the lenses are fixed to the mentioned values except for the last distance that is variable. Lens number 6 is on a translation stage and can be used to fine tune the focus of the light on the streak slit. All lenses (except for lens 2 and 3) have been bought from Thorlabs. Lens 2 and 3 are custom-made (due to the size and large focal length) and were provided by Eksmaoptics (the Eksmaoptics lenses arrived at CERN 20 days before the first day the proton bunch was sent to the experimental area, here I want to thank Eksmaoptics for their efforts to coat the lenses in time). All lenses are anti-reflection coated for the wavelength range $400-700nm$ and have a nominal transmission of $> 95\%$. To transport the light a collection lens is used and the lenses 2,3 and 4 are used to create a $1:1$ image. Lenses 2 and 3 are necessary to increase the transmitted light for sources that are displaced radially. Lenses 5 and 6 are then used to de-magnify the object and create an image on the streak slit. The whole beamline is designed for a wavelength of 450nm and for each lens the exact focal length at 450nm has been calculated using Sellmaier formulas. The result is shown in table5.1. To calculate the magnification of the system each lens was assumed to be a thin lens with the corrected focal length. Then the thin lens equation [64]

$$\frac{1}{f_c} = \frac{1}{o} + \frac{1}{i} \tag{5.2}$$

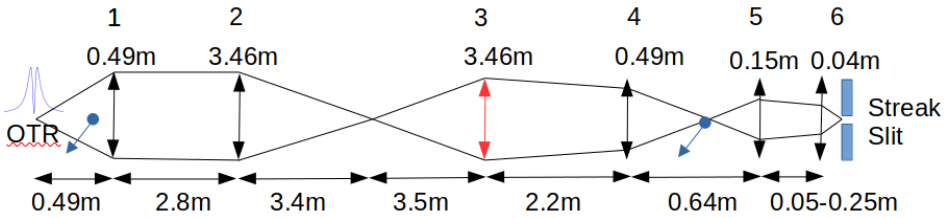

Figure 5.7: Optical beam path to the streak camera. The lenses are marked 1-6 and their nominal focal length in m is written below their number. Lens number 3 is marked red because it is the aperture stop in the current setup. The blue arrow before lens 1 and between lens 4 and 5 means that at these positions mirrors on a remote controlled translation stage can be put into the beamline to transport the light to CCD cameras. In front of the second arrow a filter-wheel is installed. For the exact calculated focal length refer to table 5.1.

was used to calculate the magnification $\frac{i}{o}$ for each lens. Here o is the distance of the object to the lens and i is the distance of the image formed. For each lens n the image position i_n was calculated and used as the object distance $o_{n+1} = d_{n-n+1} - i_n$ for the next lens. Note that if an object is in the focal plane of a lensboth the lens and the followings lens form now a thick lens. The final magnification is the product of all magnifications [64]. The calculated magnification for this setup is 0.27 for the value of $d_{5-6} = 0.19m$. For this value the setup transforms a collimated beam to a collimated beam and a image to an image. The final distance d_{5-6} has an influence on the final magnification $|M|$ of $\Delta|M| = 0.0035/cm \cdot \Delta d_{5-6}$ This was numerically estimated by varying the distance and recalculating the magnification. Since the final focusing lens is never moved more than $1cm$ from the initial position this influence is neglected. The distance d_{4-5} and the distance from the source to the first collection lens d_{1-2} have the largest influence on the magnification where the $\Delta|M| = 0.005/cm \cdot \Delta d_{4-5}$ and $\Delta|M| = 0.008/cm \cdot \Delta d_{1-2}$. Again these influences were determined by varying the corresponding distance and fixing all others. All distances but d_{5-6} were set once during setup and then not changed. The distance d_{5-6} can be changed as lens 6 is on a translation stage. An effective $F\sharp_n = \frac{1}{2\arctan\left(\frac{d_n}{o_n}\right)}$, where d_n is the diameter of the lens n, was calculated for the system. Lens number 3 sets the f-number limit with a calculated effective $F\sharp_{in}$ of 41 which is below the required 114. So $\sim$ 21% of the light that is emitted by a point source is collected. As discussed before a $F\sharp_{in}$ down to 20 could be used. To achieve such a $F\sharp$ the diameter of lens 3 needs to be 150mm. The mirrors to couple the light in and out or for the 90° bends have a size of $10.2cm$. Because they are in a 45° position with respect to the beam, they already clip some of the light and set the effective aperture stop of the system. No vendor was found that could deliver $12.7cm$ mirrors or a $150mm$ diameter lens before the first experiments.

Lens	Material	Nominal f (m)	f@450nm (m)	Diameter (mm)
1	BK7	0.5	0.493	71
2	BK7	3.5	3.456	71
3	BK7	3.5	3.456	71
4	BK7	0.5	0.493	71
5	BK7	0.15	0.147	51
6	BK7	0.04	0.039	25

Table 5.1: Table of lenses and theoretical focal length

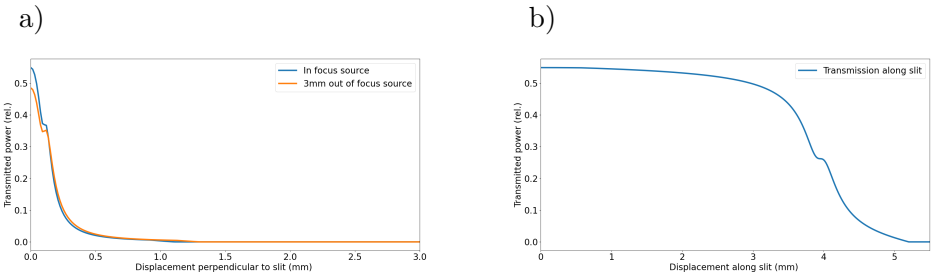

Figure 5.8: Calculated transmission of the optical beamline for an OTR source in focus (blue solid line) displaced perpendicular to the slit and one that is 3mm out of focus (orange solid line) (a). A source that is displaced laterally by 3mm has only marginally less light transmitted. In b) the transmission for an OTR source that is displaced along the streak slit direction. The transmission along the slit starts to drop considerably after $3mm$ displacement. This is far enough from the center that the micro-bunches can be imaged ($\leq 2mm$ radius).

5.2.2 Simulation of the streak signal from the self-modulated bunch

To simulate the amount of light and the signal on the streak camera a custom C++ ray tracer was written. An LCODE bunch is propagated to the position of the OTR foil. The bunch is discretized in z and r. In each z slice (slice thickness $\lambda_{pe}/10$) a fan of light rays for three wavelengths ($462.5nm, 450nm, 437.5nm$) is created at every discrete r. As all angles are small the rays are treated in a ray transfer matrix analysis. Every ray has a weighting according to the OTR power per solid angle that corresponds to its emitted angle (the sum of all weightings corresponds to the total power emitted). The optical beamline is implemented into the software using thick lens matrices. The thickness and radia of curvature for the lenses were implemented from the vendor description of the lenses. The rays propagate through the optical system and are masked by the streak camera slit ($50\mu m$ slit). The streak camera input optics has an $F\sharp$ of 5 and only rays that have an ingoing angle less than the streak camera input optics ($\theta = 1/10$) are permitted. The results for sources that are displaced perpendicular and along the streak camera

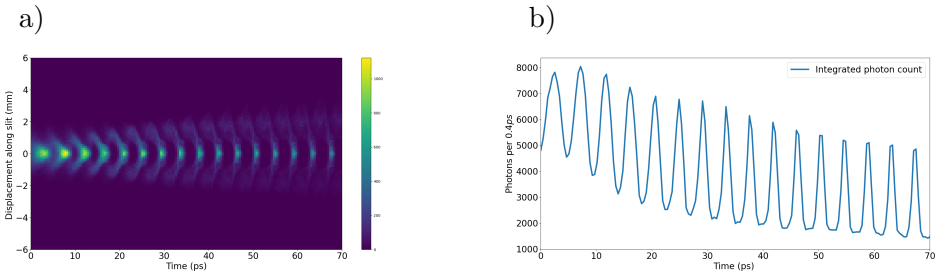

Figure 5.9: a) Simulated time-resolved image obtained through the optical transport line. The time resolution is not taken into account to leave the structure visible. The colorbar shows the number of photons per pixel and the time resolution of the grid binning is $0.2ps$. b) The profile of a) summed along the whole slit. The modulation of the micro bunches is visible and the experiment has shown that the amount of light that is transmitted is plenty.

slit are shown in fig.5.8. From this simulation and from an LCODE output a predicted streak image and time profile has been created. This was done by gridding the macro particles from LCODE and defining two axes. One that is perpendicular to the slit and one that parallel to the slit. Then the OTR transmission coefficients of fig.5.8 a) and b) were applied and a streak image is created by scaling each voxel of the beam with the number of photons created (~ 0.0016 per proton, see chapter 3) times the number of protons in the corresponding voxel. The resulting streak image and the profile is shown in fig.5.9. The AWAKE runs up to now have shown that there is plenty of light transmitted to see the micro-bunch structure. The defocused protons that can be seen in fig.5.9 a) are only visible for the first few micro-bunches but averaging over many events clearly shows the defocused bunches [65]. The ability of the streak camera setup to image the defocused protons was tremendously useful and the results were published in [65].

5.2.3 Wave optics considerations

In the preceding sections only ray optics was employed and no diffraction effects were considered. The point spread function (PSF) of a single OTR particle with gamma factor γ for light with the wavelength λ and a system with magnification M can be calculated by

$$PSF(r) \sim \left[\int_0^{\frac{1}{2F\sharp}} \frac{t^2}{t^2 + (\beta\gamma)^{-2}} \times J_1\left(\frac{2\pi r t}{\lambda M}\right) \right]^2 \tag{5.3}$$

from [66]. There were historic discussions about the spatial resolution of OTR but it has been shown that the spatial resolution of OTR is typically limited by the angular acceptance of the optical system that collects the OTR [66]. In this setup the resolution due to diffraction of the OTR in the optical system is not a limiting factor. This is shown by calculating the PSF for this setup which is shown in fig.5.10. The parameters

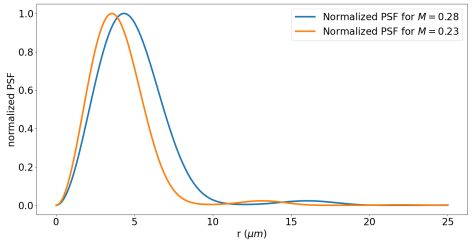

Figure 5.10: The Point spread function of a single OTR particle according to eq.5.3. The wavelength under consideration is $450nm$ and the PSF for two magnifications (0.25,blue line and 0.23, orange line) is shown. The PSF are normalized to their maximum and both do not extend further than $10\mu m$.

used are 450nm light, the SPS beam($\gamma = 427$) and the discussed setup $M = 0.28$. The PSF is confined to the area smaller than $10\mu m$ and the PSF is smaller than the slit width ($30 - 50\mu m$). This means that a single point source will spread out to a circle of $< 20\mu m$ radius and diffraction in this setup effects can be neglected. This is even more true for the measured magnification of the setup ($M = 0.23$) and thus the PSF is even more confined (orange line in fig.5.10).

5.2.4 Forward OTR from preceding CTR station

The OTR is created by a coated silicon wafer as shown in fig.5.2 a). Before the proton bunch hits the silicon wafer, it hits a metal foil that is used to create CTR. The bunch also creates forward OTR from this CTR wafer that is coupled out of the beamline by the OTR wafer. This OTR is too far out of focus to be transmitted by the optical transport line there is no hint in any experiment of detected forward OTR. The OTR signal from the screen was unaffected whether the CTR wafer was in the beam path or taken out.

5.2.5 Alignment of the OTR transport line

The alignment of the OTR transport line was done by coupling light from a transportable HeNe gas laser (Thorlabs) at position "B" of fig.5.1 into the SPS proton beamline. The light is brought to an overlap with the pulse of the AWAKE laser pulse that was aligned beforehand to the SPS proton bunch reference trajectory. This was done by sending first the AWAKE laser pulse towards the streak setup (with μJ power and another extra filter in the AWAKE laser room) and coupling the laser light to CCD cameras that were installed on the optical table in the streak hut and next to the OTR cube. Then the HeNe light was sent towards the CCD's and the position can be compared with the position of the AWAKE laser pulse. This ensured that the HeNe laser light has the same trajectory as the proton bunch and thus of the OTR. The visible HeNe light was used to center and align all optical elements in the OTR setup.

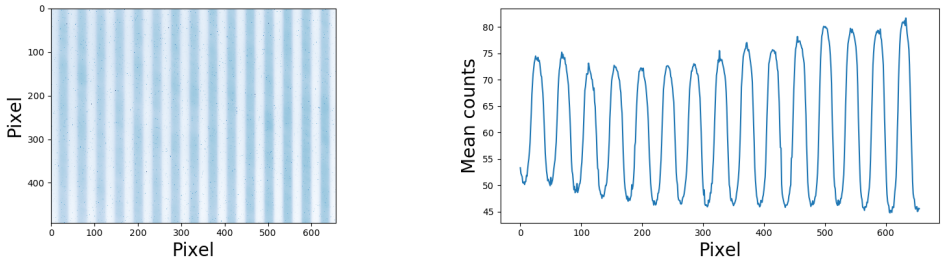

Figure 5.11: Example Image of grating taken with CCD camera. On the left hand is the original picture with 450nm filter. On the right hand side the profile along the vertical direction is taken and the modulation from the grating is visible.

5.3 Spatial calibration of the OTR setup

After installing the lenses, holders and mirrors the spatial resolution and magnification of the system were calibrated by using a 5 lines/mm grating that was illuminated by a broad band lamp and then imaged in the middle of the OTR cube from the other side of the transport line (compare with 5.2 a). The imaging was done by bringing the edge of the OTR wafer and the illuminated grating in focus at the same time. The first step was to place the grating and the lens on a rail. On the rail the magnification of the lens and grating setup is measured with a CCD and a 450nm(+-25nm) bandwidth filter. An example for this can be seen in fig.5.11 where the grating on the CCD is seen on the left and the vertical mean of the image is shown on the right. The grating can be seen as a modulation on the signal intensity. Measurements with five different magnifications $|M|$ from the 5 lines/mm grating to the CCD were done. A 122.6mm lens was used in all the measurements. The measurements had different expected magnifications $|M|$ from the grating to the CCD of 3.2 (corresponds to $d_{lg} = 160mm$ between lens and grating), 2.1 ($d_{lg} = 180mm$), 1.8 ($d_{lg} = 190mm$), 1.6 ($d_{lg} = 200mm$) and 1.4 ($d_{lg} = 210mm$). This was because the distance between lens and grating was changed by moving the grating on the rail and keeping the lens fixed. The 5 lines/mm grating frequency, scaled by the magnification $|M|$ of the lens, can be seen in fig.5.11 and the structure shows as a peak in the DFT as seen in fig.5.12. The peak position is interpolated using zero padding (see section 4.2.1) to increase the accuracy of the measured magnification. To compare the peak heights all images have been normalized to the number of counts in the image. The CCD camera pixel size S_p is known from the CCD chip width (4.8544mm) and the pixel number (656). Thus the pixel size is given by $S_p = \frac{4.8544mm}{656} = 7.4\mu m$ and one can measure the magnification. The normalization of the different measurements is again done by summing the absolute value of the high frequency terms in the DFT and dividing the signal by the resulting value. In fig.5.12 the measured magnification is shown as solid dots corresponding to the color of the measurement. The magnification $|M|$ is calculated from the interpolated frequency peak position f_{ccd} as $\left(\frac{f_{ccd}}{656 \cdot 7.4\mu m}\right) / \left(\frac{5}{mm}\right)$, the difference

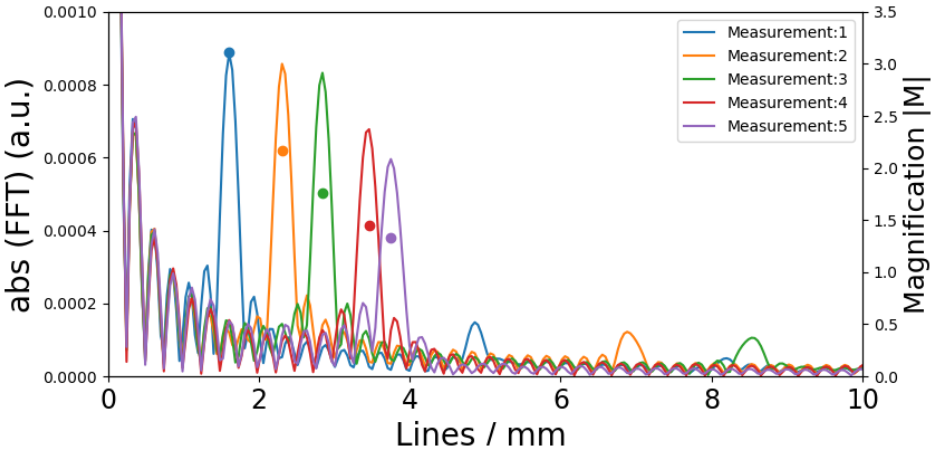

Figure 5.12: Measured lines per mm on the CCD. This is the grating frequency that is transmitted by the optical line to the streak camera. The dots are the calculated magnification from the interpolated frequency peak. The interpolation of the DFT spectrum is done using the zero padding technique in section 4.2.1.

between the theoretical and measured value is smaller than the corresponding dot size. After the magnification is measured with the CCD, the grating and lens are placed with the rail behind the OTR cube (opposite to the site where the transfer line starts). The streak camera is used in focus mode. It images the edge of the OTR foil which blocks parts of the grating image (with a 450nm(+-25nm) filter). The rail, with the lens and grating attached, is moved to a position such that the edge of the foil and the grating are in focus on the streak camera image at the same time. The foil is then completely removed and the image shown in fig.5.13 can be seen where only the grating is imaged. Again on the profile in fig.5.13 the modulation of the grating can be seen and the DFT spectrum of this profile shows a frequency peak corresponding to the number of lines/mm (the streak camera pixel number in the x axis corresponds to a imaged length) as seen in fig.5.14. Again the DFT spectrum is normalized to the high frequency components of the absolute value of the DFT spectrum. The peak f_{sc} is interpolated and the measured ratio f_{sc}/f_{ccd} gives the magnification of the whole system. The measured magnification of the system is 0.231 ± 0.01. This is smaller than expected but can be explained as the e.g. the distance d_{OTR-1} in fig.5.7 has about $1cm$ of uncertainty and the distances in the transport line also have an uncertainty of $\sim 2cm$. Already $d_{OTR-1} = 0.48m$ and $d_{4-5} = 0.61m$ lead to a theoretical magnification of 0.23 which puts the measured magnification within the possible range. The magnification measured is close to the design goal (of 0.25) thus no changes were made.
The normalized amplitude of the five measured frequencies are fitted to a Gaussian function $TF = A \cdot e^{-f^2/\sigma^2}$, which gives a measure for the spatial resolution of the system. The fit is also shown in fig.5.14 and the best fit gives $\sigma = 9.1l/mm$ which

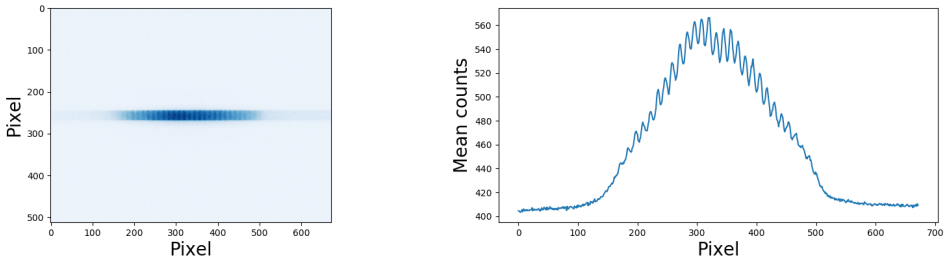

Figure 5.13: Example image of the grating taken with streak camera. On the left hand is the original picture with 450nm bandpass filter, the slit is fully opened ($200\mu m$) and the grating appears along the slit. On the right hand side a profile made by summing across the slit is shown. The modulation from the grating is visible and the DFT spectrum reveals the number of groves. In this image the CCD image magnification is 1.4, which corresponds to $7 lines/mm$ on the streak camera.

corresponds to a resolution of $0.11mm$ for spatial structures.

5.4 Limitation due to chromatic dispersion

The light from the OTR has the same time and space structure as the modulated proton bunch. The spatial structure is preserved by imaging the OTR from the foil to the streak camera. The temporal structure can be lost due to wavelength dependent dispersion in air. The broadband OTR pulse stretches as the red components of the light travel faster than the blue components. A second reason why the temporal structure can be lost is because the used lenses made out of BK7 have their own relevant wavelength dependent dispersion in the range $425 - 472nm$. The condition for imaging is that all rays sent out from a point source have the same optical path length [64]. So in imaging condition the temporal structure is not lost because there is no different path lengths of different rays from the same source for a single wavelength.
The OTR light pulses created from a single proton have a spectrum amplitude that only changes by 15% in the range from $400nm$ to $500nm$ (due to the changing index of refraction of the OTR wafer). It is considered as having a flat spectrum when emitted. This means that the emitted OTR pulse is very short and can be considered as a δ like pulse. Bandpass filters are used in the optical setup to limit the available bandwidth for the OTR light. It is assumed that the bandpass filters allow Gaussian distributed wavelengths to pass. Though this is not true. A better approximation would be a rectangular transmitted spectrum but this assumption will make the following considerations much easier for calculations. The results are still meaningful as a rectangular pulse is sinc shaped and will broaden with the same order of magnitude as a Gaussian pulse. The δ like pulse emitted from the OTR is sent through the bandpass filter which limits the bandwidth of the pulse and therefore makes the pulse of finite duration. The bandpasses

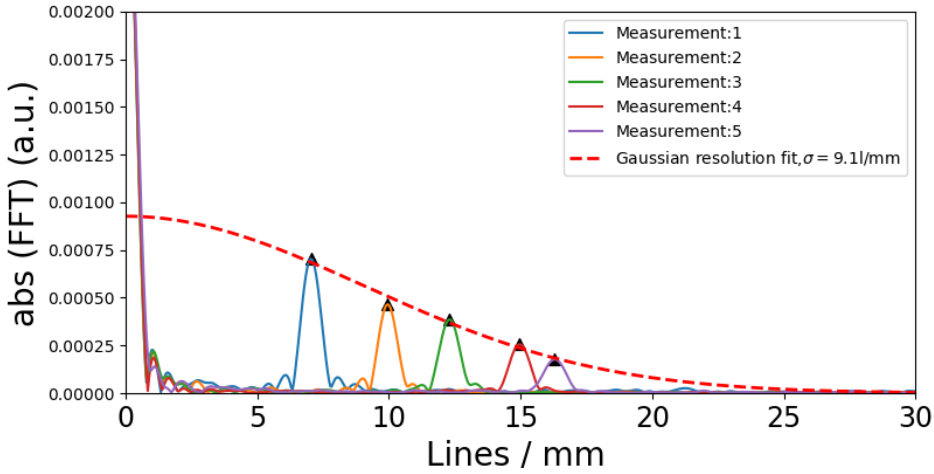

Figure 5.14: DFT spectrum of the gratings frequencies detected by the streak camera. The lines per mm are the lines on the streak camera chip. The Magnification can be calculated from the position of the peak and the amplitude of the peak is fitted to determine the modulation transfer function (see text).

are installed in a filter-wheel in the transport line (see fig.5.7). The spectrum of a single proton OTR pulse $\hat{S}_{OTR}$ is considered as now Gaussian after the bandpass.

$$\hat{S}_{OTR} = \begin{cases} \exp\left(-\left(\frac{\omega-\omega_0}{2\sigma_\omega}\right)\right) & \text{with } \omega_0 = 4186\text{THz}, \sigma_\omega = 466.5\text{THz (50nm bandpass filter)} \\ \exp\left(-\left(\frac{\omega-\omega_0}{2\sigma_\omega}\right)^2\right) & \text{with } \omega_0 = 4186\text{THz}, \sigma_\omega = 232.7\text{THz (25nm bandpass filter)} \end{cases} \tag{5.4}$$

From this spectrum an estimate of the emitted light pulse width can be made. Following [59], the inverse Fourier transform of the bandpass transmission curve gives the temporal width of the light pulse. The result is again Gaussian with $\sigma_t = \frac{1}{\sigma_\omega}$ which gives a σ_t of $25fs$ in the case of the $50nm$ bandpass filter and $\sigma_t = 50fs$ for the 25nm bandpass. This is the minimum length an OTR pulse can have by using bandwidth limited light. The 1D propagation of a light pulse in a linear medium is described by

$$E(t,z) = \int_{-\infty}^{\infty} \tilde{E}(\omega)\, \mathrm{e}^{-i(k(\omega)z-\omega t)} \mathrm{d}\omega \tag{5.5}$$

where $\tilde{E}$ is the spectral distribution of the pulse. When the spectral width is only a few % of the central frequency (as in the case here) and it is centered around some ω_0, one can expand the wavenumber $k(\omega) = \frac{n(\omega)\omega}{c}$ around ω_0. Keeping terms up to the second order term in the expansion $k = k_0 + k'\Delta\omega + k''(\Delta\omega)^2$ where k' is the one over the group velocity and k'' is one over the group velocity dispersion (GVD). Plugging this back into the eq.5.5 leads to $E = e^{(-ik_0 z)} e^{(-ik'z + i\omega_0 t)} \int_{-\infty}^{\infty} \tilde{E}(\Delta\omega) \exp\left(-ik''z(\Delta\omega)^2 + i\Delta\omega t\right) \mathrm{d}(\Delta\omega)$. With the Gaussian bandpass filters from eq.5.4 a normal Gaussian integral results and

the integral is evaluates to a Gaussian pulse due to the group velocity dispersion. The resulting stretched σ_s is given by

$$\sigma_s = \sigma_t \sqrt{1 + \left(\frac{k'' z}{2\sigma_t^2}\right)^2}. \tag{5.6}$$

In the whole optical system there are six lenses, all made from BK7 glass with a GVD of $100\frac{fs^2}{mm}$ at $450nm$. Each lens has $\sim 10mm$ thickness so the whole system will introduce a pulse stretching of $60mm$ BK7 which will stretch a $50fs$ OTR pulse at maximum to $\leq 600fs$ and a $25fs$ OTR pulse to maximum $\leq 1200fs$. Air has a GVD of $0.04\frac{fs^2}{mm}$ which is over three orders of magnitude smaller than the BK7 GVD. The total length in air is $\sim 10m$ which is ~ 2.2 orders of magnitude larger than the total length in BK7 so the effect of air is negligible. A fire protection window that is installed in the transport line has a similar GVD as BK7, but is only $1mm$ thick. So it can also be neglected.
It must be noted that this is a discussion about the σ of a Gaussian light pulse. Every single OTR light pulse broadens and such the whole pulse broadens by $0.6/1.2ps$. Every bunch broadens in each temporal direction. The time between two peaks is $\sim T/2$ so it is expected to wash out the modulation when the OTR modulation is shorter than $4.4ps$. This corresponds to $227GHz \leftrightarrow 6.4 \cdot 10^{14} cm^{-3}$. Thus the narrow band filter ($25nm$) has to be used for densities above $\sim 5 \cdot 10^{14} cm^{-3}$. The maximum frequency detectable is therefore around $450GHz$ with a narrow band filter far above the maximum frequency that is expected ($\sim 300GHz$ for $n_{pe} = 11 \cdot 14 cm^{-3}$). In summary this means that the setup is not washing out the modulation on the OTR light that has a periodicity T of $3.3 - 10ps$. The modulation of the light pulse is preserved. The smearing of the modulation for frequencies above $200GHz$ was observed and thus typically the $25nm$ filter was used when the expected micro-bunch frequency was above $200GHz$.

5.5 Time calibration of the streak windows

The streak time window length is important as it systematically shifts (see 4.2) any measured frequencies. Although the vendor already time calibrated the streak camera, the streak window lengths were checked again. The spatial half of the laser pulse of the fs-AWAKE laser pulse was sent through a piece of glass (24mm UVFS, thickness known within $0.1mm$) which adds a delay. The other spatial half is sent through air. The angle between the normal of the glass slab and the laser pulse propagation direction is $0 \pm 2.5°$. The delay Δt_l can be calculated from the laser central wavelength λ_0, the thickness of the glass d and the group index $n_g = \frac{c}{v_g}$, where v_g is the group velocity of the pulse at the laser wavelength in the glass. The delay is given by $\Delta t_l = d \cdot n_g/c - d/c$ the effect of air was approximated with vacuum. The laser has a central wavelength of 780nm and the corresponding $n_g = 1.468$ which results in $\Delta t_l = 37.47ps$ for the 24mm glass piece.From the resulting streak image a profile was made which can be seen in fig.5.15. Streaks without the laser pulse were subtracted from the image. Then every pixel was set to zero, which was below 2σ of the noise extracted from the background

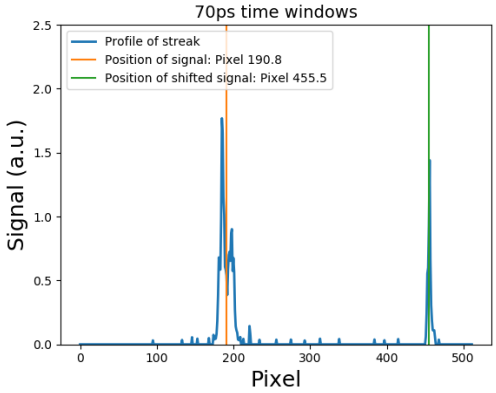

Figure 5.15: Time resolved profile with a laser pulse used to measure the time window length (blue line). The laser pulse appears twice due to the reflection in the glass slab. The orange and green line mark the mean time of each pulse.

images. This is why in fig.5.15 many pixels are exactly zero. This is necessary as small noise contributions can change the calculated mean position of the laser pulse. The position of the pulses was determined by calculating the expectation value of the signal position $<$ Signal $>= \sum$Signal $\cdot$ PixelNumber. Only the range from pixel 50 to pixel 300 was considered to calculate the mean value for the first peak which is the orange line in fig.5.15. For the shifted pulse the pixel range from 300 to 511 was chosen and the result is marked by the green line. In the profile figure shown in fig.5.15 the two pulses are shifted by an amount of 264.7 pixel which corresponds to a time window of 72.3ps for the streak camera. The measurement was repeated a hundred times for three different trigger delays such that the first pulse was once at the beginning, once in the middle and once located towards the end of the image. The resulting measured streak time window is plotted in fig.5.16 where the red dots represent the measured time window versus the median pixel position of the two pulses. The blue error bars represent the mean and its standard deviation of the corresponding measurements. On the three means a Bayesian maximum likelihood fit was made with a Gaussian prior at the nominal time window length of 73 ps (black curve, $\sigma = 1ps$). The posterior distribution is the green curve that is also Gaussian with its mean at 73.1ps which confirms the calibration supplied by the manufacturer. The systematic uncertainty on the time window is taken as the σ of the posterior distribution and is given by $\sigma = 0.4ps$. With a linearized error propagation model this translates to a DFT bin width δ_b of $\frac{1}{73.1ps} = 13.68GHz$ with a systematic uncertainty of $\Delta_b = 0.06GHz$ which corresponds to $\frac{\Delta_b}{\delta_b} = 0.5\%$. The same measurements were done for the $211ps$ time window. The prior is the black curve in fig.5.16 with mean $210.5ps$ and $\sigma = 1.5ps$. The posterior has its most likely value at $205.7ps$ which can be seen in the green curve. For the $\sim 200ps$ window I decided to use our value of $205.7ps \sim 206ps$. This is a considerate deviation from the vendor calibration of 2.5% and increases the uncertainty in the exact time window length. Due

a) b)

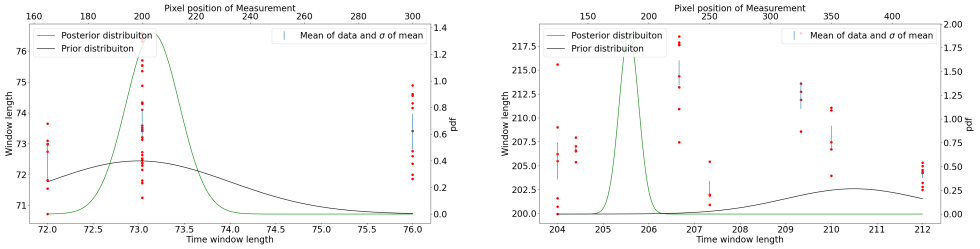

Figure 5.16: Measured corresponding time window length (blue points) with mean and standard deviation (blue line) for the different positions. Red: prior distribution for window length. Black posterior distribution of the time window length.

to the large discrepancy the time window uncertainty is taken to be $5.3ps$. This is larger than the σ of the posterior and corresponds to a uncertainty in the frequency bins $\delta_b = \frac{1}{205.7ps} = 4.86GHz$ of $\Delta_b = 0.12GHz$. This corresponds to $\frac{\Delta_b}{\delta_b} = 2.5\%$.

5.5.1 Linearization of time axis

The time axis of the streak camera is not linear. The steps to transform the streak camera images to a linear time axis are explained in the following. The task is to transform a signal S that is dependent on a nonlinear sampled time (t_n) to a signal $\tilde{S}(t_l)$ that is sampled by a linear time t_l with the same total length. The necessary transformation is defined by the need to keep the energy ($S(t_n)$ is in AWAKE proportional to power) a constant. Thus the condition for the transformation is $\int_{t_0}^{t_1} S(t_n)\mathrm{d}t_n = \int_{t_0}^{t_1} \tilde{S}(t_l)\mathrm{d}t_l$. There is no absolute value taken as all signals are strictly positive. The substitution rule enforces $\int_{t_0}^{t_1} S(t_n)\mathrm{d}t_n = \int_{t_0}^{t_1} S(t_n(t_l))\frac{\mathrm{d}t_n}{\mathrm{d}t_l}\mathrm{d}t_l$ and therefore the linear sampled signal is given by $\tilde{S}(t_l) = S(t_n(t_l))\frac{\mathrm{d}t_n}{\mathrm{d}t_l}$. For the streak camera the linear time axis is proportional to the number of pixels $t_l = c_l \cdot n_{px}$ and the dependence of the nonlinear time axis on the pixels is given by the vendor. The derivative of t_n depending on the number of pixels for the two relevant timescales $73ps$ and $206ps$ is shown in fig.5.17. Then $t_l = c_l \cdot n_{px}$, $\mathrm{d}t_l = c_l \cdot \mathrm{d}n_{px}$ and c_l is given by the time window length ($\frac{73}{512}ps$ and $\frac{206}{512}ps$ respectively). The measured window length with $206ps$ the complete curve was squeezed to $206ps$ instead of $210.5ps$. For a simpler resampling the derivative for each timescale is fitted by a quadratic fit (see fig.5.17).
The final resampling is then done with a linear interpolation (scipy.interpolate.interpolate1D) function. An example resampled signal is shown in fig.5.18. To correct for the nonlinear time axis every image taken has to be resampled along the time axis. All results hereafter use this re-sampling.

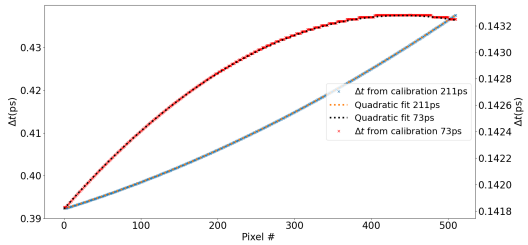

Figure 5.17: Red: Supplied Δt for $73ps$ and $206ps$ timescale and quadratic fit (black dotted) vs pixel number px. The quadratic fit for the $206ps$ timescale is $6.458 \cdot 10^{-8} \cdot px^2 5.600 \cdot 10^{-5} \cdot px + 0.392$. For the $73ps$ timescale it is $-7.507 \cdot 10^{-9} \cdot px^2 6.621 \cdot 10^{-6} \cdot px + 0.142$.

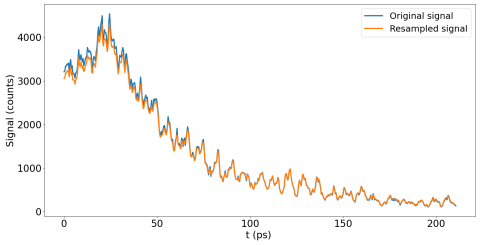

Figure 5.18: An AWAKE profile of a self-modulated bunch (blue solid line) and the resampled signal on the $206ps$ timescale (orange line).

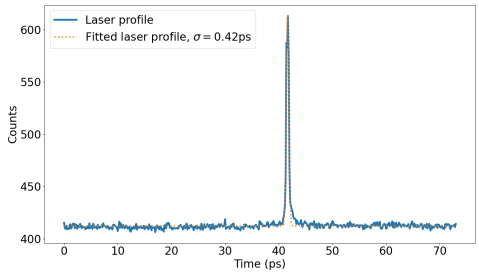

Figure 5.19: AWAKE $200fs$ laser pulse measured on the streak camera (blue solid line). The laser pulse is fitted with a Gaussian with $\sigma = 0.42ps$ (orange dotted line).

5.5.2 Time resolution of the streak camera

To test the temporal resolution of the streak camera the main AWAKE laser pulse (FWHM $\sim 120fs$)) was sent to the streak camera through the OTR transfer line. Then the streak camera measured the temporal width of the laser pulse. The measured Gaussian σ of the laser pulse is $0.42ps$. Since the temporal resolution for a long bunch train is of interest, the energy that is in the high frequency bins $|F_k|$ of the DFT during self-modulation experiments ($\sum_{1THz}^{2THz} |F_k|$) has been compared with the power in the DFT bins during the test setup (see 4.1.2). An example of this is shown in fig.5.20. The relative energy of the light pulse from the OTR for events are shown. The plasma density is $6.99 \cdot 10^{14} cm^{-1}$ and the energy of pulses from the test setup in chapter 4 with a $50\mu m$ slit and a cylindrical lens is also shown. The narrowband filter ($25nm$) is used in the streak images and the MCP and slit settings were always equal. The figure shows that the energy between the light pulse from the experiment is comparable with the energy from the tests which showed shown that the streak camera can detect modulation frequencies up to $450GHz$, which suffices. In fig.5.5.2 three example events (event numbers 1,10,35 of fig.5.20) are shown. The event ♯10 is a self-modulation event while the other two are beam-background images. As the self-modulation radially ejects a large part of the protons the energy of the OTR contained in the image is less than for the other two cases. Additionally the self-modulation spreads the beam across the image. The smearing along the slit and the energy in the self-modulated pulse is comparable with the experimental tests in chapter 4.

5.6 Software Integration and logging

The streak camera is integrated in the CERN FESA system which allows to control all settings. The software for the FESA system and a java GUI to control the streak camera was developed by David-Medina Godoy from the BE-CO-group of CERN. In the GUI the raw streak image is displayed and the settings of the streak camera can be modified.

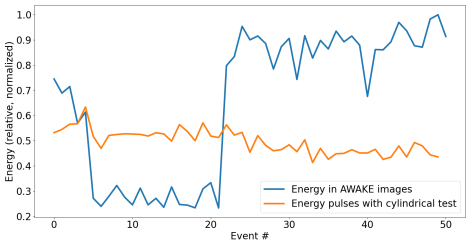

Figure 5.20: Comparison signal energy in AWAKE events and the test in chapter 4. The y-axis is normalized to the highest measured energy. The self-modulation events (blue line) ♯5 − 20 have less energy (about one third) of the energy that was used in the cylindrical tests (orange line), this means that the setup will not smear out the light modulation due to space charge effects in the camera and the conclusions from chapter 4 apply. The non-self-modulation events have ∼ double the energy than the modulated pulses in the laboratory.

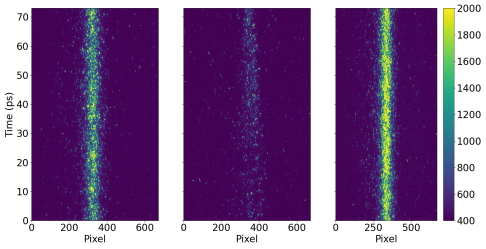

Figure 5.21: Three events (1 - left ,10 - middle and 35 - right) from fig5.20. The events are comparable to the tests with the cylindrical lens in energy. The cylindrical test smeared out the modulation over half the screen which also happens in the self-modulation event in the middle. Note that the colorscale is normalized to the event ♯35.

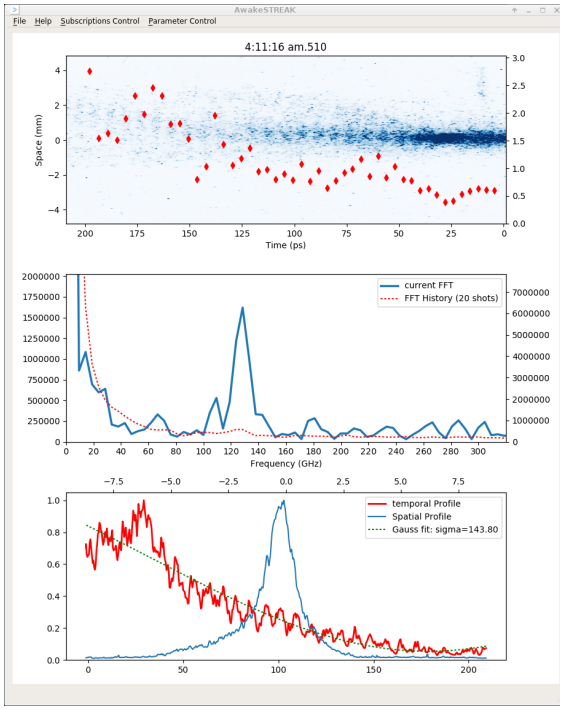

Figure 5.22: Python GUI to show diagnostics in real time. The Java GUI allows to change timing and streak settings. The Python GUI shows the streak image (top) with the beam radius for each ten pixels. The middle plot shows the discrete Fourier Transform (blue) and the averaged Fourier transform of the last 20 events (red). The bottom plot shows a longitudinal and transverse profile of the beam.

A second GUI was developed (python3 using PyQT5) that receives data from the CERN FESA system and allows to show custom defined processed camera data. A typical plot of the python GUI is shown in 5.22.
The motors used in this setup are STANDA stepper motors that only needed a minor modification in the connector to be compliant with the existing CERN BE-BI group software. The integration of the motors was thus done by using the already existing BI software. The BI drivers for the motors were also bought and integrated into a BI controlled system. The motor control is accessible by the AWAKE control application.

The data produced by the setup (images, settings, etc.) is stored by the CERN logging database and the AWAKE EventBuilder (developed by S. Gessner) and accessible over the CERN network. A list of the most important recorded data (either stored in the eventBuilder or the CERN logging database, LDB) is given in table 5.2.

Description	Location	Path
Streak Image	eventBuilder	AwakeEventData/XMPP-STREAK /StreakImage/streakImageData
Streak Gain	eventBuilder	AwakeEventData/XMPP-STREAK /StreakImage/streakImageMcpGain
Streak Time window	eventBuilder	AwakeEventData/XMPP-STREAK /StreakImage/streakImageTimeRange
Streak Info comment	eventBuilder	AwakeEventData/XMPP-STREAK /StreakImage/streakImageInfo
MPP-Streak tube fine trigger	CERN LDB	MPPAWAKE:FASTTRIG-1:STREAKTUBE
MPP-Streak CMOS fine trigger	CERN LDB	MPPAWAKE:FASTTRIG-1:STREAKCMOS
MPP-streak Focussing Mirror position X	CERN LDB	MPPAWAKE:TSG41-MIRROR-1:MMPOS
MPP-streak Focussing Mirror position Y	CERN LDB	MPPAWAKE:TSG41-MIRROR-2:MMPOS
MPP-streak Filter Wheel position	CERN LDB	MPPAWAKE:TSG41-WHEEL-1:MMPOS

Table 5.2: Table of most important stored data. Not all data stored is included in this table. Note that the Streak Info comment has all metadata about the streak camera settings included.

5.6.1 Timing

Three fast and precise trigger signals used for the streak camera and a general SPS timing signal needed to trigger the acquisition of streak images are delivered to the streak hut.

For AWAKE the timing between the ionizing laser pulse and the proton bunch is key. The CERN timing team (lead by Heiko Damerau) designed and installed the timing system for the AWAKE experiment. The AWAKE laser pulse that creates the relativistic ionization front is the reference for the SPS bunch and all timings are derived from its master oscillator. The CMOS camera of the streak camera has a readout trigger and the streak tube has an independent trigger. This allows to use the streak camera in a time-integrated mode as a normal camera synchronized with the laser pulse and the proton bunch ("focus mode"). This allows to place the OTR of the proton bunch on the slit of the streak cameras without any timing constraints (a very long exposure of the streak CCD makes a "free running" untriggered mode possible).
The trigger going to the streak camera can be delayed in coarse steps of double the main AWAKE oscillator frequency which corresponds to $5.6ns$. Then a finer delay can be adjusted which allows the trigger to be precise within tens of picoseconds (nominally $10ps$ stepsize). During the first runs it was observed that the trigger delay can be off from the selected value by $\sim 30ps$. It is assumed that the physical hardware of the trigger causes this as it switches between physical delay lines. In the first dataset the trigger delay could only be adjusted very coarse ($\sim 30ps$) which is almost half the window. This turned out to be not problematic as the goal in this work is to identify the self-modulation and the problem was solved in later runs where a more precise trigger was needed.
The first overlap of the SPS proton bunch and the laser pulse was achieved using the streak setup discussed. For the overlap down to 50ns a photodiode was used that collected the OTR from the beam and low power laser light. Below 50ns difference the streak camera was used to see the low power laser pulse (a filter that additionally decreases the low power laser energy $\sim \mu J$ by another six orders of magnitude was inserted in the laser pulse path) and the proton bunch OTR on the same image. To see the OTR and the laser pulse the $450nm$ bandpass filter was switched to a neutral density filter (ND1). This allowed to place the laser pulse within in the bunch with $\sim 20ps$ precision. Note that this is not influenced by any trigger jitter or the uncertainty on the trigger as this moves only the captured time window. Delays between the laser pulse and the proton bunch of up to $50\mu s$ were introduced without problems. This allowed this setup to measure the decay of the plasma and a detailed analysis of the hosing instability [67] or the evolution of the plasma column [68].

Proton bunch length characterization

The setup allows a temporal characterization of the proton bunch. Simulations predict that the micro-bunch frequency is independent of the length of the proton bunch length. The nominal SPS proton bunch length is $\sigma_z = 400ps$ and the streak camera setup measured typically $\sigma_z \sim 350ps$ for the SPS proton bunch. The proton bunch can be

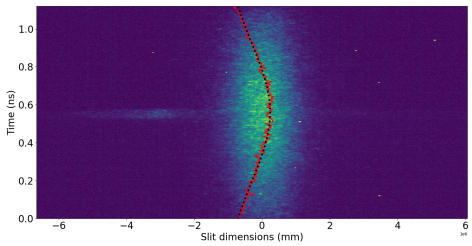

Figure 5.23: One of the first images that show the temporal overlap of the AWAKE main laser pulse with the proton bunch. The laser pulse is in low power mode and attenuated by filters to not destroy the streak camera. A strong signal from the laser pulse is visible on the left of the proton bunch at around $600ps$. The laser pulse position does not indicate whether the laser pulse is spatially overlapping with the proton bunch. The bunch length is $\sigma_z = 355ps$ and the bunch width is measured to be $\sigma_r = 0.62mm$. A profile of the bunch with a Gaussian bunch length fit is shown as the overlay.

shortened to $\sim 260ps$. The bunch is shortened by rotation in longitudinal phase space [69]. When this bunch rotation was on, the streak camera setup measured a Gaussian bunch length of $\sim 220 - 260ps$. This shortened bunch has a higher charge density which leads to a faster development of the self-modulation instability. This was observed with this setup.

5.7 Streak setup in the experiment

The floor of the AWAKE experimental area has a 3° slope while the streak camera room has a flat floor but is not in a 90° angle to the beam axis but rather $\sim 35°$. This leads to a rotation of the beam image on the streak camera and the axis of the bunch that the slit cuts out can be calculated by transfer matrix operations as $\sim 30°$. To check the orientation of the slit on the OTR foil, the proton beam has been moved in $200\mu m$ steps in the x and y direction of the beam coordinate system up to ± 1 mm. The slit of the streak camera was opened completely and the movement of the beam center was tracked in focus mode. For each direction the beam was fitted with a Gaussian envelope and the fitted mean was recorded. The resulting tracks show the rotation of the streak camera slit with respect to the beam x and y axis, as depicted in fig.5.24. In the experiment the beam is expected to be modulated symmetrically radially. The orientation of the slit is only important when aligning to other diagnostics as those usually use the x-y axis defined by the transverse beam plane and not the slit plane. The measured angle of the x-shift with respect to the x-axis of the streak is $-51°$ and the angle of the y axis shift with respect to the streak slit is 21°.
Note that these values depend on the exact settings of the mirrors that couple the OTR

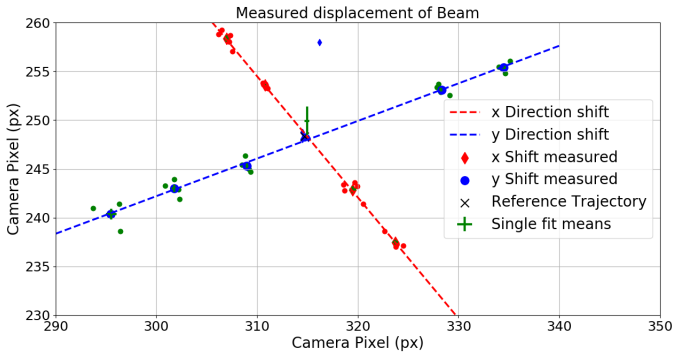

Figure 5.24: Measurement to show the rotation of the bunch image through the transport line. The proton bunch was displaced from the reference trajectory where the two lines cross in the x and y direction. The Beam center was calculated by fitting a Gaussian envelope to the beam image and a straight line was fitted to the measured beam centers. The x-axis of the image is also the x-axis of the camera. The beam shift in the y direction has a 21° slope, while the shift in x-direction has a −51° slope.

in and out the transport line. For the first experiments (where this measurement applies) it was found that the transport line was not imaging the beam completely symmetrically (this was later changed to obtain symmetric images) but was preferring one slit half (the "left" side in all images shown in this work). This could be the reason for the discrepancy between calculated rotation (35°) and measured rotation (21°) and why the two axes are not perpendicular to each other.

During the experiment it was necessary to put the image of the proton bunch on the streak camera into focus. This was done by streaking the beam on the nanosecond timescale and creating a time summed profile. The resulting spatial image is fitted with a Gaussian and the resulting spatial width is recorded. Then the final focusing lens is moved by the translation stage and the measurement is repeated. The resulting bunch widths vs the translation stage position can be seen on image 5.25. The fitted Gaussian bunch width $\sqrt{2}\sigma$ is given in pixel and the quadratic fit is shown as the orange line. The starting position of the final lens was 7000 steps and the final value was set to 8750 steps. The translator has $150mm$ of travel range and needs $\sim$ 35000 steps to cover the whole range, thus the change of the lens position was about 7.5mm, the calculated magnification is unchanged by this change. With a camera pixel size of $6.5\mu m$, a magnification of 0.23 and a minimum pixel width of 28.1 (corresponding to $\sqrt{2}\sigma_r$) the resulting σ_r is $562\mu m$. This is in good agreement with the expected $\sigma_r = 557\mu m$, given by the emittance of the AWAKE beam and the propagation distance ($\sigma = \sigma_0 \left(1 + \frac{z^2\epsilon^2}{\sigma_0^4}\right)^{1/2} \sim 0.56mm$, for $\epsilon = 2 \cdot 10^{-6} mm - mrad$,$z = 13.5m$ and $\sigma_0 = 0.2mm$). Note that this is the un-modulated bunch width.

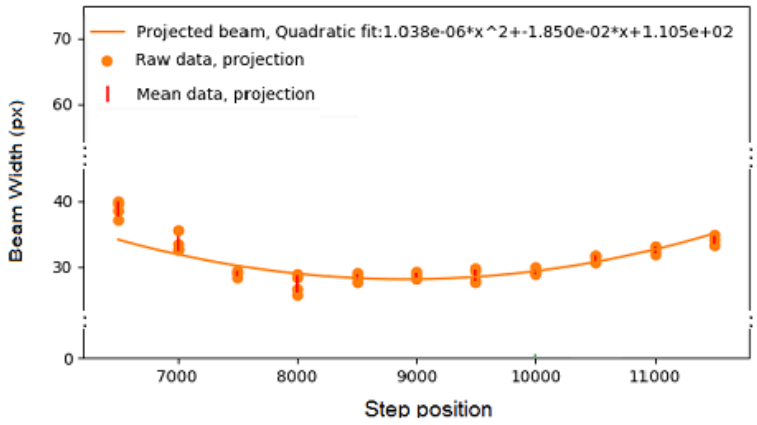

Figure 5.25: Bunch size in pixels versus final lens translator position. The size is at its minimum for the translator at position 8750.

After the lens position was finalized the slit position within the beam was determined. The beam itself is visible as a Gaussian spot on the streak camera, when the camera is used in focus mode. The slit cannot be opened more than $200\mu m$ so the beam is always cut and the full Gaussian spot is not visible. Without the bandpass filter or a ND filter the beam is very bright on the camera and it leads to saturation effects. These do not allow to fit a Gaussian beam profile in two directions. To determine the slit position within the beam the slit is narrowed and the motorized mirror that couples the OTR light out from the transport line is used to sweep the beam across the slit. The captured intensity is determined and normalized for each mirror position by integrating the image over the slit. The final intensities I are fitted to the formula

$$I = erf((u - x)/2\sigma) - erf((l - x)/2\sigma) \tag{5.7}$$

where u, l are the upper and lower cut due to the slit, σ is the beam size and x is the mean of the Gaussian beam. The function erf is the error function. This fit assumes that the bunch has a symmetrical Gaussian transverse shape and the slit acts as a cut on the Gaussian spot. Transverse measurements of the bunch showed that the transverse bunch shape can be fitted with a Gaussian function so eq.5.7 can be applied. The resulting fits for two different slit openings can be seen in fig.5.26. Note that all quantities, as for example the beam center and also the intensity, depend only on the mirror step position. So all values are measured with respect to that quantity. In fig.5.26(a) the slit was opened to $100\mu m$ and the resulting mirror step position to obtain maximum intensity, and thus center the Gaussian spot on the slit, is 7069 ± 4 steps. The same measurement was in this case repeated with a slit opening of $30\mu m$ and the result is shown in (b). Again the best mirror position according to the fit is 7069 ± 4 steps which is expected as the slit mean closing position on the CCD image moves less than pixel between fully open and fully closed.

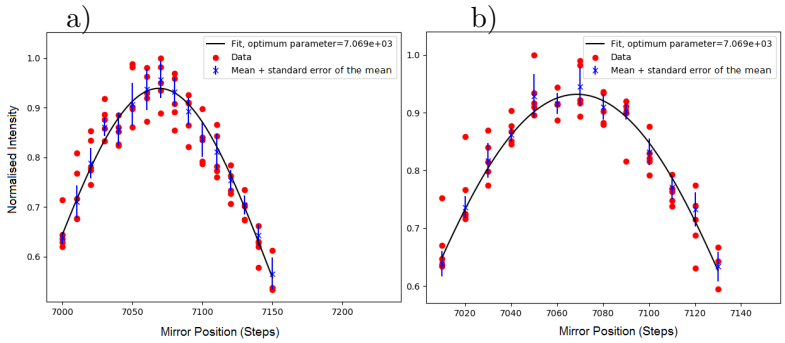

Figure 5.26: Image (a) shows the measured beam intensity vs the mirror position. The slit was opened to $100\mu m$ and the fit of the data with eq.5.7 states that for a mirror setting of 7069 steps the beam center is placed in the middle of the slit. In figure (b) the same result was obtained when the slit is closed to $30\mu m$ which shows that the slit position is independent of the slit width.

The focusing and slit position depend on the beam trajectory so these measurements were regularly repeated. The focusing did not need much adjustment but when the beam was not set to its reference trajectory the slit position was not in the middle of the beam. In operation it was not necessary to set a new slit position because the beam could be set back to the original position by the SPS, which turned out to be very precise and easy.

5.8 Conclusion

The optical streak camera system for the AWAKE experiment has been presented and characterized. The optical system was a full success in all AWAKE runs until 2021 and was key in understanding the self-modulation process. The setup was used in a number of important AWAKE experiments and delivered many other important contributions such as detection of the hosing instability [67], the micro-bunch charge [70] or the characterization of the self-modulation instability with linear density gradients [71]. Before all of these results, this setup showed the frequency dependency of the self-modulated bunch, that will be presented in the next chapter. Note that in the very first experiments (very late 2016, early/mid 2017) the self-modulation of proton bunches in a plasma channel itself was not yet detected and thus many effects that were detected with this setup were not yet understood.

6 Proton bunch self-modulation observation at varying plasma densities

The preceding chapter has introduced the measurement setup for the time resolved proton bunch diagnostics in AWAKE. In this chapter the results from the first self-modulation experiments will be presented. Most of the data was obtained in the Mai/June 2017 runs. It will be shown that long proton bunches indeed self-modulate in a plasma and that the self-modulation is initiated with a relativistic ionization front (RIF) created by the laser pulse. It will be shown that the modulation frequency of the micro-bunches can be very well described by the cold plasma electron frequency f_{pe}. The results of this chapter have been published as "Experimental Observation of Proton Bunch Modulation in a Plasma at Varying Plasma Densities", PHYSICAL REVIEW LETTERS 122, 054802 (2019).

6.1 Bunch-plasma interaction at large timescales

In this section the effect of the plasma created by the RIF is discussed. The time-resolved images taken by the streak camera show that the bunch only interacts with the Rubidium vapor behind the RIF and show that the self-modulation is induced by the RIF. A small but interesting detail is that before the detection of the self-modulation it was not clear whether the self-modulation instability would occur when the laser pulse is placed far ahead of the proton bunch or at the beginning of the proton bunch. It has been observed experimentally that at low Rubidium densities and for the laser pulse far ahead of the bunch the hosing instability does occur and competes with the self-modulation instability [67]. Nonetheless the self-modulation instability has been observed when the RIF is placed far ahead of the proton bunch and is thus not seeded with the laser inside the bunch [67].

When no Rubidium vapor or high-power laser pulse is present, figure.6.1 a) shows a time-resolved image with a nanosecond time scale. The red profile (from the region shown by the white lines) on the side of the streak image shows the time profile of the proton bunch obtained by summing the image along the spatial dimension. In this image the bunch population is $3.0 \cdot 10^{11} p^+$ and the measured bunch length is $\sigma_z = 250ps$ (corresponding to $\sigma_z \sim 7.5cm$) as determined by the Gaussian fit of the profile (dashed green line). The temporal position of the laser pulse can be seen as the horizontal line ($t \sim 0.45ns$, $< 4mm$) by the laser on the left side of the image. When Rubidium vapor is present with the laser pulse placed inside in time (see fig.6.1 b) and space of the proton bunch, the laser pulse ionizes the Rubidium vapor on a short timescale

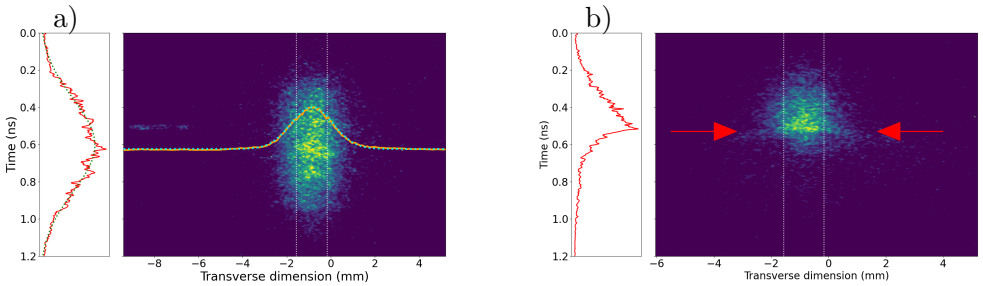

Figure 6.1: a) Time resolved image of the proton bunch without plasma. The bunch is on the right hand side of the image and the short laser pulse on the left hand side. The red temporal profile is fitted with a Gaussian function with $\sigma_z = 250ps$. The transverse profile is the orange overlay and the cyan Gaussian fit has a σ_r of $0.60mm$. (b) Image with plasma ($n_{Rb} = 2.1 \cdot 10^{14} cm^{-3}$, $3 \cdot 10^{11} p^+$) and ionizing laser pulse (blocked, not visible) placed as in (a). The effect of the plasma ($t > 0.5ns$) is visible in the image and on the bunch profile (red line). The red arrows point to the visible, symmetrically de-focussed protons behind the laser.

($\tau_{ionize} \ll \tau_{Laser} \ll 1/\omega_{pe}$). Only the second half ($t > 0.5ns$ in fig.6.1 b)) of the proton bunch propagates in, and can interact with the plasma. This corresponds to the cut-bunch propagating in a plasma that was presented in chapter 2. This enhances the initial wakefields created by the step of the bunch charge in the plasma and initiates the self-modulation process. Further the initialization of the self-modulation suppresses other instabilities like the hosing instability [67], which competes with the self-modulation instability.
In fig.6.1 b) the back part of the proton bunch is affected by the combined presence of the laser pulse and vapor and thus of the plasma. The self-modulation effect de-focusses a significant fraction of the protons propagating in the plasma. In chapter 5 it was shown that the OTR from protons that are de-focussed transversely to the slit is not transmitted by the optical setup. OTR from protons that are de-focussed along the slit is transmitted up to $\sim$ 5mm radius (corresponding to the transverse dimension in fig.6.1 a and b). The charge density of de-focussed protons becomes low for larger radii ($\geq 2.5mm$) and the slit collects only a small part of the wide charge distribution. Thus the proton bunch signal for large radii is faint behind the laser.
Directly behind the laser pulse that creates the RIF in fig.6.1 b) there are two rapidly expanding line of charge to the left and right of the bunch axis (red arrows). The self-modulation instability is radially symmetric and these lines of charge are the radially de-focussed protons between the micro-bunches. The protons are ejected due to the effect of transverse wakefields in the plasma. The images in fig.6.1 and 6.2 are taken with the $1.2ns$ time window of the streak camera which has $\sim 12ps$ time resolution and this resolution is not enough to resolve the micro-bunches behind the laser pulse.

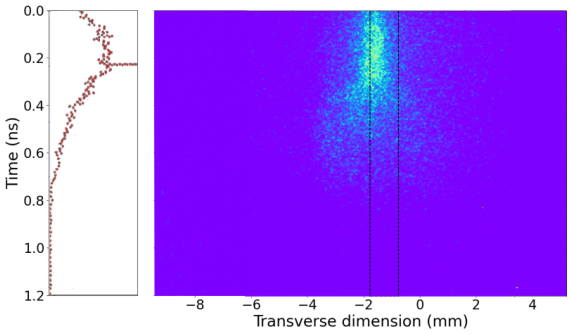

Figure 6.2: Example image with the ionizing laser pulse located in the first half of the bunch at $\sim 0.2ns$ and the self-modulation starting behind the laser. The bunch population is $1 \cdot 10^{11} p^+$ and the Rubidium density is $n_{Rb} = 3.7 \cdot 10^{14} cm^{-3}$. The streak camera setting are such that the bunch charge behind the laser pulse is only visible up to $\sim 0.5ns$ but the profile (created from the black lines) shows that there is a charge trails up to $0.8ns$.

The time resolved de-focussed protons can be seen in section 6.2.3. Directly behind the laser the bunch charge on axis drops rapidly but a faint trail of charge can be seen in the image that is visible in the profile. Placing the RIF ahead of the temporal bunch center also leads to a heavily affected bunch behind the relativistic ionization front. This can be seen in fig.6.2 where the laser is placed at the $\sim 0.2ns$ time mark. The bunch has one one third of the charge of the bunch in fig.6.1. The initial wakefield strength depends on the driving charge of the cut bunch and the smaller step in charge leads to a slower growth of the self-modulation instability along the bunch. Still the bunch is fully self-modulated behind the RIF and the instability modulation growths along the bunch such that with the camera setting no visible charge remains on axis. The trailing charge can be seen in the profile but again no modulation frequency is detected due to the low time resolution. In the next section it will be shown that a significant amount of charge remains along the bunch axis and this charge is made of micro-bunches generated by the self-modulation. Images were taken with Rubidium vapor densities ranging from 1.3 up to $10.6 \times 10^{14} cm^{-3}$. These densities correspond to plasma frequencies (modulation periods) of $102.4GHz$ ($9.8ps$) and $292.3GHz (3.4ps)$.

6.2 Micro-bunch detection for different plasma densities

In this section the detection of the micro-bunch frequencies for different Rubidium densities is discussed. On the long timescale a strong de-focussing effect on the proton bunch behind the RIF can be seen up to the point that it appears there is no charge left behind the RIF. This section will show that there is charge left behind the RIF and

there is a train of micro-bunches on the bunch axis. The method presented in chapter 4 to distinguish a frequency signal from noise is used. The background images for the DFT power spectra are images of the proton bunch with no Rubidium or laser pulse present and that have the same streak camera settings as the self-modulation image. It was observed that a gradient of the Rubidium vapor (and thus the plasma density) leads to a change in the self-modulation frequency [72],[63]. For the data used in this work the gradient over $10m$ was always $\leq 1\%$ measured by an white light interferometer technique that can measure the Rubidium vapor density with a precision of $\leq 0.5\%$ [73], [74].

6.2.1 Micro-bunch train

The long timescale images (fig.6.1-6.2) show that behind the RIF the bunch density is less than from the un-modulated bunch and the long time window does not detect remaining charge on the bunch axis. The defining feature of the self-modulation is the existence of the train of micro-bunches on axis. This train can be directly seen with self-modulation images at low Rubidium (and thus plasma) density of $\sim 1-2\cdot 10^{14} cm^{-3}$ and $206ps$ time window. Figure 6.3 a) shows an example self-modulation image where the micro-bunches are visible along the whole time window. This event corresponds to the case that is shown in fig.6.1 a). The transverse and longitudinal wakefields grow along the bunch and the transverse effect of the wakefields leads to an ejection of protons out of the bunch. The initial transverse wakefields along the bunch are small and the protons in the de-focussing part of the wakefield are not ejected very far. The orange arrows point to protons in the de-focussing phase that get ejected further out along the bunch and with increasing wakefield development. It is visible that the growth of the wakefields along the bunch is so strong that after ~ 4 wakefield periods the protons are ejected further than $\sim 2.5mm$ from the bunch and the signal becomes faint due to the low charge density and the decreasing OTR light capture efficiency. Along the bunch axis a "spine" of charge remains, visible along the bunch shortly behind the laser. These are the protons in the focussing part of the wakefield that drive the plasma resonantly. A few late micro-bunches on the bunch axis are marked with red arrows. Note that a lot of charge is still present outside of this "spine" (de-focussed protons) but it is distributed over the whole image from $-2.5mm$ to $2.7mm$ and has a much lower density so it is not as visible as the micro-bunches. The image scaling limits are set in a way to increase the visibility of the micro-bunch train. The Rubidium density of $2.03\cdot 10^{14} cm^{-3}$ corresponds to $f_{pe} = 128.0GHz$ when the Rubidium is 100% ionized. A profile, given by the white lines, is selected in the image. The profile is shown on the left of fig.6.3 a). The (windowed, see section 6.2.2) DFT power spectrum of the profile (and thus the "spine") has a clear peak which is interpolated at $130.6 \pm 3.1GHz$. This is in agreement with the measured Rubidium density and $\sim 100\%$ ionization. In summary the image shows the three main features of the self-modulation: A train of micro-bunches on the bunch axis, radially symmetric de-focussed protons between the micro-bunches (so it is not the hosing instability, which has a distinctive, look see e.g. [67]) and the micro-bunch modulation frequency is close to f_{pe}.

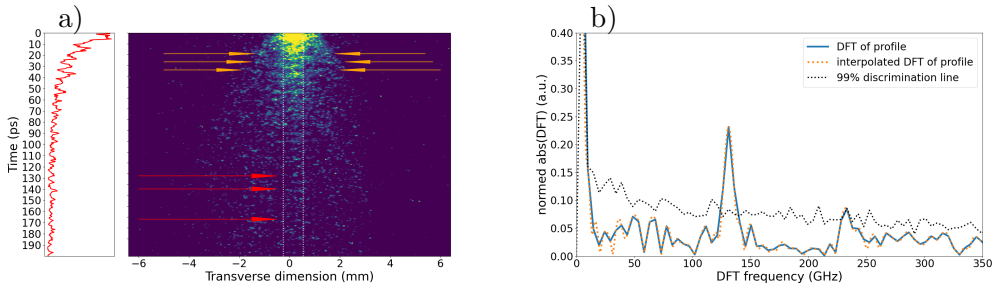

Figure 6.3: a) Time-resolved image with a Rubidium density of $2.03 \cdot 10^{14} cm^{-3}$, corresponding to a plasma frequency of $128.0 GHz$. The laser is at time $\sim 0 ps$ and placed in the middle of the proton bunch. The bunch is $\sim 360 ps$ long. The density on axis (red overlay on the left) is decaying but short micro-bunches stay visible for along the entire length of the bunch (small red arrows). The radial symmetry can be seen by the de-focussed protons near the laser (orange arrows). b) The DFT power spectrum of the windowed bunch profile (blue line, interpolation orange dotted) shows a peak at the interpolated frequency $130.6 \pm 3.1 GHz$ that is above a 99% discrimination threshold (dotted black line, see chapter 4).

When the laser pulse is placed early in the bunch, the train of micro-bunches also develops. This can be seen in fig.6.4 a) where a self-modulation event on the $206 ps$ time window is shown that corresponds to the case in fig.6.2. The laser is placed $\sim 200 ps$ before the incoming bunch middle and is in the image detectable by the elongated first micro-bunch behind the RIF that shows an increased charge density starting at $\sim 10 ps$. It has been shown that the first micro-bunch is consistently elongated when seeding the self-modulation instability [65], this allows to infer the laser position in the image at $\sim 9 - 10 ps$ which is marked by the green line. The white lines mark again the selected profile region, which is shown on the left of fig.6.4 a). Behind the laser pulse the formation of the micro-bunches is visible and the earliest detectable ejected protons are marked by the orange arrows. The protons are ejected symmetrically and due to the slow growth of the transverse wakefields the de-focussed protons stay in the imaged region for a long time. This is in contrast to fig.6.3 where the protons leave, due to the stronger transverse wakefields, the imaged region within a few micro-bunches. Many micro-bunches behind the laser, there are still radially ejected protons visible (up to the time mark $\sim 100 ps$) while later they become undetectable due to the reduced light collection efficiency. Two different effects lead to the slower growth of the wakefields along the bunch and thus to the slower ejection of the protons. The first is reason is that the laser pulse is placed early in the bunch. The step at the cut is lower and the initial wakefields driven by the bunch are smaller. The second is that the low charge of the bunch, which consists of only $1.05 \cdot 10^{11} p^+$, drives initial wakefields with only one third of the magnitude of a bunch that has $\sim 3 \cdot 10^{11} p^+$. The red arrows point to later micro-bunches that form

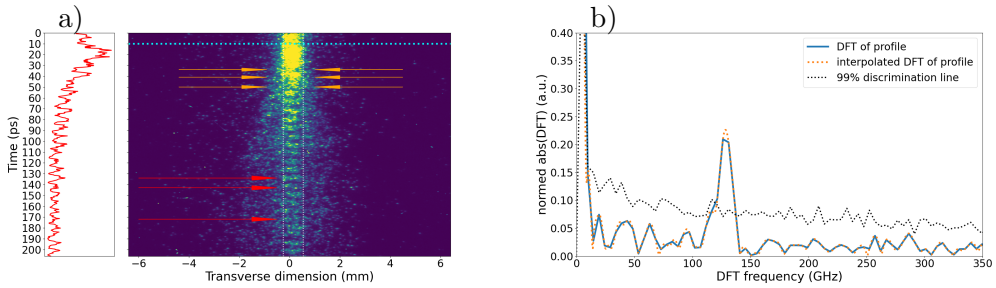

Figure 6.4: a) Time-resolved image with a Rubidium density of $2.03 \cdot 10^{14} cm^{-3}$, corresponding to a plasma frequency of $128.0 GHz$. The laser is at position $\sim 10 ps$. The total bunch charge is $1.05 \cdot 10^{11} p^+$ and the laser is placed early in the bunch ($\sim 200 ps$ ahead of the center). The laser position is marked by the green line. Orange arrows point towards the first visible ejected protons and red arrows point towards some later on-axis micro-bunches. The red overlay on the left shows the central profile (white dotted lines).
b) The DFT power spectrum of the profile in a) (blue line) shows a clear peak above the detection threshold (black dotted line) at the interpolated (orange dotted line) frequency $128.0 GHz \pm 2.5$.

the "spine" of charge that is visible along the bunch axis which resonantly drive the plasma and create large longitudinal wakefields. In the DFT power spectrum of the profile (fig.6.4b) a peak can be identified which has its maximum at $128.0 GHz$. This corresponds again to f_{pe} that equals the Rubidium density ($2.03 \cdot 10^{14} cm^{-3}$) and 100% ionization.
At higher Rubidium densities the self-modulation is reaching saturation very fast and due to the time resolution ($\sim 2 ps$) the setup can not resolve the micro-bunches over the whole bunch length within the $206 ps$ time window. Still the setup can show the three qualitative main features at Rubidium vapor densities of the self-modulation, as shown in fig.6.5 a) and b). With a Rubidium density of $3.67 \cdot 10^{14} cm^{-3}$ (corresponding to $f_{pe} = 172.0 GHz$ at full ionization) an increased on-beam-axis density can be seen in the orange overlay on the right of fig.6.5 a). The overlay is created by cutting the image into $12 ps$ long slices and averaging those over time. At the beginning the beam is still focussed but the bunch becomes symmetrically broader and broader at later times with a small peak remaining at the center which is made out of the micro-bunches. The distribution becoming broader is due to the effect of the radially ejected protons. The central profile (from the white lines) is shown on the left of fig.6.5 a). In this image no frequency is detected in the DFT power spectrum of the single profile by using the method developed in chapter 4. In fig.6.5 b) the average DFT power spectrum of 12 profiles created from similar events is shown and a peak appears at $172.6 GHz$. The appearance of the peak above the detection threshold shows that the charge peak at the center of the image contains a charge modulation near $f_{pe} = 172.0 GHz$. Again it

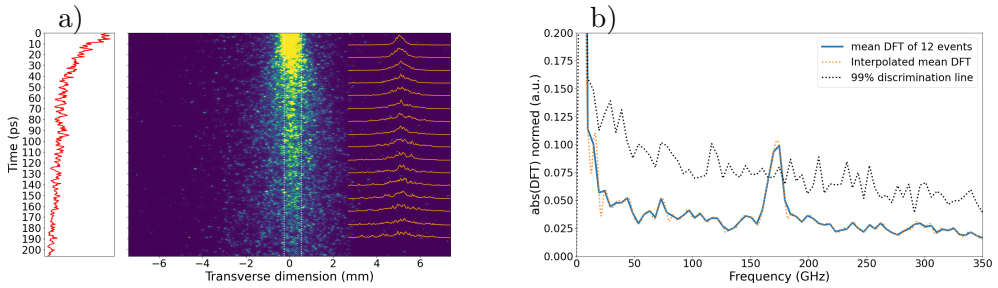

Figure 6.5: a) Self-modulation image with a Rubidium density of $3.67 \cdot 10^{14} cm^{-3}$, corresponding to a plasma frequency of $172.0 GHz$. The laser is at position $\sim 0ps$. Visible is that the density on axis (red overlay on the left) is decaying and that the bunch has a symmetric radial modulation (orange overlay on the right). The streak camera time-resolution does not allow to identify micro-bunches per eye or in the single event DFT power spectrum (not shown).
b) An average over 12 normalized DFT power spectra (blue line) of the on axis profiles reveals a small peak at $172.6 \pm 4.1 GHz$ (orange dotted interpolation) above the detection threshold (dotted black line).

is notable that the deflection of the protons from the central spine occurs slower than in fig.6.3 a) which is due to low charge ($0.98 \cdot 10^{11} p^+$ in fig.6.5 a, $\sim 1.0 \cdot 10^{11} p^+$ for the other 11 events) in the bunch.

6.2.2 Windowing and frequency uncertainty

In fig.6.6 a) a self-modulation event for a Rubidium density of $2.03 \cdot 10^{14} cm^{-3}$ within the $206ps$ window is shown. In fig.6.6 b) the selected profile (white lines in a)) can be seen. While peaks from the self-modulated bunches are visible in the profile, the most prominent feature is the overall decay of the signal intensity along the bunch. This is because at later times in the bunch the protons are de-focussed further than those that are closer to the RIF (at $\sim 0ps$ in a) and b)), the overall charge becomes less due to the Gaussian envelope and the micro-bunches become shorter in time. In the DFT power spectrum of the profile the large decay is a high amplitude, low frequency, component that is convoluted with the rectangular windowing function of the streak window. The rectangular window DFT power spectrum has a main lobe that is narrow. The FWHM frequency of the rectangular window for a time window with length t is $\frac{1.8955}{t\pi}$, which corresponds to $8.3 GHz$ for the $73ps$ time window and $2.9 GHz$ for the $206ps$ window. The side lobes of the rectangular window are large, e.g. the first side lobe is only $13dB$ below the main lobe and the higher side lobes decay with $\sim -6dB$ for the first few side lobes and even less for > 10 bins from the main lobe. This leads to a leakage of the strong signal (the overall decay in fig.6.6 a,b)) into the neighboring bins. This can be seen in the DFT power spectrum of the profile on fig.6.7 a) together with a zeropad interpolation

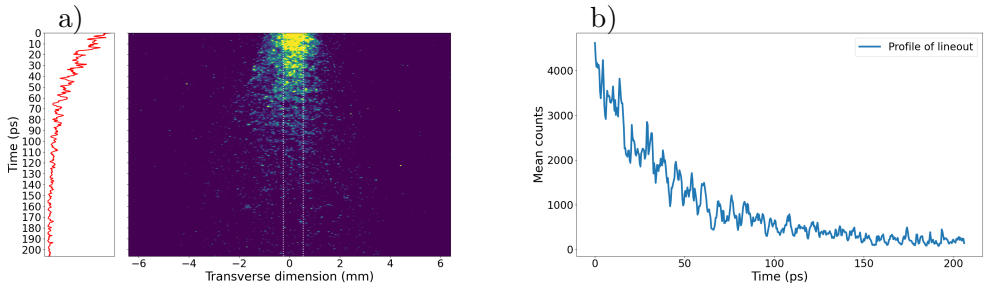

Figure 6.6: Example event with a Rubidium density of $2.03 \cdot 10^{14} cm^{-3}$, corresponding to a plasma frequency of $128.0 GHz$. The laser is at position $\sim 0 ps$ and placed in the middle of the proton bunch. The profile of the lineout marked by white lines is shown on the left of a) and in b). The profile shows micro-bunches but the overall decay of the signal is the most visible feature in b).

and a discrimination line for frequency detection. The frequency discretization of the interpolation is $1 GHz$. A small peak is above the discrimination line at $133 GHz$ and the leakage from the low frequency signal mixes with the peak from the micro-bunches. Applying a different window function instead of the rectangular window increases the width of the main lobe but suppresses the side lobe peaks and thus suppresses the effect of the low frequency component of the signal. For example the Hann window (for n time points in a window with length N given by $\sin\left(\frac{n}{\pi N}\right)$) has a first side lobe peak of $-33 dB$ and the side lobes decay with about $10 dB$ per bin for the first few bins. This greatly reduces the influence of the low frequency component on the self-modulation frequency peak. This comes at the costs of a broader main lobe,as for the Hann window the main lobe has a FWHM of $\frac{3.18}{t\pi}$ (t is the window length) and a decreased signal sensitivity. In fig.6.7 b) the DFT power spectrum of the profile multiplied by a Hann window is shown together with the interpolation and the discrimination line for a signal. The peak is now clearly distinguishable and has its maximum at $131.6 GHz$ (compared to the $133.0 GHz$ without windowing). All profiles showed a low frequency component, thus a windowing function was always used to minimize the effect of the signal decay.

A single isolated frequency in the profile leads to a full width half-maximum (FWHM) of the interpolation that is given by the used window ($\frac{3.18}{t\pi}$ for a Hann window). The interpolated FWHM is broader than the single frequency peak and the difference of the FWHM single frequency peak to the measured FWHM is taken to be the frequencies that are contained in the measured measured signal besides the main frequency component. In fig.6.8 the windowed interpolated DFT peak is compared to an artificial windowed signal with a single frequency that is located at the measured frequency. The FWHM (red arrows) of the interpolated peak is from $123.3 GHz$ to $137.4 GHz$ leading to a FWHM of $14.1 GHz$. The single frequency peak has a FWHM of $4.9 GHz$, thus the frequency of the modulation is determined to be $130.1 \pm 4.6 GHz (= (14.1 GHz - 4.9 GHz)/2)$. This method was used to determine the σ of the single frequency measurements.

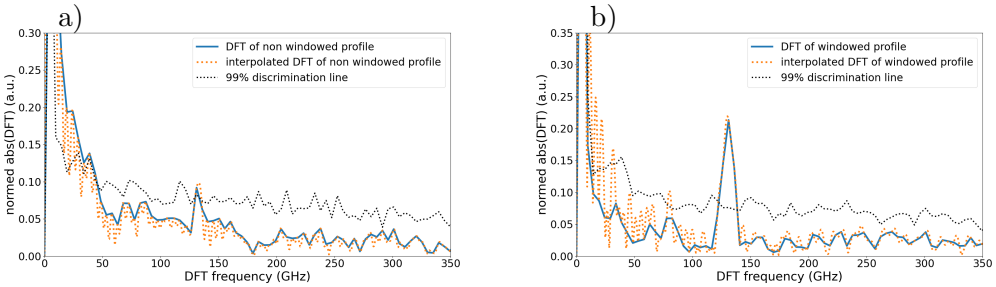

Figure 6.7: a) the DFT power spectrum of the profile in fig.6.6 b). The large low frequency leaks into the higher frequencies and suppresses the peak of the microbunch frequency. The peak is hardly visible and its maximum is interpolated at $133.0 \pm 4.3 GHz$. In b) a Hann window was applied in the profile to suppress the leakage of the large low frequency signal into higher bins and a clear signal at $130.1 \pm 4.3 GHz$ appears.

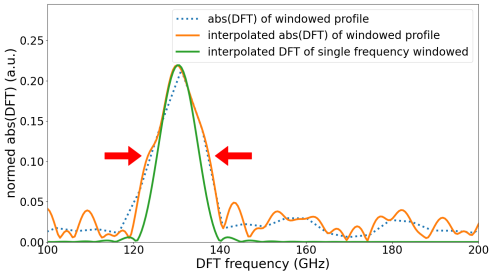

Figure 6.8: Comparison of the width of the windowed profile (blue dotted line - interpolation in orange solid) with the width of a single frequency peak (green line). The standard deviation of the measured frequency variable is taken at the FWHM of the windowed interpolated peak minus the FWHM of the single frequency peak divided by two. The red arrows locate the FWHM height.

6.2.3 Micro-bunch frequency for varying plasma densities

Self-modulation events with Rubidium densities ranging from $1.3 - 10.6 \cdot 10^{14} cm^{-3}$ have been acquired in the first experimental runs. In this section it is shown that either the micro-bunches can be seen directly in the time-resolved images or the DFT power spectrum picks up a single peak in the charge "spine" behind the RIF. This is true for all measured Rubidium densities. The events considered as self-modulation events were selected by hand from all of the events for a given Rubidium density. For the images a peak-search range from $80GHz - 450GHz$ was chosen for Rubidium densities below $7.88 \cdot 10^{14} cm^{-3}$. For Rubidium densities above the search range was $150 - 450GHz$.

Self-modulation at a Rubidium vapor density of $2.57 \cdot 10^{14} cm^{-3}$

At a low Rubidium density the micro-bunches are seen on the time resolved images and $73ps$ time window. In fig.6.9 a) the micro-bunches can be seen starting behind the laser pulse (and therefore the RIF) that is located just outside the time window at $\sim -5ps$. For the DFT power spectra two regions of interest (ROI) have been selected, shown by the white and yellow lines in fig.6.9 a). The larger ROI (ROI1) ranges from $-0.7mm$ to $+1.2mm$ and the smaller ROI (ROI2) ranges from $-0.3mm$ to $+0.5mm$. The ROIs are chosen in such a way that they have the bunch in their center. If the beam has a measurable drift along the slit the ROIs were shifted to keep the bunch in the middle of the ROI. The final fit of the frequency dependency of the micro-bunches was done for both ROIs independently. In the profile to the left ROI1 is shown in gold and ROI2 in red. The overall decay of the charge density on axis can be seen in the profile. The collected photon density per ps from the radially extended protons is too low to allow seeing the radially de-focussed protons except for the first few micro-bunches. For the times $0ps - 20ps$ the integrated transverse wakefield action is small and the protons are only ejected a tiny amount away from the axis. Averages of many images (done in later works) show the radially de-focussed protons on the $73ps$ timescale [32][65]. The interpolated DFT power spectrum (Hann window applied) for both ROIs shows a peak at $143.8GHz$ for this self-modulation event. The peaks are broad as the FWHM of the peak for both ROIs is $34.0GHz$. This is much larger than the FWHM of a single Hann windowed peak ($13.8GHz$). The expected modulation period for $143.8GHz$ is $6.9ps$ which leads to 10.5 micro-bunches in the whole window. This is consistent with the counted number of micro-bunches in the image (~ 10.5). The large width of the peak might stem from the observation that the micro-bunches do not only become less intense at later times but also have a less steep edge (see profiles) along the time direction at later times. Also at very early times the protons are not yet ejected from the micro-bunch train. The first distinguishable micro-bunch in the profile is at $\sim 20ps$ while the laser pulse is earlier. This has the same effect as a single elongated bunch at the beginning of the self modulation instability. In this image the typical elongated first bunch is not fully observed (it is cut at the very top of the image). This means that the effective modulated bunch is only $\sim 60ps$ long and this increases the minimum FWHM of the windowed peak already by $\sim 3GHz$. This already shows that there is not a single

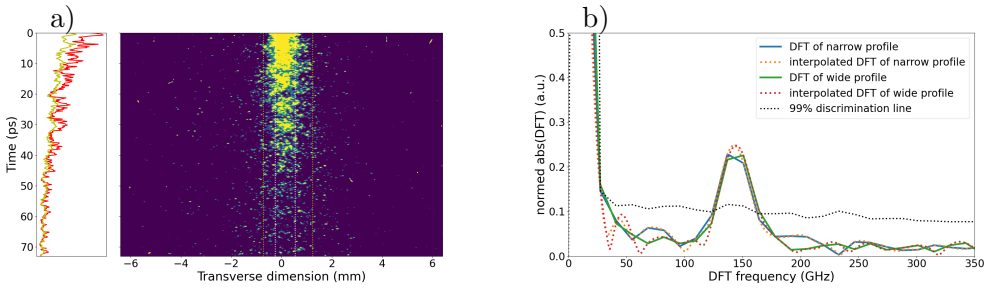

Figure 6.9: a) Example time-resolved image with a Rubidium density of $2.57 \cdot 10^{14} cm^{-3}$, corresponding to a plasma frequency of $144.0 GHz$. The streak-trigger-laser delay is $0 ps$ and the laser is placed in the middle of the bunch (bunch population: $3.38 \cdot 10^{11}$). The profile for the white ROI is shown on the left in red. b) DFT power spectra (blue and green solid lines) of the selected profiles in a) with Hann windowing function. For both ROIs a peak is interpolated (orange and red dotted lines) at $143.8 GHz$ with a half-width that is $10.1 GHz$ larger than a single frequency Hann window peak half-width.

frequency in the bunch

Self-modulation at a Rubidium vapor density of $6.99 \cdot 10^{14} cm^{-3}$

At low frequencies, as in the preceding section, the micro-bunches are visible. At higher frequencies (corresponding to Rubidium vapor densities $\geq 5 \cdot 10^{14} cm^{-3}$) the narrowband filter in the system ($25 nm$ bandwidth) has to be used to ensure the time resolution of the camera and the modulation becomes much less visible (see section 5.4). In fig.6.10 a) a self-modulation event with the laser pulse nominally in the middle of the image is shown. Although there is no laser marker in the image, the position of the laser pulse (and thus the RIF) can be inferred by the increased signal peak in the image, marked by the red arrow in fig.6.10 a). The red profile (corresponding to ROI2) has an increased charge density at $\sim 20 ps$ time. This sets the laser pulse and the onset of the modulation at the $\sim 18 ps$ time mark [65]. The offset between the laser pulse position ($\sim 18 ps$) and the middle of the image is due to streak-trigger to laser pulse jitter and because the precise trigger could only be shifted with coarse ($\sim 30 ps$) steps. The micro-bunches are hardly visible in the image, but periodic peaks can be guessed in the profile (easiest to spot at the times $50 - 70 ps$). These peaks correspond to the micro-bunches. The DFT power spectra of the selected ROIs are shown in fig.6.10 b). The DFT spectra show clearly dominant peaks at $228.8 GHz$ and $232.8 GHz$ for the two ROI cases. For the ROI2 the peak is the only signal above the discrimination line, while for the ROI1 there are low frequency bins above the discrimination line. The peak that has the largest relative height (compared to the detection threshold) above the discrimination line has been chosen as the self-modulation frequency which is the bin at $228.8 GHz$. With a higher Rubidium density the initial wakefields are stronger and the self-modulation

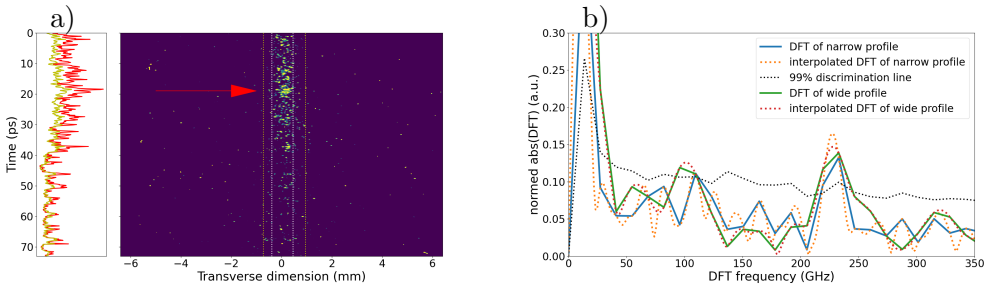

Figure 6.10: a) Time-resolved image with a Rubidium density of $6.99 \cdot 10^{14} cm^{-3}$, corresponding to a plasma frequency of $237.4 GHz$. The streak-laser delay is $30 ps$ and the laser is placed in the middle of the bunch (bunch population: $3.20 \cdot 10^{11}$). The laser is around the $20 ps$ mark (not visible) and the self-modulation starts behind the laser. The profile for the white ROI is shown on the left in red. b) DFT power spectra of the selected profiles in a) with Hann windowing function (solid blue and green line). A peak is interpolated (oranged dotted line) at $228.8 GHz$ for ROI2 (white lines). For the ROI2 the peak maximum is interpolated (red dotted line) at $232.8 GHz$. Both peaks have a one sided FWHM that is $10.2 GHz$ larger than a single frequency peak FWHM.

develops faster. The protons are ejected radially earlier in the bunch and the density of the de-focussed protons is too low to be detected at these Rubidium (and thus plasma) densities. Still the setup is able to detect the modulation frequency in a single event. The FWHM of the peaks is for both ROIs $10.2 GHz$. One reason for this large peak width is that in this event the modulation does not occur at the beginning of the image but only after $\sim 27\%$ of the time window. This reduces the number of visible micro-bunches and thus the frequency resolution. The Hann window main lobe FWHM of a $53 ps$ time window is $19.1 GHz$ which is $5.2 GHz$ larger than the main lobe of a $73 ps$ time window. This alone would reduce the FWHM to $7.6 GHz$ without any other effects, e.g. again the development of the micro-bunches or the elongated micro-bunch after the laser pulse.

Self-modulation at a Rubidium vapor density of $10.6 \cdot 10^{14} cm^{-3}$

At the highest measured Rubidium density of $10.6 \cdot 10^{14} cm^{-3}$ the expected self-modulation frequency is $292.4 GHz$. From the tests of the streak camera (see section 4.3), it is expected that the response of the camera drops sharply at an imposed frequency of $\sim 300 GHz$ to a value that decays only slowly to the detection threshold at $450 GHz$. The DFT of the events at this high Rubidium density show that the setup is near its resolution limit. Still single event detection of the self-modulation frequency is possible. In fig.6.11 a) a self-modulation event with a Rubidium density of $10.6 \cdot 10^{14} cm^{-3}$ is shown. The RIF is at the beginning of the image at $\sim 0 ps$. The RIF is placed in the middle of the bunch. In the image itself no traces of micro-bunches can be seen. Also in the

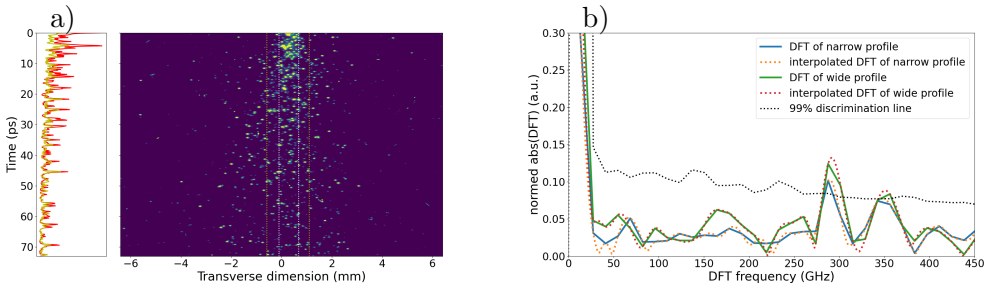

Figure 6.11: a) Example event with a Rubidium density of $10.6 \cdot 10^{14} cm^{-3}$, corresponding to a plasma frequency of $292.4 GHz$. The streak-laser delay is $0 ps$ and the laser is placed in the middle of the bunch (bunch population: $2.89 \cdot 10^{11}$). The profile for the white ROI is shown on the left in red. b) DFT power spectra of the selected profiles in a) with Hann windowing function. For the small ROI a peak is interpolated at $289.0 GHz$ with an additional half-width of $6.0 GHz$. For the large ROI a peak is interpolated at $291.8 GHz$ with an additional half-width of $7.5 GHz$.

profiles of the ROIs there is hardly a trace of micro-bunches visible. Some clear peaks in the profiles (e.g. the ones at $\sim 20-30 ps$ and at $\sim 55-70 ps$) do have a time-distance that corresponds roughly to the expected frequency ($\sim 3.3 ps$). In the Hann-windowed DFT power spectra of the profiles that is shown in fig.6.11 b) one can see that there is a peak in the DFT spectra. The DFT power spectrum peak for the narrow ROI is barely above the discrimination line. The sidelobe at $350 GHz$ is below the discrimination line for ROI2. The larger ROI has a clearer peak. The second peak at $350 GHz$ is above the discrimination line for the ROI1. As this event is the only event that has a second peak and the peak at $300 Ghz$ is larger the peak at $350 GHz$, the peak at $300 GHz$ is chosen as the detected frequency. The interpolated measured frequency depends slightly ($\sim 1\%$) on the ROI chosen and the detected frequencies are interpolated at $289.0 GHz$ and $291.8 GHz$, respectively. The FWHM of the peaks is $7.5 GHz$ (ROI1) and $6.0 GHz$ (ROI2). Since the peaks are only barely above the discrimination it is possible that part of this width comes from the background noise.
Data was acquired for more Rubidium densities and below I show the resulting fit of the micro-bunch frequency on axis vs. the Rubidium density.

6.3 Fitting the micro-bunch frequency

For each measured Rubidium density the mean m of the N ($N = 5-20$) measured self-modulation frequencies f_i at that density is calculated as $m = \sum_{i=0}^{N-1} f_i/N$. Every single measurements is independent ($Cov(f_i, f_j) = 0$ for measurement $i \neq j$) and the variance of the mean is given by $Var(m) = \frac{1}{N^2} \sum_i Var(f_i)$ as an estimate of the uncertainty of the mean. Here $Var(f_i)$ is the estimated variance of a single measurement and is given

by the square of the width of the measured peak. The mean has an added systematic uncertainty given by the uncertainty of the window length which is 0.5% in case of the $73ps$ window and 2.5% in case of the $206ps$ window (see section 5.5). This is added in quadrature to the variance of the peak width. The measured modulation frequency of the micro-bunches is to zeroth order expected to be equal to the plasma frequency $f_{pe} = \frac{1}{2\pi}\sqrt{\frac{e^2}{m_e\epsilon_0}}n_{pe}^{1/2} = 89.8\beta^{1/2}\sqrt{\frac{n_{Rb}}{10^{14}cm^{-3}}}GHz$. The degree of ionization of the vapor by the laser pulse is not known and the model used to fit the detected modulation frequency is given by $f_{mod,detected} = f(\alpha, \beta, n_{Rb}) = 89.8\beta^{\alpha}(\frac{n_{Rb}}{10^{14}cm^{-3}})^{\alpha}GHz$. Here β can be interpreted as the degree of ionization of the Rubidium vapor and α as the exponent for the frequency dependency. I will argue in the next section that one should interpret α and β more broadly as a probability distribution over the outcome of the experiment.

6.3.1 α and β as experiment realization dependent variables

For a given Rubidium density there is no single micro-bunch frequency in the bunch for a given degree of ionization, which means that α does not have a single value. As mentioned, the first micro-bunch after the RIF is elongated. Depending on the transverse wakefield growth the first few micro-bunches are not distinguishable in the time-resolved images, as the protons are not ejected far enough for micro-bunches to be formed. This effect can be seen in fig.6.9 a) for the first two micro-bunches. Also the wakefield phase velocity is smaller than the proton bunch velocity which leads to a dephasing between micro-bunches and wakefields. This changes the wakefields and in turn changes the exact micro-bunch frequency depending on the position within the bunch. This means that there is not a single frequency in the micro-bunch train as the modulation depth of the bunch train grows along the bunch but more a center frequency.
A further argument is that only in the zeroth order approximation the beam does not influence the plasma frequency. Yet the beam ions contribute towards the plasma ion column density which sets the restoring force for the plasma electrons. In first order approximation one can add the beam density to the ion density which influences the exact local plasma frequency. This contribution is not insignificant for the precision of the measurements done here. For a long bunch with $3 \cdot 10^{11}p^+$ and $\sigma_z = 12cm$, $\sigma_r = 0.02cm$ the charge density at the beginning of the plasma cell is $4\% \cdot 10^{14}cm^{-3}$. For a shortened bunch with $\sigma_z = 8cm$ the contribution increases to $\sim 6\% \cdot 10^{14}cm^{-3}$. Thus for even the highest density of $10.6 \cdot 10^{14}cm^{-3}$ the bunch density is on the order of $0.4 - 0.6\%$. For lower Rubidium vapor densities the influence increases accordingly. As the bunch charge used in the data here varies between $1 - 3 \cdot 10^{11}p^+$ and the bunch length varies from 240 to $380ps$, the charge density for the bunches varies by a factor of 5 (for low charge beams the charge density can become as low as 20% of bunches with maximum charge density) and thus the contribution to the restoring force on the plasma electrons is different. The time-resolved images show that the influence of the bunch charge on the growth of the self-modulation instability (see e.g. fig.6.5) is significant [75]. It was measured (with this setup) that the charge density in the first micro-bunches is $\sim 60\%$ of the charge density of the un-modulated bunch [76]. This means that the bunch charge density on axis is on

the order of $\geq 1\%$ of the plasma density as the un-modulated bunch. Thus the focussed (and maybe even de-focussed) beamlets contribute to the exact micro-bunch formation (and thus frequency) far within the plasma and the appearance of multiple frequencies close together is not an artifact but a physical effect. Simulations and experiments [65] have shown that there is no single frequency in the self-modulated bunch and that the exact modulation frequency depends on at which exact radius of the bunch the frequency is measured.
This means that not a single value for α can be expected but for a given ionization one expects frequencies close to f_{pe} that corresponds to $\alpha = 0.5$.
Conversely β is not only determined by the degree of ionization of the plasma. The setup measures the bunch after it left the plasma so it can not measure directly effects that happen in the plasma. Only the integrated effect of all influences within the plasma and the propagation after the plasma is detected. There are effects in the plasma-bunch interaction that can lead to differences in the micro-bunch frequency with two different events even though the plasma density and the corresponding values of α are the same in both. This creates an environment where β should not only be interpreted as the degree of ionization of the plasma but as a random variable that describes different outcomes of the self-modulation experiments used in the first AWAKE runs, depending on the exact realization of the event. There are effects in AWAKE that can lower the self-modulation frequency. For example the laser pulse does not create an plasma column with an infinite radius but a cylindrical shaped plasma with a radius of $\sim 1.5-2mm$ [77]. The alignment between the proton bunch and the plasma channel is not perfectly coaxial. If the bunch and the laser have a misalignment at the beginning of the plasma cell the proton bunch travels in a plasma with $< 100\%$ ionization or near the edge of the channel. In both cases this can lower the micro-bunch frequency.
Simulations show that protons in the bunch are ejected further than the plasma channel radius ($\sim 1.5mm$ radius), so not the complete proton bunch travels in the plasma. The protons later in the bunch do exit the plasma channel at some time and the same happens with the plasma electrons. Thus the approximation of an infinite plasma is not true.
In total there are more effects in the experiment that lower the plasma frequency that increase the plasma frequency which is supported by the data taken here. In fig.6.12 the distribution of the relative measured frequencies $m_f = \frac{f_{measured}-f_{pe}}{f_{pe}}$ for all measured events in the $73ps$ time window is shown together with a fit of the form $(m_f - 0.0087)^{0.0339} e^{\frac{(m_f-0.0087)}{0.04416}}$ when $m_f < 0.0087$ and 0 else. Here f_{pe} corresponds to the Rubidium density assuming 100% ionization. The distribution peaks a little bit below 0 ($\sim 1.5\%$), which corresponds to $f_{pe} = m_f$. Only a fraction of the events has a measured micro-bunch modulation frequency above f_pe and there is a long tail towards lower frequencies. This is in agreement with a model that has many influences on the plasma frequency where more lower the micro-bunch frequency than raise it. For the reasons discussed here I argue that, in accordance with Bayesian analysis, one should not expect one true value for β and α, but β and α are random variables that have, depending on the realized experiment outcome, different values.

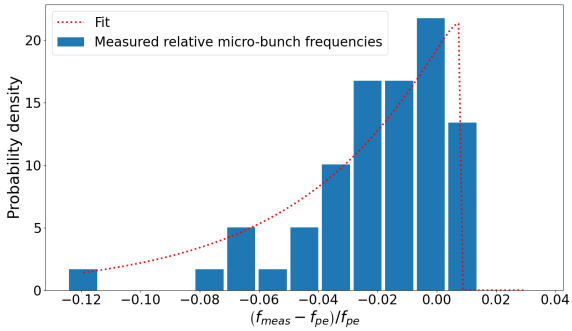

Figure 6.12: Probability distribution of the relative deviation of the measured micro-bunch frequency (blue bars). A fit to the distribution is shown with the red dotted line. The distribution is in accordance with an experiment where there are many contributions that can lower the modulation frequency but only a few can raise the modulation frequency.

6.3.2 Bayesian fit

For the narrow and the wide ROI a Bayesian fit of the measured mean modulation frequency of the micro-bunches was made. In table 6.1 the mean measured frequencies for the evaluated data is presented. The priors for the fit parameters used are a Gaussian dis-

Rb density ($\frac{1}{10^{14}cm^3}$)	1.29	2.13	2.21	2.57	3.67	3.67	4.79	6.99	7.88	10.6
ROI1 (mean, GHz)	102.9	125.1	134.9	142.1	169.2	173.1	193.5	234.1	247.7	290.4
ROI1 (σ, GHz)	5.1	3.1	1.5	2.6	5.7	1.9	4.2	4.8	4.9	2.7
ROI2 (mean, GHz)	102.0	125.8	134.1	141.7	169.6	172.6	191.6	232.5	249.9	289.7
ROI2 (σ, GHz)	4.9	3.1	1.7	2.6	5.7	2.2	4.2	4.5	4.9	2.5
Window (ps)	206	73	206	73	73	206	73	73	73	73

Table 6.1: Mean measured data, all frequencies are in GHz, standard deviation from time window not included.

tribution with $\mu = 0.5, \sigma = 0.01$ for the exponent α and a prior $p(\beta) = e^{\frac{\beta-1}{l_0}}/l_0, l_0 = 0.05$ for $\beta \leq 1$ and $p(\beta) = 0$ elsewhere. These values are chosen because of the strong prior assumption that the frequency is close to f_{pe} and no secondary ionization occurs. This high belief in the prior is due to lacking of other resonant frequencies for the plasma electrons. When interpreting β purely as the degree of ionization the chosen prior belief excludes the possibility for secondary ionization by the laser pulse. This is justified because the ionization potential for secondary ionization is $27.3eV$ which is ~ 6 times as high as the energy for first ionization ($4.2eV$) and strongly suppressed. The missing appearance of high frequency outliers in fig.6.12 further increases the confidence in the prior assumption that second ionization of the Rubidium is unlikely. The full two di-

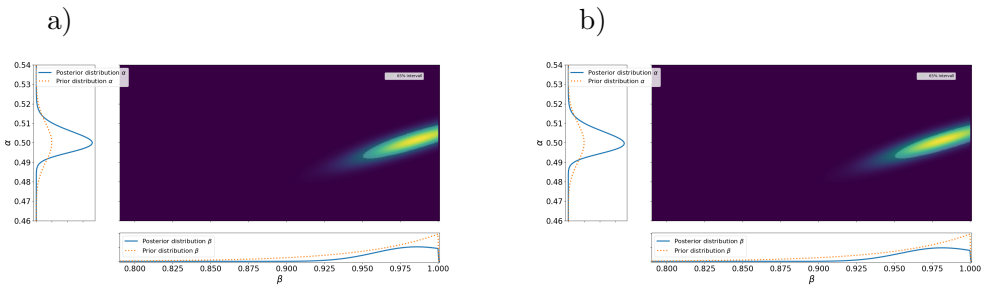

Figure 6.13: Bayesian fit for ROI1 (a) and ROI2 (b). The mode for the marginalized distributions in a) is $\alpha_{mode} = 0.500$ and the standard deviation is $\sigma_\alpha = 0.006$, $\beta_{mode} = 0.986$ $\sigma_\beta = 0.019$. The mode for the marginalized distributions in b) is $\alpha_{mode} = 0.500, \sigma_\alpha = 0.006$ and $\beta_{mode} = 0.981, \sigma_\beta = 0.020$. Next to the marginalized probability distributions the prior distributions are shown in dashed-red.

mensional prior $P_0(\alpha, \beta)$ is the product of the two independent priors.
The posterior distributions $P(\alpha, \beta|D)$ (D are the measured data points) have been calculated numerically by gridding the parameter space and applying Bayes Theorem:

$$P(\alpha, \beta|D) = \frac{P(D|\alpha, \beta)P_0(\alpha, \beta)}{\int P(D|\alpha, \beta)P_0(\alpha, \beta)d\alpha d\beta} \tag{6.1}$$

The probability of the data with respect to the model $P(D|\alpha, \beta)$ is taken to be normally distributed with the standard deviation given by the standard deviation of the data.

$$P(D|\alpha, \beta) = \prod_{m_i} \frac{1}{\sqrt{2\pi}\sigma_i} e^{\frac{(m_i - f(\alpha,\beta))^2}{2\sigma_i^2}} \tag{6.2}$$

The gridding parameters extend far enough such that the prior distributions integrate numerically to one. The numerical integration was done using the python package scipy [27]. For the ROI1 the resulting posterior distribution for the parameters α and β is shown in fig.6.13 a) and in fig.6.13 b) the posterior distributions is shown for ROI2. It is evident in the posterior distribution that the posterior value for α is no longer independent from β (as it was in the priors) but α and β have a positive correlation (ROI1: 0.88, ROI2: 0.89) which is calculated with the Pearson correlation coefficient [78] $\rho = \frac{CoV(\alpha,\beta)}{\sigma_\alpha \sigma_\beta}$. This introduces a dependency of the exponent of the factor β but the prior assumed values of $\alpha = 0.500, \beta = 1$ lie still in the two dimensional 65% credible interval, that is shown in fig.6.13 a,b) with a shaded region. An independent probability distribution for α of β is given by the marginalized probability distribution. For ROI1 and ROI2 these are shown on the left of fig.6.13 a,b), respectively. For both ROIs the posterior mode value is 0.500 and the distribution has a numerically evaluated standard deviation of 0.006. This shows that the exponent is, with the precision of these measurements, indistinguishable from the single value that is predicted by assuming a

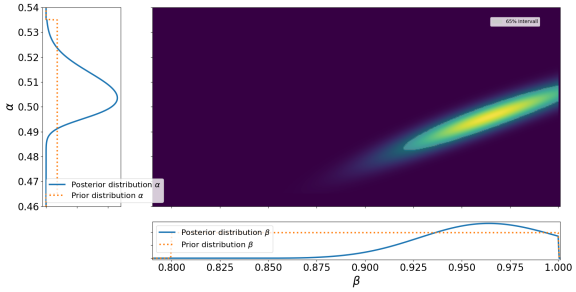

Figure 6.14: Posterior distribution of α, β with a flat prior (red dashed line), $\beta \in [0.875, 1.01]$ and $\alpha \in [0.465, 0.535]$.

cold linear plasma response (exponent = 0.5). The marginalized distributions for β are shown in fig.6.13 a,b) on the bottom. The distribution of β independent of α has its mode as 98.6%/98.1% (ROI1/ROI2) with a numerically evaluated standard deviation of 1.9%/2.0%. When β is interpreted as the ionization factor, full ionization of the plasma channel is still within the 65% credible interval and should therefore not be rejected.
Using a flat prior ($\alpha \in [0.46, 0.54]$,$\beta \in [0.85, 1.01]$) means being more indifferent to prior predictions. The flat prior explicitly allows a $\beta > 1$, up to $\beta = 1.01$. The posterior two dimensional distribution for α, β together with the marginalized distributions are shown in fig.6.14. The posterior distributions shows again that α and β are correlated ($\rho = 0.92$). The marginalized distribution of α is centered around the mode 0.504 ± 0.008. So the posterior distribution of α is only weakly dependent on the prior (the data is "strong") and will always result in a distribution that is maximal around 0.5. Allowing for a $\beta \geq 1$ (corresponding to a second ionization of some Rb Atoms) does not change the posterior in a significant way. The mode value for β is $96.4 \pm 2.7\%$. Using the small ROI leads to very similar results. When using a flat prior, $\beta = 100\%$ is no longer in the 65% credible of the marginalized β distribution interval, which ends at $\beta = 99.1\%$.
In fig.6.15 the measured mean modulation frequencies together with a fit that uses the mode values and the two dimensional 65% credible interval are shown for ROI1 and ROI2. Fig.6.15 is the main result of this work. The figure shows that the micro-bunches that are detected in single event time-resolved images have a periodicity that is very well described by the cold-electron plasma frequency. The difference between the large ROI and the small ROI is not big enough to be visible on fig.6.15. These results show that the power dependency of the modulation frequency of the micro-bunches is in agreement with that of the plasma frequency. The marginalized posterior distributions of α are in agreement with the predicted value 0.5 for a Gaussian prior and an indifferent flat prior distribution. These measurements are precise enough to show that the plasma frequency is the dominant micro-bunch modulation frequency.

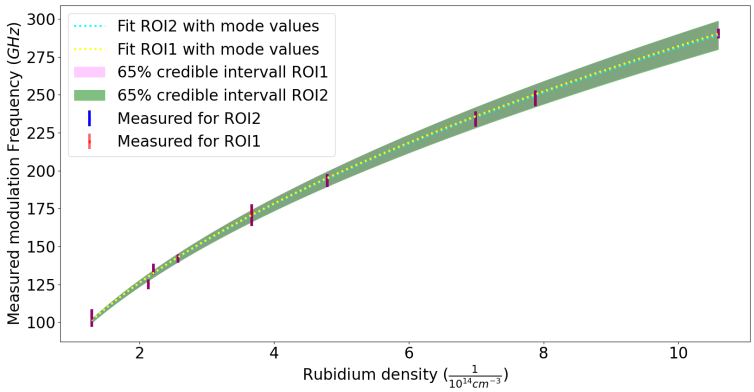

Figure 6.15: Fit to the measured micro-bunch frequencies with the mode values for ROI1 in yellow. The green shaded regions includes all fits that lie in the 65% credible interval. The mode fit for ROI2 is under the mode fit for ROI1 and not visible due to the small differences. The 65% credible interval for ROI2 coincides also with the 65% credible interval of ROI1.

6.4 Conclusion

In this chapter the designed and tested setup to acquire time-resolved images of the self-modulated proton bunch was used to directly evidence the self-modulation instability and measure the frequency of the micro-bunch train. It was shown that the self-modulation can be induced by placing a RIF within a proton bunch and that there is a micro-bunch train behind the RIF. It was shown that there clearly is a micro-bunch train behind the RIF. A Bayesian analysis shows that the periodicity of the micro-bunches is described within 1.5% precision by the cold plasma electron frequency $f_{pe} = \frac{1}{2\pi}\sqrt{\frac{e^2}{m_e\epsilon_0}}n_{pe}^{1/2}$ and assuming 100% ionization. The Bayesian analysis further concludes that a 100% ionization of the plasma channel is in the 65% credible interval and compatible with the measured modulation frequencies. Further it was shown in later works [79] that the phase stability of the seeded self-modulation has been determined to be within $\sim 6\%$. This means that in a well-controlled environment, the self-modulation is very reproducible, which makes it possible in principle to accelerate externally injected electrons [80]. Observing the seeded self-modulation was key for the acceleration of externally injected electrons in the wake-fields driven by long proton bunches [80]. The results presented here with a relativistic ionization front (as opposed to a sharp rising charge distribution as in [81] or [82]) show for the first time the initialization and the development of the self-modulation of a long charged particle bunch in a plasma which was the main goal of this thesis. At long timescales it is observed that the self-modulation starts at the time of the ionizing laser pulse and thus of the ionization front. At low plasma densities, fast timescale images show the formation of micro-bunches. They also show that protons in between

the micro-bunches are de-focussed, which is consistent with the action of the transverse wakefields creating the micro-bunches. As mentioned in the beginning the results of this chapter have been published as "Experimental Observation of Proton Bunch Modulation in a Plasma at Varying Plasma Densities", PHYSICAL REVIEW LETTERS 122, 054802 (2019).

7 Thesis conclusion and outlook

In this thesis I have described the fundamental aspects, the formation of a train of micro-bunches on the bunch axis, of the self-modulation by using a qualitative model. I have designed and built an optical setup that is able to measure the defining features of the self-modulation instability in single events. With this setup I have shown that the self-modulation instability can be initialized with an RIF and I have shown that a train of micro-bunches is formed. I have further shown that the on-axis micro-bunch period is described by the inverse cold-electron plasma frequency.
In the first chapter introduces the need for diverse acceleration schemes, and the second chapter introduces the characteristic bunch train of the self-modulation instability. In the third chapter methods to measure the bunch train are discussed and OTR together with a streak camera is chosen. The fourth chapter shows that a streak-camera does have the time resolution to detect the frequency of a long pulse train up to $450GHz$ which makes it suitable for the AWAKE experiment. In the fifth chapter the implemented optical system is described and the setup is characterized. In the last chapter the self-modulation instability micro-bunch train is quantified. Time resolved images on a short timescale, or at a low Rubidium vapor density show that the train of micro-bunches is directly visible in a single event. I have shown that the self-modulation occurs only after the RIF and that it is a symmetric instability. The designed setup shows the defocused protons next to the micro-bunch train. A DFT based analysis shows that a large single peak at f_{pe} in the spectrum of single events can be associated with the modulation period of the micro-bunch train. At higher Rubidium densities the micro-bunches are no longer visible but the charge train does contain a peak that is 99% not from noise which is again at the cold electron plasma frequency. Overall it was shown that the measured micro-bunch train frequency f_m follows the linear theory prediction $f_m = f_{pe}$ and that 100% ionization should be assumed.
The setup in this thesis has been tremendously useful for the AWAKE experiment and lead to a lot of insights about the self-modulation process. Together with an extension of the system (a laser marker) by F. Batsch [83] that allows to stitch images together and circumvent the intrinsic jitter of the laser, streak camera and proton bunch. To highlight the usefulness of this setup I want to show that the setup was an important part in three (four including this thesis) PHD thesis.
In these works the self-modulation instability has been studied further and many important details that are needed for the self-modulation instability to be used in an accelerator were proven. It has been shown that:

- The self-modulation occurs behind the RIF and that there is a train of micro-bunches with modulation frequency f_{pe} (this work)

- The self-modulation can be seeded with the RIF or an electron bunch and it is phase stable which is extremely important for the use as an accelerator [83].
- Fundamental properties, as micro-bunch charge and radial distribution, of the self-modulation in the experiment are close to theoretical predictions [65].
- It has been shown that the self-modulation instability competes with the hosing instability and that the self-modulation is the dominant instability at high Rubidium densities [67] or when it is seeded.

While the importance of the first two works is easy to see, e.g. the importance in the third work is, that for any scientific or industrial accelerator a proven set of simulations is needed for the fast design of machines! The last work proves also that the self-modulation instability is, despite its name, a very robust and stable process. Further this setup has been used as an important complementary diagnostics with crucial information for the indirect self-modulation detection and the CTR detection of self-modulation.
In the long timeline for the AWAKE Run2a-d which goes from 2021/2022 to 2027 there is a lot of physics to be discovered and unknowns to be eradicated. In 2021/2022 it is planned to show that the self-modulation can also be seeded by using an electron bunch. This is needed because in Run2c and Run2d it is planned to use a staged plasma cell system with two consecutive plasma sources. In this case a RIF inside the bunch can not be used to seed the self-modulation. In the first plasma the RIF creates a bunch that is self-modulated behind the RIF and very phase stable but before the RIF the bunch is not modulated. The second plasma is pre-ionized and thus the front of the bunch can go through the self-modulation instability independently and interfere with the seeded self-modulation in the later parts. When placing the laser in front of the proton bunch the self-modulation becomes unseeded and is no longer phase-stable. This problem is circumvented by using an electron bunch for seeding of the self-modulation instability and the laser pulse to create a plasma in front of the bunch. This setup can also provide the measurements to show that the seeding is possible and that the self-modulation becomes phase stable. This goal of Run2a has been demonstrated (also using this setup) in 2022 [84].
The large works that are needed to upgrade the AWAKE area gives the possibility to rework the complete streak camera setup. With the additional experience and knowledge from Run1 there are optimizations possible. The two most important optimizations are discussed in the following.

- The current setup has two CCD cameras that can monitor the transverse distribution of the bunch, yet both can only be used instead of the streak camera by inserting a mirror on a flipper into the optical beam line. The experiments have shown that it is possible to use only the $\sim 450nm$ light for the streak camera and the amount of signal is large. Thus using dichroic mirrors or using a beamsplitter would allow the setup to make transverse measurements at the same time as time resolved measurements. This additional information is very useful to discriminate between the hosing instability and the self-modulation instability and gives infor-

mation about the bunch charge distribution transverse to the slit of the streak camera.

- The current setup can only image in the direction of the slit. The position of the slit within the bunch can be changed by motorized mirrors which allows the setup to scan the complete beam over many events. Together with the laser marker installed by F. Batsch (whose importance can not be understated) this setup is already very useful. A non-dispersive image rotation stage and a second streak camera would allow to image a second axis at the same time, or even the same axis at a later time. This lowers the number of events that are needed to do a full characterization of the self-modulated bunch and would allow for a more detailed characterization of the self-modulation. There exists currently a second streak camera operated by the CERN-BI group for electron bunch measurements. I have installed an optical transport line from the setup discussed in this work to the BI streak camera. This line works and can be used but the setup has not enough time resolution and too large light losses to be useful for frequencies $f_{smi} > 170GHz$. Further the options to place the slit on the streak camera are limited, due to the main use of the second streak camera to characterize electron beams. Yet it shows that a setup with a second streak camera is possible.

When implementing these optimizations I am confident that this setup will stay a vital part in the AWAKE diagnostics zoo.

8 Acknowledgments

I want to thank all people, institutions and groups that helped me to finish this work.

- Dr. Patric Muggli, for his daily supervision, the useful discussions, his patience and help and much more
- Prof. Dr. Allen Caldwell,for his patience as PhD supervisor and his introduction to Bayesian frameworks.
- Dr. Mikhail Martyanov and Dr. Joshua Moody and Dr. Erdem Öz for their support knowledge and their help when I didn't know any further.
- my colleagues Anna-Maria Bachmann, Fabian Batsch and Mathias Hüther for their good teamwork
- Ans pardons, Edda Gschwendtner, Marlene Turner Stefano Mazzoni and all others at CERN for their help in dealing with CERN
- Thomas Haubold and Markus Lippert for their workshop experience and expertise
- Ina Wacker, for her caring support
- All teams at CERN who made this thesis possible!

Thanks goes to the Werner-Heisenberg Institute for accepting me for a stipendium! Lastly I want to thank my wife Valerie for her support and patience and my son Valentin for being here!

List of Figures

Bibliography

[1] "The nobel prize in physics 1906, accessed 27/03/2022." [Online]. Available: https://www.nobelprize.org/prizes/physics/1906/thomson/biographical/

[2] P. J. Bryant, "A brief history and review of accelerators," 1994. [Online]. Available: https://cds.cern.ch/record/261062

[3] G. Dollinger and T. Faestermann, "Physics at the munich tandem accelerator laboratory," *Nuclear Physics News*, vol. 28, no. 1, pp. 5–12, 2018. [Online]. Available: https://doi.org/10.1080/10619127.2018.1427405

[4] W.Kleeven and S.Zaremba, "Cyclotrons: Magnetic design and beam dynamics," *Vol. 1 (2017): Proceedings of the CAS-CERN Accelerator School on Accelerators for Medical Applications*, 2017.

[5] F. Gerigk, "Cavity types," *CAS - CERN Accelerator School: RF for Accelerators, pp.277-298*, 2010.

[6] S. Braccini, "Particle accelerators and detectors for medical diagnostics and therapy," 2016.

[7] U. Amaldi, "The importance of particle accelerators," *Proceedings of EPAC 2000, Vienna*, 2000.

[8] Y. Suetsugu, "High-intensity synchrotron radiation effects," *CERN Yellow Reports*, p. Vol 2 (2016): Proceedings of the 2014 Joint International Accelerator School: Beam Loss and Accelerator Protection, 2016. [Online]. Available: https://e-publishing.cern.ch/index.php/CYR/article/view/230

[9] Xfel-how it works, accessed 01/04/2022. Available at: https://www.xfel.eu/facility/overview/how_it_works/index_eng.html.

[10] V. Dolgashev, "High gradient, x-band and above, metallic rf structures - 2nd european advanced accelerator concepts workshop - eaac 2015," *Nuclear Instruments and Methods in Physics Research Section A: Accelerators, Spectrometers, Detectors and Associated Equipment*, 2016.

[11] E. Halkiadakis, G. Redlinger, and D. Shih, "Status and implications of bsm searches at the lhc," 2014, arxiv:1411.1427. [Online]. Available: https://arxiv.org/abs/1411.1427

[12] C. Englert, A. Freitas, M. M. Mühlleitner, T. Plehn, M. Rauch, M. Spira, and K. Walz, "Precision measurements of higgs couplings: implications for new physics scales," *Journal of Physics G: Nuclear and Particle Physics*, vol. 41, no. 11, p. 113001, sep 2014. [Online]. Available: https://doi.org/10.1088%2F0954-3899%2F41%2F11%2F113001

[13] CERN Yellow Reports: Monographs, "Cern yellow reports: Monographs, vol. 1 (2022): European strategy for particle physics - accelerator rnd roadmap," 2022. [Online]. Available: https://e-publishing.cern.ch/index.php/CYRM/issue/view/146

[14] V. Shiltsev, "Considerations on energy frontier colliders after lhc," 11 2016. [Online]. Available: https://www.osti.gov/biblio/1341812

[15] A. Caldwell and M. Wing, "VHEeP: a very high energy electron–proton collider," *The European Physical Journal C*, vol. 76, no. 8, aug 2016. [Online]. Available: https://doi.org/10.1140%2Fepjc%2Fs10052-016-4316-1

[16] T. Tajima and J. M. Dawson, "Laser electron accelerator," *Phys. Rev. Lett.*, vol. 43, pp. 267–270, Jul 1979. [Online]. Available: https://link.aps.org/doi/10.1103/PhysRevLett.43.267

[17] T. Tajima, "Laser beat-wave accelerator for ultra-high energies," *IEEE Transactions on Nuclear Science*, vol. 30, no. 4, pp. 3209–3211, 1983.

[18] C. W. Siders, S. P. Le Blanc, D. Fisher, T. Tajima, M. C. Downer, A. Babine, A. Stepanov, and A. Sergeev, "Laser wakefield excitation and measurement by femtosecond longitudinal interferometry," *Phys. Rev. Lett.*, vol. 76, pp. 3570–3573, May 1996. [Online]. Available: https://link.aps.org/doi/10.1103/PhysRevLett.76.3570

[19] P. A. Walker, N. Bourgeois, W. Rittershofer, J. Cowley, N. Kajumba, A. R. Maier, J. Wenz, C. M. Werle, S. Karsch, F. Grüner, D. R. Symes, P. P. Rajeev, S. J. Hawkes, O. Chekhlov, C. J. Hooker, B. Parry, Y. Tang, and S. M. Hooker, "Investigation of GeV-scale electron acceleration in a gas-filled capillary discharge waveguide," *New Journal of Physics*, vol. 15, no. 4, p. 045024, apr 2013. [Online]. Available: https://doi.org/10.1088/1367-2630/15/4/045024

[20] A. J. Gonsalves, K. Nakamura, J. Daniels, C. Benedetti, C. Pieronek, T. C. H. de Raadt, S. Steinke, J. H. Bin, S. S. Bulanov, J. van Tilborg, C. G. R. Geddes, C. B. Schroeder, C. Tóth, E. Esarey, K. Swanson, L. Fan-Chiang, G. Bagdasarov, N. Bobrova, V. Gasilov, G. Korn, P. Sasorov, and W. P. Leemans, "Petawatt laser guiding and electron beam acceleration to 8 gev in a laser-heated capillary discharge waveguide," *Phys. Rev. Lett.*, vol. 122, p. 084801, Feb 2019. [Online]. Available: https://link.aps.org/doi/10.1103/PhysRevLett.122.084801

[21] A. Aimidula and P. Zhang, "A review of beam-driven plasma wakefield experiments," 2018. [Online]. Available: https://arxiv.org/abs/1807.02777

[22] J. Rosenzweig, P. Schoessow, B. Cole, W. Gai, R. Konecny, J. Norem, and J. Simpson, "Experimental measurement of nonlinear plasma wake-fields," in *Proceedings of the 1989 IEEE Particle Accelerator Conference, . 'Accelerator Science and Technology*, 1989, pp. 731–733 vol.2.

[23] J. D. Jackson, *Classical Electrodynamics2nd Edition.* John Wiley and Sons, New York, 1975.

[24] J. D. Hunter, "Matplotlib: A 2d graphics environment," *Computing in Science & Engineering*, vol. 9, no. 3, pp. 90–95, 2007.

[25] J. W. Eaton, D. Bateman, S. Hauberg, and R. Wehbring, "Gnu octave version 6.3.0 manual: a high-level interactive language for numerical computations," 2021. [Online]. Available: https://www.gnu.org/software/octave/doc/v6.3.0/

[26] C. R. Harris, K. J. Millman, S. J. van der Walt, R. Gommers, P. Virtanen, D. Cournapeau, E. Wieser, J. Taylor, S. Berg, N. J. Smith, R. Kern, M. Picus, S. Hoyer, M. H. van Kerkwijk, M. Brett, A. Haldane, J. F. del Río, M. Wiebe, P. Peterson, P. Gérard-Marchant, K. Sheppard, T. Reddy, W. Weckesser, H. Abbasi, C. Gohlke, and T. E. Oliphant, "Array programming with NumPy," *Nature*, vol. 585, no. 7825, pp. 357–362, Sep. 2020. [Online]. Available: https://doi.org/10.1038/s41586-020-2649-2

[27] P. Virtanen, R. Gommers, T. E. Oliphant, M. Haberland, T. Reddy, D. Cournapeau, E. Burovski, P. Peterson, W. Weckesser, J. Bright, S. J. van der Walt, M. Brett, J. Wilson, K. J. Millman, N. Mayorov, A. R. J. Nelson, E. Jones, R. Kern, E. Larson, C. J. Carey, İ. Polat, Y. Feng, E. W. Moore, J. VanderPlas, D. Laxalde, J. Perktold, R. Cimrman, I. Henriksen, E. A. Quintero, C. R. Harris, A. M. Archibald, A. H. Ribeiro, F. Pedregosa, P. van Mulbregt, and SciPy 1.0 Contributors, "SciPy 1.0: Fundamental Algorithms for Scientific Computing in Python," *Nature Methods*, vol. 17, pp. 261–272, 2020.

[28] A. C. Caldwell and M. Wing, "Vheep: a very high energy electron–proton collider," *The European Physical Journal C*, vol. 76, pp. 1–10, 2016.

[29] E. Gschwendtner, "The awake experiment at cern," *arXiv:1512.05498v1 [physics.acc-ph]*, 2015.

[30] K. Pepitone, S. Doebert, R. Apsimon, J. Bauche, M. Bernardini, C. Bracco, G. Burt, A. Chauchet, E. Chevallay, N. Chritin, S. Curt, H. Damerau, M. D. Kelisani, C. Delory, V. Fedosseev, F. Friebel, F. Galleazzi, I. Gorgisyan, E. Gschwendtner, J. Hansen, L. Jensen, F. Keeble, L. Maricalva, S. Mazzoni, G. McMonagle, O. Mete, A. Pardons, C. Pasquino, V. Verzilov, J. Schmidt, L. Soby, B. Williamson, E. Yamakawa, S. Pitman, and J. Mitchell, "The electron accelerators for the awake experiment at cern—baseline and future developments," *Nuclear Instruments and Methods in Physics Research Section A: Accelerators, Spectrometers, Detectors and Associated Equipment*, vol. 909, pp. 102–106, 2018,

3rd European Advanced Accelerator Concepts workshop (EAAC2017). [Online]. Available: https://www.sciencedirect.com/science/article/pii/S0168900218301980

[31] E. Oz, J. Moody, F. Batsch, and P. Muggli, "A novel plasma source for plasma wakefield accelerators," 05 2015, pp. 1–1.

[32] F. Batsch, M. Martyanov, E. Oez, J. Moody, E. Gschwendtner, A. Caldwell, and P. Muggli, "Interferometer-based high-accuracy white light measurement of neutral rubidium density and gradient at AWAKE," *Nuclear Instruments and Methods in Physics Research Section A: Accelerators, Spectrometers, Detectors and Associated Equipment*, vol. 909, pp. 359–363, nov 2018. [Online]. Available: https://doi.org/10.1016%2Fj.nima.2018.02.067

[33] M. Turner, A. Petrenko, B. Biskup, S. Burger, E. Gschwendtner, K. Lotov, S. Mazzoni, and H. Vincke, "Indirect self-modulation instability measurement concept for the awake proton beam," *Nuclear Instruments and Methods in Physics Research Section A: Accelerators, Spectrometers, Detectors and Associated Equipment*, vol. 829, pp. 314–317, 2016, 2nd European Advanced Accelerator Concepts Workshop - EAAC 2015. [Online]. Available: https://www.sciencedirect.com/science/article/pii/S0168900216000887

[34] A. Petrenko, G. Plyushchev, M. Turner, E. Gschwendtner, K. Lotov, and A. Sosedkin, "Beam-plasma interaction simulations for the awake experiment at cern," *Proceedings of IPAC2016, Busan, Korea*, 2016.

[35] F. F. Chen, *Plasma Physics and controlled Gusion Vol 1: Plasma Physics.* Plenum Press, 1984.

[36] J. M. Dawson, "Nonlinear electron oscillations in a cold plasma," *Phys. Rev.*, vol. 113, pp. 383–387, Jan 1959. [Online]. Available: https://link.aps.org/doi/10.1103/PhysRev.113.383

[37] R. D. Ruth, A. W. Chao, P. L. Morton, and P. B. Wilson, "A plasma wakefield accelerator," *SLAC-PUB-3374*, 1984.

[38] R. Keinigs and M. E. Jones, "Two-dimensional dynamics of the plasma wakefield accelerator," *The Physics of Fluids*, vol. 30, no. 1, pp. 252–263, 1987.

[39] E. Gschwendtner, "Awake, a particle-driven plasma wakefield acceleration experiment," *CERN Yellow Reports*, pp. Vol 1 (2016): Proceedings of the 2014 CAS–CERN Accelerator School: Plasma Wake Acceleration, 2016. [Online]. Available: https://e-publishing.cern.ch/index.php/CYR/article/view/223

[40] W. Lu, C. Huang, M. M. Zhou, W. B. Mori, and T. Katsouleas, "Limits of linear plasma wakefield theory for electron or positron beams," *Physics of Plasmas*, vol. 12, no. 6, p. 063101, 2005. [Online]. Available: https://doi.org/10.1063/1.1905587

[41] E. P. Lee and R. K. Cooper, "General envelope equation for cylindrically symmetric charged-particle beams," *Part. Accel.; (United States)*, 7 1976, available at:http://cds.cern.ch/record/1107845/files/p83.pdf. [Online]. Available: https://www.osti.gov/biblio/7142237

[42] N. Kumar, A. Pukhov, and K. Lotov, "Self-modulation instability of a long proton bunch in plasmas," *PRL 104, 255003*, 2010.

[43] M. Moreira, J. Vieira, and P. Muggli, "Influence of proton bunch parameters on a proton-driven plasma wakefield acceleration experiment," *Physical Review Accelerators and Beams*, vol. 22, no. 3, mar 2019. [Online]. Available: https://doi.org/10.1103%2Fphysrevaccelbeams.22.031301

[44] K. V. Lotov, "Fine wakefield structure in the blowout regime of plasma wakefield accelerators," *Phys. Rev. ST Accel. Beams*, vol. 6, p. 061301, Jun 2003. [Online]. Available: https://link.aps.org/doi/10.1103/PhysRevSTAB.6.061301

[45] A. P. Sosedkin and K. V. Lotov, "Lcode: A parallel quasistatic code for computationally heavy problems of plasma wakefield acceleration," *Nuclear Instruments & Methods in Physics Research Section A-accelerators Spectrometers Detectors and Associated Equipment*, vol. 829, pp. 350–352, 2016.

[46] H. Koziol, "Beam Diagnostics for Accelerators; 2005 ed." p. 44 p, May 2001. [Online]. Available: https://cds.cern.ch/record/499098

[47] S. Takano, "Beam diagnostics with synchrotron radiation in light sources," *IPAC 2010 - 1st International Particle Accelerator Conference*, 01 2010.

[48] J. Camas, G. Ferioli, J. J. Gras, and R. Jung, "Screens versus SEM grids for single pass measurements in SPS, LEP and LHC," in *2nd European Workshop on Beam Diagnostics and Instrumentation for Particle Accelerators*, 6 1995.

[49] H. H. B. C. Martinez, "Non-intercepting bunch length monitor for picosecond electron bunches," in *Proc. of the 6th Europ. Part. Accel. Conf*, 1998.

[50] P. Forck, "Beam instrumentation and diagnostics," 2020.

[51] M. L. Ter-Mikaelian, *High nergy Electromagnetic Processes in Condensed Media.* Wiley-Interscience, 1972.

[52] V. L. Ginzburg and V. N. Tsytovich, *Transition Radiation and Transition Scattering.* Adam Hilger, 1990.

[53] V. Ginzburg, "Transition radiation and transition scattering," *1982 Phys. Scr. 1982 182*, 1982.

[54] B. Bolotovskii, V. Davydov, and V. Rok, "The emission of electromagnetic waves in the case of a smooth variation of parameters," *Sov. Phys. Usp. 25(3), March*, 1982.

[55] K. Honkavaara, "Optical transition radiation in high energy electro beam diagnostics," Ph.D. dissertation, Helsinki Institue of Physics and Laboratoire de l'Accelerateur Lineaire, 1999.

[56] M. Castellano, A. Cianchi, G. Orlandi, and V. Verzilov, "Effects of diffraction and target finite size on coherent transition radiation spectra in bunch length measurements," *Nuclear Instruments and Methods in Physics Research Section A: Accelerators, Spectrometers, Detectors and Associated Equipment*, vol. 435, no. 3, pp. 297–307, 1999. [Online]. Available: https://www.sciencedirect.com/science/article/pii/S0168900299005665

[57] J. van Tilborg, "Coherent terahertz radiation from laser-wakefield-accelerated electron beams," Ph.D. dissertation, Applied Physics, 2006.

[58] P. Bell, R. Griffith, K. Hagans, R. Lerche, C. Allen, T. Davies, F. Janson, R. Justin, B. Marshall, and O. Sweningsen, "Compact optical technique for streak camera calibration," *Review of Scientific Instruments 75, 3930 (2004)*, 2004.

[59] C. C. Davis, *Lasers and Electro-optics: Fundamentals and engineering.* Cambridge University Press, 2014.

[60] D. Walls and G. Milburn, *Quantum Optics.* Springer, 2008.

[61] A. Girgis and F. Ham, "A quantitave study of the pitfalls in the fft," *IEEE AES-16,No 4*, 1980.

[62] A. Papoulis, *Probability, random variables, stocahstic processes.* McGraw-Hill, 1991, p. 140.

[63] F. Braunmüller, T. Nechaeva, E. Adli, R. Agnello, M. Aladi, Y. Andrebe, O. Apsimon, R. Apsimon, A.-M. Bachmann, M. A. Baistrukov, F. Batsch, M. Bergamaschi, P. Blanchard, P. N. Burrows, B. Buttenschön, A. Caldwell, J. Chappell, E. Chevallay, M. Chung, D. A. Cooke, H. Damerau, C. Davut, G. Demeter, L. H. Deubner, A. Dexter, G. P. Djotyan, S. Doebert, J. Farmer, A. Fasoli, V. N. Fedosseev, R. Fiorito, R. A. Fonseca, F. Friebel, I. Furno, L. Garolfi, S. Gessner, B. Goddard, I. Gorgisyan, A. A. Gorn, E. Granados, M. Granetzny, O. Grulke, E. Gschwendtner, V. Hafych, A. Hartin, A. Helm, J. R. Henderson, A. Howling, M. Hüther, R. Jacquier, S. Jolly, I. Y. Kargapolov, M. A. Kedves, F. Keeble, M. D. Kelisani, S.-Y. Kim, F. Kraus, M. Krupa, T. Lefevre, Y. Li, L. Liang, S. Liu, N. Lopes, K. V. Lotov, M. Martyanov, S. Mazzoni, D. Medina Godoy, V. A. Minakov, J. T. Moody, P. I. Morales Guzmán, M. Moreira, P. Muggli, H. Panuganti, A. Pardons, F. Peña Asmus, A. Perera, A. Petrenko, J. Pucek, A. Pukhov, B. Ráczkevi, R. L. Ramjiawan, S. Rey, H. Ruhl, H. Saberi, O. Schmitz, E. Senes, P. Sherwood, L. O. Silva, R. I. Spitsyn, P. V. Tuev, M. Turner, F. Velotti, L. Verra, V. A. Verzilov, J. Vieira, C. P. Welsch, B. Williamson, M. Wing, J. Wolfenden, B. Woolley, G. Xia, M. Zepp, and G. Zevi Della Porta, "Proton bunch self-modulation in plasma with density

gradient," *Phys. Rev. Lett.*, vol. 125, p. 264801, Dec 2020. [Online]. Available: https://link.aps.org/doi/10.1103/PhysRevLett.125.264801

[64] M. Born and E. Wolf, *Principles of Optics: 60th Anniversary Edition*, 7th ed. Cambridge University Press, 2019.

[65] A.-M. Bachmann, "Self-modulation development of a proton bunch in plasma," 2021. [Online]. Available: https://mediatum.ub.tum.de/?id=1595621

[66] M. Castellano and V. A. Verzilov, "Spatial resolution in optical transition radiation beam diagnostics," *Phys. Rev. ST Accel. Beams*, vol. 1, p. 062801, Oct 1998. [Online]. Available: https://link.aps.org/doi/10.1103/PhysRevSTAB.1.062801

[67] M. J. Hüther, "Direct observation of the hosing instability of a long relativistic proton bunch in the awake experiment," 2020. [Online]. Available: https://mediatum.ub.tum.de/?id=1554985

[68] S. Gessner and t. A. Collaboration, "Evolution of a plasma column measured through modulation of a high-energy proton beam," 2020. [Online]. Available: https://arxiv.org/abs/2006.09991

[69] C. Bracco, E. Gschwendtner, A. Petrenko, H. Timko, T. Argyropoulos, H. Bartosik, T. Bohl, J. Esteban Müller, B. Goddard, M. Meddahi, A. Pardons, E. Shaposhnikova, F. M. Velotti, and H. Vincke, "Beam studies and experimental facility for the awake experiment at cern," *Nuclear Instruments and Methods in Physics Research Section A: Accelerators, Spectrometers, Detectors and Associated Equipment*, vol. 740, pp. 48–53, 2014, proceedings of the first European Advanced Accelerator Concepts Workshop 2013. [Online]. Available: https://www.sciencedirect.com/science/article/pii/S0168900213014411

[70] A.-M. Bachmann and P. Muggli, "Determination of the charge per micro-bunch of a self-modulated proton bunch using a streak camera," *Journal of Physics: Conference Series*, vol. 1596, no. 1, p. 012005, jul 2020. [Online]. Available: https://doi.org/10.1088/1742-6596/1596/1/012005

[71] P. Guzman, P. Muggli, R. Agnello, C. Ahdida, M. Aladi, C. Amoedo, Y. Andrebe, O. Apsimon, R. Apsimon, A.-M. Bachmann, M. Baistrukov, F. Batsch, M. Bergamaschi, P. Blanchard, F. Braunmueller, P. Burrows, B. Buttenschoenn, A. Caldwell, J. Chappell, and G. Porta, "Simulation and experimental study of proton bunch self-modulation in plasma with linear density gradients," *Physical Review Accelerators and Beams*, vol. 24, 10 2021.

[72] P. Guzman, P. Muggli, R. Agnello, C. Ahdida, M. Aladi, C. Amoedo, Y. Andrebe, O. Apsimon, R. Apsimon, A.-M. Bachmann, M. Baistrukov, F. Batsch, M. Bergamaschi, P. Blanchard, F. Braunmueller, P. Burrows, B. Buttenschön, A. Caldwell, J. Chappell, and G. Porta, "Simulation and experimental study of proton bunch self-modulation in plasma with linear density gradients," *Physical Review Accelerators and Beams*, vol. 24, 10 2021.

[73] F. Batsch, M. Martyanov, E. Oez, J. Moody, E. Gschwendtner, A. Caldwell, and P. Muggli, "Interferometer-based high-accuracy white light measurement of neutral rubidium density and gradient at awake," *Nuclear Instruments and Methods in Physics Research Section A: Accelerators, Spectrometers, Detectors and Associated Equipment*, vol. 909, pp. 359–363, 2018, 3rd European Advanced Accelerator Concepts workshop (EAAC2017). [Online]. Available: https://www.sciencedirect.com/science/article/pii/S0168900218302213

[74] E. Öz, F. Batsch, and P. Muggli, "An accurate rb density measurement method for a plasma wakefield accelerator experiment using a novel rb reservoir," *Nuclear Instruments and Methods in Physics Research Section A: Accelerators, Spectrometers, Detectors and Associated Equipment*, vol. 829, pp. 321–325, 2016, 2nd European Advanced Accelerator Concepts Workshop - EAAC 2015. [Online]. Available: https://www.sciencedirect.com/science/article/pii/S0168900216001558

[75] L. Verra, E. Gschwendtner, and P. Muggli, "Focusing of a long relativistic proton bunch in underdense plasma," 2023. [Online]. Available: https://arxiv.org/abs/2302.04051

[76] A.-M. Bachmann and P. Muggli, "Determination of the charge per micro-bunch of a self-modulated proton bunch using a streak camera," *Journal of Physics: Conference Series*, vol. 1596, p. 012005, 07 2020.

[77] G. Demeter, J. Moody, M. Kedves, B. Ráczkevi, M. Aladi, A.-M. Bachmann, F. Batsch, F. Braunmueller, G. Djotyan, V. Fedosseev, F. Friebel, S. Gessner, E. Granados, E. Guran, M. Hüther, V. Lee, M. Martyanov, P. Muggli, E. Öz, and G. Porta, "Long-range propagation of ultrafast ionizing laser pulses in a resonant nonlinear medium," *Physical Review A*, vol. 104, 09 2021.

[78] K. Pearson and F. Galton, "Vii. note on regression and inheritance in the case of two parents," *Proceedings of the Royal Society of London*, vol. 58, no. 347-352, pp. 240–242, 1895. [Online]. Available: https://royalsocietypublishing.org/doi/abs/10.1098/rspl.1895.0041

[79] F. Batsch, P. Muggli, R. Agnello, C. C. Ahdida, M. C. Amoedo Goncalves, Y. Andrebe, O. Apsimon, R. Apsimon, A.-M. Bachmann, M. A. Baistrukov, P. Blanchard, F. Braunmüller, P. N. Burrows, B. Buttenschön, A. Caldwell, J. Chappell, E. Chevallay, M. Chung, D. A. Cooke, H. Damerau, C. Davut, G. Demeter, H. L. Deubner, S. Doebert, J. Farmer, A. Fasoli, V. N. Fedosseev, R. Fiorito, R. A. Fonseca, F. Friebel, I. Furno, L. Garolfi, S. Gessner, I. Gorgisyan, A. A. Gorn, E. Granados, M. Granetzny, T. Graubner, O. Grulke, E. Gschwendtner, V. Hafych, A. Helm, J. R. Henderson, M. Hüther, I. Y. Kargapolov, S.-Y. Kim, F. Kraus, M. Krupa, T. Lefevre, L. Liang, S. Liu, N. Lopes, K. V. Lotov, M. Martyanov, S. Mazzoni, D. Medina Godoy, V. A. Minakov, J. T. Moody, K. Moon, P. I. Morales Guzmán, M. Moreira, T. Nechaeva, E. Nowak, C. Pakuza, H. Panuganti, A. Pardons, A. Perera,

J. Pucek, A. Pukhov, R. L. Ramjiawan, S. Rey, K. Rieger, O. Schmitz, E. Senes, L. O. Silva, R. Speroni, R. I. Spitsyn, C. Stollberg, A. Sublet, A. Topaloudis, N. Torrado, P. V. Tuev, M. Turner, F. Velotti, L. Verra, V. A. Verzilov, J. Vieira, H. Vincke, C. P. Welsch, M. Wendt, M. Wing, P. Wiwattananon, J. Wolfenden, B. Woolley, G. Xia, M. Zepp, and G. Zevi Della Porta, "Transition between instability and seeded self-modulation of a relativistic particle bunch in plasma," *Phys. Rev. Lett.*, vol. 126, p. 164802, Apr 2021. [Online]. Available: https://link.aps.org/doi/10.1103/PhysRevLett.126.164802

[80] E. Adli, A. Ahuja, O. Apsimon, R. Apsimon, A.-M. Bachmann, D. Barrientos, F. Batsch, J. Bauche, V. K. Berglyd Olsen, M. Bernardini, T. Bohl, C. Bracco, F. Braunmüller, G. Burt, B. Buttenschön, A. Caldwell, M. Cascella, J. Chappell, E. Chevallay, M. Chung, D. Cooke, H. Damerau, L. Deacon, L. H. Deubner, A. Dexter, S. Doebert, J. Farmer, V. N. Fedosseev, R. Fiorito, R. A. Fonseca, F. Friebel, L. Garolfi, S. Gessner, I. Gorgisyan, A. A. Gorn, E. Granados, O. Grulke, E. Gschwendtner, J. Hansen, A. Helm, J. R. Henderson, M. Hüther, M. Ibison, L. Jensen, S. Jolly, F. Keeble, S.-Y. Kim, F. Kraus, Y. Li, S. Liu, N. Lopes, K. V. Lotov, L. Maricalva Brun, M. Martyanov, S. Mazzoni, D. Medina Godoy, V. A. Minakov, J. Mitchell, J. C. Molendijk, J. T. Moody, M. Moreira, P. Muggli, E. Öz, C. Pasquino, A. Pardons, F. Peña Asmus, K. Pepitone, A. Perera, A. Petrenko, S. Pitman, A. Pukhov, S. Rey, K. Rieger, H. Ruhl, J. S. Schmidt, I. A. Shalimova, P. Sherwood, L. O. Silva, L. Soby, A. P. Sosedkin, R. Speroni, R. I. Spitsyn, P. V. Tuev, M. Turner, F. Velotti, L. Verra, V. A. Verzilov, J. Vieira, C. P. Welsch, B. Williamson, M. Wing, B. Woolley, and G. Xia, "Acceleration of electrons in the plasma wakefield of a proton bunch," *Nature*, vol. 561, no. 7723, pp. 363–367, Sep. 2018.

[81] Y. Fang, V. E. Yakimenko, M. Babzien, M. Fedurin, K. P. Kusche, R. Malone, J. Vieira, W. B. Mori, and P. Muggli, "Seeding of self-modulation instability of a long electron bunch in a plasma," *Phys. Rev. Lett.*, vol. 112, p. 045001, Jan 2014. [Online]. Available: https://link.aps.org/doi/10.1103/PhysRevLett.112.045001

[82] M. Gross, J. Engel, J. Good, H. Huck, I. Isaev, G. Koss, M. Krasilnikov, O. Lishilin, G. Loisch, Y. Renier, T. Rublack, F. Stephan, R. Brinkmann, A. Martinez de la Ossa, J. Osterhoff, D. Malyutin, D. Richter, T. Mehrling, M. Khojoyan, C. B. Schroeder, and F. Grüner, "Observation of the self-modulation instability via time-resolved measurements," *Phys. Rev. Lett.*, vol. 120, p. 144802, Apr 2018. [Online]. Available: https://link.aps.org/doi/10.1103/PhysRevLett.120.144802

[83] F. G. Batsch, "Instability and seeded self-modulation of a relativistic proton bunch in plasma," 2021.

[84] L. Verra, G. Porta, J. Pucek, T. Nechaeva, S. Wyler, M. Bergamaschi, E. Senes, E. Guran, J. Moody, M. Kedves, E. Gschwendtner, P. Muggli, R. Agnello, C. Ahdida, M. Goncalves, Y. Andrebe, O. Apsimon, R. Apsimon, J. Arnesano, and

M. Zepp, "Controlled growth of the self-modulation of a relativistic proton bunch in plasma," *Physical Review Letters*, vol. 129, 07 2022.